POLITECNICO DI MILANO

Scuola di Ingegneria Industriale e dell'Informazione
Corso di Laurea Magistrale in Ingegneria Fisica
Dipartimento di Fisica

Crystallographic investigation of gold nanoparticles embedded in a $SrTiO_3$ thin film for plasmonics applications

Relatore: Prof. Giacomo Claudio Ghiringhelli
Correlatori: Dott. Carsten Detlefs & Dott. Claudio Mazzoli

Tesi di Laurea di:
Davide Pincini
Matr. Nr. 784259

Anno Accademico 2012/2013

"It's not who you are underneath,
it's what you do that defines you."

Rachel Dawes

The Dark Knight Trilogy, C. Nolan

Sommario

Sistemi costituiti da nanoparticelle metalliche costituiscono l'oggetto di studio di un ampio filone di ricerca che coinvolge discipline differenti, tra cui si annoverano la fisica applicata (in particolare le nanotecnologie), le scienze dei materiali, la chimica e non da ultima la biologia. Lo studio di nanoparticelle metalliche è stato recentemente rinominato *plasmonica*. Il nome deriva dal fatto che le proprietà ottiche di particelle metalliche di dimensioni nanometriche sono caratterizzate dalla presenza del cosiddetto *plasmone localizzato di superficie*. Questi altro non è che un'eccitazione collettiva del mare di elettroni liberi del metallo a seguito dell'interazione con un fascio luminoso: alla lunghezza d'onda della risonanza plasmonica, l'eccitazione produrrà un forte assorbimento della radiazione incidente, provocando una diminuzione del segnale trasmesso. I plasmoni localizzati costituiscono la specializzazione al caso di particelle metalliche dei plasmoni superficiali presenti in generale all'interfaccia tra un metallo e un dielettrico. La localizzazione offre la possibilità aggiuntiva di ingegnerizzare le proprietà della risonanza plasmonica regolando opportunamente le caratteristiche morfologiche e strutturali delle nanoparticelle. Sebbene una completa comprensione delle proprietà ottiche delle nanoparticelle metalliche sia stata raggiunta solamente nell'ultimo quarto del XX secolo, i loro effetti sono stati sfruttati fin dall'antichità e sono visibili nella vita di tutti i giorni. La risonanza plasmonica è infatti responsabile, per esempio, degli stupendi colori dei vetri utilizzati nei rosoni e nelle vetrate di molte cattedrali gotiche. Le proprietà ottiche di sistemi costituiti da nanoparticelle metalliche sono stato oggetto del recente interesse di molti autori (Kelly et al. [30], Link and El-Sayed [37], Jackson and Halas [27]) e sono all'origine del loro interesse applicativo. La sensibilità della risonanza plasmonica alle caratteristiche dell'ambiente in cui le nanoparticelle sono immerse e l'incremento locale del campo associato all'eccitazione rendono le nanoparticelle particolarmente indicate per la realizzazione di sensori, in particolare per la detezione di agenti biologici (Prasad [45]). L'incremento locale di campo può essere in particolare sfruttato per aumentare l'efficienza di processi ottici lineari e non lineari in una molecola posta a breve distanza dalla nanoparticella, come nel caso della Surface Enhanced Raman Spectroscopy (SERS). Altre possibili applicazioni si collocano nel campo dell'ottica guidata (realizzazione di guide d'onda plasmoniche), nelle tecniche di microscopia ottica in campo vicino senza aperture e nella catalisi di reazione chimiche (Bell [3]). In generale le proprietà, specialmente ottiche, delle nanoparticelle metalliche dipendono dalla loro morfologia e struttura. Queste, a loro volta sono determinate dai fenomeni su scala atomica coinvolti nel processo di formazione delle nanoparticelle, i quali sono quindi di grande interesse sia scientifico che tecnologico.

I campioni oggetto del presente lavoro sono costituiti da nanoparticelle di oro (Au) monocristalline incorporate all'interno di un film sottile di titanato di stronzio ($SrTiO_3$, abbreviato in STO), un ossido con reticolo cubico a temperatura ambiente. Campioni di questo genere sono stati recentemente realizzati (Christke et al. [13] e Katzer et al. [29]) mediante un processo di deposizione costituito da due passi successivi. Il primo prevede la deposizione, mediante Magnetron Sputtering, di un film sottile d'oro su un substrato di STO orientato secondo la direzione (001). Dopo un annealing a 1070 K, si realizza la deposizione di un film sottile di STO al di sopra del layer d'oro, mediante Pulsed Laser Deposition. L'aspetto interessante consiste nel fatto che, durante questo secondo passaggio, le isole del layer d'oro (soggette ad un processo di dewetting a seguito dell'annealing) sono interessate da un processo di ricostruzione che porta alla formazione di nanoparticelle metalliche all'interno del film sottile di STO. Questo sistema di fabbricazione costituisce una valida alternativa agli altri precedentemente utilizzati (Pelton et al. [44]) e presenta il vantaggio che la forma e le dimensioni delle nanoparticelle possono essere variate cambiando opportunamente i parametri di deposizione. Le nanoparticelle così ottenute presentano una forma ellittica, con l'asse maggiore diretto nella direzione ortogonale al substrato: tale anisotropia le rende particolarmente appetibili per applicazioni sensoristiche, in particolare per la rivelazione di agenti biologici. Nanoparticelle preparate con un metodo analogo sono state sfruttate anche per limitare i fenomeni dissipativi in superconduttori ad alta temperatura critica (Grosse et al. [23] e Katzer et al. [28]) e per l'ingegnerizzazione di giunzioni Josephson (Michalowski et al. [40]).

Lo studio oggetto della tesi costituisce la fase preliminare di un progetto di ricerca che si pone l'obiettivo di: *i*) investigare le principali caratteristiche (tra cui forma e dimensioni) che impattano le proprietà ottiche delle nanoparticelle così ottenute; *ii*) esplorare la natura delle modifiche indotte al film circostante dalla presenza delle nanoparticelle e il legame tra queste e le carattestiche strutturali delle nanoparticelle stesse. In particolare, le misure presentate in questo elaborato sono state mirate a realizzare una caratterizzazione cristallografica delle nanoparticelle di oro e, in misura minore, del titanato di stronzio circostante. Una caratterizzazione di questo tipo non è importante solamente alla luce delle possibili applicazioni pratiche dei campioni studiati. Essa infatti ha anche un valore intrinseco, in quanto consente di ottenere preziose informazioni cristallografiche su sistemi ottenuti crescendo metalli di transizione (in particolare cubici a facce centrate, come nel caso dell'oro) su substrati ceramici. Tali proprietà infatti, risultano ancora oggi molto poco documentate in letteratura, specialmente nel caso dell'oro. La tecnica a cui si è fatto ricorso è la ben consolidata diffrazione da raggi X, realizzata mediante radiazione di sincrotrone. Le misure hanno preso parte interamente sulla beamline ID06 del European Synchrotron Radiation Facility (ESRF) a Grenoble, Francia. I dati presi in considerazione sono stati raccolti nel corso di due esperimenti distinti, ciascuno con un differente setup sperimentale; in entrambi i casi si è fatto ricorso a raggi X duri (con energia compresa tra 7 e 15 keV). Il primo dei due esperimenti ha fatto uso di un detector CCD a superficie planare: tale detector è stato utilizzato per acquisire un gran numero di immagini, ciascuna per una differente orientazione del campione rispetto al fascio primario. Nel secondo invece è stato utilizzato un detector puntiforme

alloggiato su un tradizionale diffrattometro per esperimenti di diffrazione da cristalli singoli.

Le misure sono state realizzate su più campioni con un diverso spessore del layer d'oro (1, 1.5, 2, 3, 4, 5.3 e 8 nm) a parità di spessore del film sottile di STO (275 nm). È stato inoltre preso in considerazione anche un campione aggiuntivo cresciuto in maniera analoga agli altri (con 5 nm di spessore del film d'oro), ma senza il layer di STO sovrastante. Quest'ultimo ha consentito di sondare le isole del layer d'oro soggetto al fenomeno di dewetting, prima che queste diano origine alle nanoparticelle. Con i dati del primo esperimento si è cercato principalmente di sfruttare l'ampio campo visivo del CCD per avere una panoramica generale sulle orientazioni cristallografiche preferenziali delle nanoparticelle d'oro. Per fare ciò è stato necessario mettere in relazione ciascun pixel del detector con il corrispondente vettore del reticolo reciproco del campione. A questo scopo si è reso necessario adattare alla geometria sperimentale utilizzata l'apparato matematico descritto da He [25]. Dall'analisi è emersa la presenza di due orientazioni cristallografiche preferenziali per le nanoparticelle d'oro nella direzione ortogonale al substrato, nella fattispecie {111} e {200}: le medesime orientazioni sono state osservate anche nel campione senza layer di STO. Tali risultati sono consistenti con le proprietà documentate in letteratura per sistemi simili (Fu and Wagner [19] e Francis and Salvador [16]). Per spessori del layer d'oro al di sopra di 5 nm, si è inoltre visto che il film sottile di titanato di stronzio cessa di avere un preciso ordinamento cristallino (con epitassia (001)): al contrario è emersa la presenza di grani policristallini orientati preferenzialmente con le direzioni {111} o {110} ortogonali al substrato. Da sottolineare il fatto che per i campioni con 1 e 1.5 nm di oro l'orientazione {111} delle nanoparticelle d'oro sembra non essere esattamente rispettata: sono stati infatti misurati picchi di diffrazione {111} in direzioni leggermente inclinate rispetto alla verticale.

Per ciascuna delle due orientazioni verticali si è poi cercato di determinare quale fosse l'orientazione dei nanocristalli d'oro parallelamente alla superficie del substrato. Per farlo è stato misurato l'angolo tra la proiezione nel piano del vettore {220} del cristallo di oro e l'asse cubico (001) del substrato. Per quanto riguarda le nanoparticelle orientate secondo la {111}, per uno spessore del layer d'oro superiore a 2 nm si è messa in luce l'esistenza di due famiglie di nanoparticelle caratterizzate da un valore dell'angolo suddetto, che chiamiamo β_{111}, di 0° e 45°. Lo stesso tipo di ordinamento è stato evidenziato anche per il campione senza layer di STO. Per il campione con 1 nm di oro invece la famiglia caratterizzata da $\beta_{111} = 0°$ sembra essere assente, suggerendo l'idea che tra 1 e 2 nm di spessore si verifichi una transizione che porta una delle due famiglie ad essere energeticamente sfavorita. Con i dati raccolti non è purtroppo possibile affermare con certezza quale sia il ruolo del film di titanato di stronzio nel verificarsi di questa transizione. Per quanto riguarda le nanoparticelle orientate secondo la {200} sono stati osservati gli stessi valori dell'angolo che definisce l'orientazione nel piano, in questo caso chiamato β_{002}. Nel campione senza layer d'oro l'orientazione delle isole sembra essere in questo caso leggermente diversa, essendo praticamente assente il picco a 45° ed essendo invece presenti più valori di orientazione nel piano attorno a 0°. Per tutti gli spessori d'oro superiori agli 1.5 nm, l'abbondanza della famiglia con $\beta_{002} = 0°$ è superiore all'altra, rimanendo tuttavia comparabile. Per 1 nm di spessore d'oro il rapporto è totalmente invertito, con la famiglia con $\beta_{002} = 0°$ che risulta essere quasi assente. Anche in questo caso

quindi, le orientazioni cristallografiche di crescita sembrano dipendere dal quantitativo di oro depositato. Come prima, però, non è stato possibile determinare con esattezza quale sia il ruolo del film sottile di STO. Sia per le nanoparticelle orientate lungo la {111} che per quelle orientate lungo la {200} le orientazioni osservate al di sopra di 2 nm di oro sono consistenti con quanto riportato in letteratura (Fu and Wagner [19] e Silly and Castell [46]).

Per quanto riguarda eventuali sviluppi futuri, resta ancora da chiarire la natura della transizione osservata a cavallo tra 1 e 2 nm di spessore del layer d'oro e il ruolo ricoperto dal film sottile di titanato di stronzio. Per farlo sarebbe necessario avere a disposizione più campioni senza layer di STO per differenti spessori del film d'oro. Per definire in maniera più precisa le proprietà dell'interfaccia Au/STO potrebbe essere interessante un'indagine più approfondita della superficie del substrato utilizzato, con riguardo, per esempio, alle terminazioni presenti. Infine, i dati di diffrazione raccolti potranno essere utilizzati per investigare l'eventuale presenza di strain nelle nanoparticelle e/o nel titanato di stronzio e per ottenere ulteriori informazioni sulle dimensioni e sulla forma delle nanoparticelle (proprietà di grande rilievo per le applicazioni plasmoniche).

Il presente lavoro è organizzato come segue. Dopo una breve panoramica generale sulle nanoparticelle metalliche nella ricerca e nelle applicazioni tecnologiche (Sezione 1.1), il Capitolo 1 descriverà i campioni studiati, con particolare riferimento al metodo di preparazione e al loro potenziale interesse per applicazioni pratiche (Sezione 1.2). Il Capitolo 2 presentarà poi i principali concetti teorici coinvolti nelle misure sperimentali oggetto dei capitoli successivi: le Sezioni 2.1 e 2.2 forniranno rispettivamente i fondamenti della tecnica di diffrazione da raggi X e le principali properietà dei metalli di transizione (in particolare cubici a facce centrate) depositati su substrati ceramici; la Sezione 2.3 discuterà invece in dettaglio l'apparato matematico necessario per la descrizione di un esperimento di diffrazione con un detector CCD a superficie planare. A seguito della presentazione del setup sperimentale del Capitolo 3, verranno mostrati e discussi i principali risultati ottenuti. In particolare il Capitolo 4 presenterà l'analisi preliminare delle orientazioni cristallografiche preferenziali e discuterà le principali direzioni verticali di crescita delle nanoparticelle d'oro (assieme alle modifiche da queste indotte nel layer di STO). Il Capitolo 5 riguarderà invece l'investigazione dell'orientazione nel piano della superficie del substrato dei cristalli d'oro, cercando di metterne in luce il legame con la presenza del film sottile di STO e con il quantitativo di oro depositato. Infine, nelle appendici, il lettore potrà trovare una sintetica introduzione alle proprietà della radiazione di sincrotrone (Appendice A) e alcuni dettagli sul programma utilizzato per la riduzione dei dati di diffrazione acquisiti con il detector CCD (Appendice B). Nell'Appendice C è inoltre riportato il listato dei principali script Python realizzati dall'autore del presente lavoro per l'analisi dati.

Contents

Abstract

Metallic nanoparticles represent a widespread subject of study in several different fields of research, such as applied physics (nanotechnology), material science, chemistry and biology. In recent years they have been extensively studied by many authors (Kelly et al. [30], Link and El-Sayed [37], Jackson and Halas [27]) particularly with respect to their optical properties. These are characterized by the presence of the so called localized surface plasmon resonance, which earned the study of metallic nanoparticles the name of *plasmonics*. Their properties have been probed with a wide selection of experimental techniques, ranging from microscopy (TEM, AFM, STM ...) to optical spectroscopy and X-ray diffraction, and a large variety of fabrication methods (Pelton et al. [44]) have been explored to obtain systems made up of nanoparticles of various metals. Furthermore, they have been proved to be promising for many different scientific and practical applications (Prasad [45] and Bell [3]), for which both the surrounding medium sensitivity of the plasmonic resonance and the associated local field enhancement play a major role. The morphological and structural features of the metallic nanoparticles are strictly related to their properties in most of the applications mentioned above. These features mainly depend on the particular preparation method exploited for the nanoparticles production: a fundamental understanding of the atomic-scale processes involved in the nanoparticles formation is thus of great importance.

The samples object of the present work are composed by anisotropic monocrystalline gold (Au) nanoparticles embedded in a strontium titanate ($SrTiO_3$) thin film. They were prepared through a novel two-steps deposition process, whose main parameters can be varied in order to obtain nanoparticles of different size and shape (Christke et al. [13] and Katzer et al. [29]). This process therefore allows to tune the optical properties of the nanoparticles and it constitutes a valid alternative to other traditionally used fabrication processes, particularly for the production of plasmonic active sensors in life sciences. Nanoparticles prepared with an analogous deposition process have been also exploited as flux pinning centers in high temperature superconducting YBCO thin films (Grosse et al. [23] and Katzer et al. [28]) or for the engineering of YBCO grain boundaries in Josephson junctions (Michalowski et al. [40]).

The study here presented consists of a crystallographic characterization realized through synchrotron X-ray diffraction. The aim was to determine the preferred crystallographic orientations of the Au nanocrystals and their interaction with the surrounding $SrTiO_3$ matrix. It represents the first step of a research project addressing the nanoparticles features (such as the shape and the dimension) with an impact on their optical properties and the mod-

ifications induced in the surrounding matrix. Samples with different amounts of deposited Au were probed with a hard X-ray beam and two different diffraction setups were used, exploiting both a two-dimensional and a zero-dimensional detector. The main vertical (normal to the substrate) growth direction of the nanoparticles was determined for all the samples, along with the crystalline quality of the $SrTiO_3$ layer. For each vertical growth direction the in-plane orientation of the Au crystals was measured, in order to fully determine their crystallographic orientation with respect to the substrate. The correlation between the nanoparticles orientation and the amount of deposited Au was investigated, trying to understand the role of the $SrTiO_3$ thin film in the nanoparticles formation process. Such a characterization is not only important in the light of the potential practical applications of the samples, but it is also valuable in itself. It indeed offers the possibility of a deeper understanding of the fundamental properties regarding the growth of Au (and transition metals in general) on ceramic substrates, which are still not well explored.

The present work is organized as explained hereafter. After a general overview of metallic nanoparticles (Section 1.1), Chapter 1 describes the samples experimentally probed, with particular focus on the preparation methods used and their potential practical applications (Section 1.2). Chapter 2 provides the reader with the main theoretical concepts involved in the measurements presented in the following chapters: Sections 2.1 and 2.2 outline the basics of the X-ray diffraction technique and the properties of transition (face centered cubic) metals deposited on ceramic substrate respectively; then, Section 2.3 describes in detail all the mathematical framework necessary for the description of a diffraction experiment performed with a CCD area detector. Following the presentation of the experimental setup of Chapter 3, the main experimental results obtained are discussed. In particular Chapter 4 presents the preliminary textured analysis undertaken and the main vertical growth direction of the Au nanoparticles (along with the modification induced in the $SrTiO_3$ thin film). Chapter 5 deals with the in-plane investigation of the Au crystals, addressing its relation with the presence of the $SrTiO_3$ layer and the amount of Au deposited. Finally the appendices provide a brief overview of the properties of synchrotron radiation (Appendix A) and some details about the program used to performed the CCD diffraction data reduction (Appendix B). In Appendix C the most important Python scripts used for the data analysis are reported.

Chapter 1

Metal nanoparticles overview

This chapter aims to contextualize the present work and to provide the main motivations which its scientific interest is based on. In Section 1.1 a general overview of the recently developed research field concerning metallic nanoparticles, along with its possible practical applications, is presented. Section 1.2 describes the samples object of the experimental data discussed in Chapters 4 and 5: their preparation methods are outlined and their scientific relevance is highlighted.

1.1 Overview of the usage of metal nanoparticles as plasmonic active materials: preparation methods and possible applications

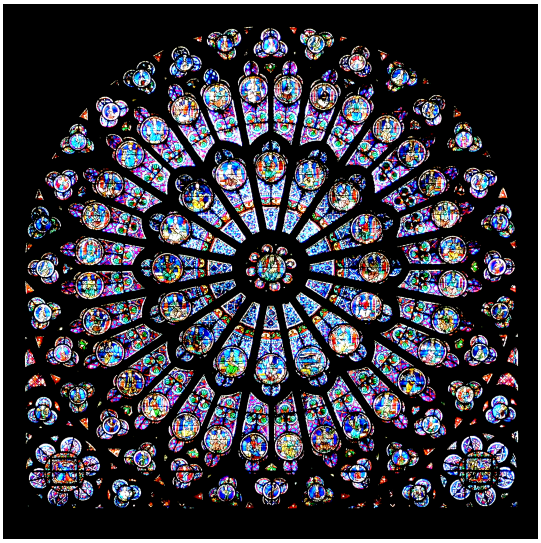

Figure 1.1: Gothic stained glass rose window of Notre-Dame de Paris. The colors are due to presence of colloids of gold nanoparticles [50].

Metallic nanostructures have been a subject of considerable interest in recent years. The

study of metallic nanostructure is generally referred to as *plasmonics*: this term derives from the fact that the behavior of metallic nanoparticles upon optical excitations is governed by the presence of the so called *localized surface plasmon resonance* (LSPR). Although a complete explanation of the optical properties of metallic nanoparticles was fully provided only during the last quarter of the 20th century [33], their effect have been clearly evident in everybody's everyday life for centuries (see Figure 1.1).

A localized surface plasmon is a collective excitation of the conduction electrons of the metal nanoparticle surface driven by the electromagnetic field of a light wave incident on it (see Figure 1.2). Although several theoretical models have been proposed (Kelly et al. [30]), the optical properties of metal nanoparticles can be described in terms of the classical model of Mie (Wolf [58]). For nanoparticles much smaller than the wavelength of the incident radiation (about 25 nm for Au particles [53]) a dipole approximation can be adopted, leading to the following expression for the extinction coefficient (Vollmer and Kreibig [53]):

$$k = \frac{18\pi N V \epsilon_d^{3/2}}{\lambda} \frac{\epsilon_2}{[\epsilon_1 + 2\epsilon_d]^2 + \epsilon_2^2} \tag{1.1}$$

being λ the wavelength of the incident radiation, N the total number of nanoparticles present, V the nanoparticle volume, ϵ_d the dielectric function of the surrounding medium (assumed to be a frequency independent real constant) and ϵ_1 and ϵ_2 the real and the imaginary part of the metal dielectric function ϵ_m respectively, such that $\epsilon_m = \epsilon_1(\omega) + i\epsilon_2(\omega)$ (ω being the frequency of the incident radiation). The previous expression exhibits a resonance (i.e. the LSPR) when the following condition holds

$$\epsilon_1 = -2\epsilon_d \tag{1.2}$$

This condition, known as *Fröhlich condition* (Fröhlich [18]), is valid in the assumption that $\epsilon_2 \ll 1$ or $\partial\epsilon_2(\omega)/\partial\omega \ll \partial\epsilon_1(\omega)/\partial\omega$. When the wavelength of the incident radiation is such that the previous condition is satisfied, the localized surface plasmon is excited and the extinction coefficient (1.1) exhibits a maximum. Using the Drude-Sommerfeld model to express the metal dielectric function, the corresponding resonance frequency ω_{SP} (derived from equation (1.1)) is given by (Gaponenko [20])

$$\omega_{SP} = \frac{\omega_P}{\sqrt{1 + 2\epsilon_d}} \tag{1.3}$$

where ω_P is the plasma frequency of the metal. Relations (1.2) and (1.3) express one of the most significant features of metallic nanoparticles for practical applications. It indeed establishes that the position of the plasmonic resonance depends on the medium surrounding the nanoparticle: in particular, an increase in the dielectric constant of the surrounding medium leads to an increase in the nanoparticles absorption as well as a red shift of the plasmon absorption band maximum (see Figure 1.3). According to equation (1.2), the plasmon absorption is size-independent within the dipole approximation. However, a dependance of the particle absorption bandwidth on the particle size is experimentally observed: the bandwidth indeed decreases as the particle radius r (considering for simplicity a spherical particle) in-

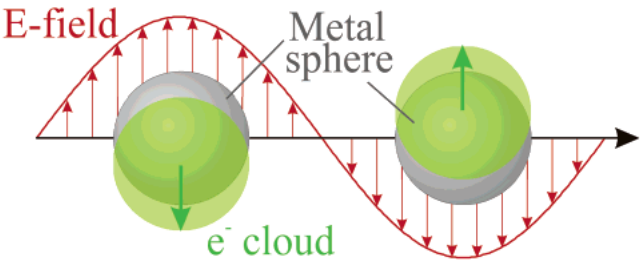

Figure 1.2: Schematic of a plasmon oscillation. Figure taken from Kelly et al. [30]

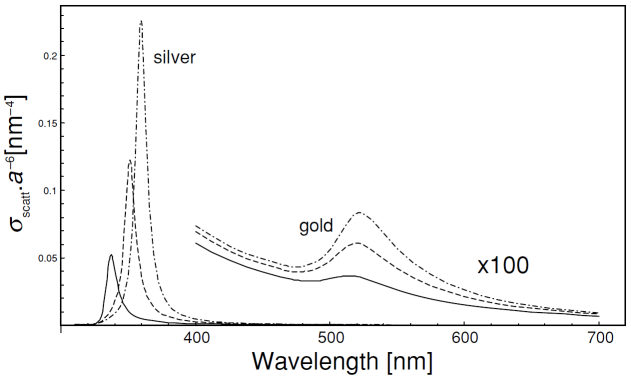

Figure 1.3: Scattering cross-section of spherical gold and silver particles in different environments normalized by a^6, with a denoting the particle radius. Solid line: vacuum (n = 1). Dashed line: water (n = 1.33). Dash-dotted line: glass (n = 1.5). Figure taken from Novotny and Hecht [42]

creases, following a $1/r$ law. This dependance, known as the *intrinsic size effect* (Link and El-Sayed [37]), is mainly due to the damping in the electron charge oscillations caused by the electron scattering from the particle boundaries.

For larger nanoparticles ($>$ 25 nm for Au nanoparticles [53]) the dipole approximation is no longer valid and electron oscillations of higher order occur. In this regime, an explicit size dependance of the extinction coefficient (as well as the resonance condition) appears (referred to as the *extrinsic size effect* [37]): a red shift of the resonance frequency is generally observed as the nanoparticle radius is increased, as shown in Figure 1.4a for the case of Au nanoparticles. For non spherical nanoparticles the description is more complex. In the case of oriented ellipsoidal particles, the dielectric function displays three different values along the three principal axes (Bohren and Huffman [7]). In the case of a nanorod-shaped metallic nanoparticle, the plasmon absorption band splits into two bands corresponding to the long (longitudinal) and short (transverse) axis of the rod, as shown for Au nanorods in Figure 1.4b. In general, manipulating the nanoparticles shape and size it is possible to tune the nanoparticle optical properties. This aspect is of course of great interest for plasmonics practical applications.

Another important feature characterizing the optical properties of metallic nanoparticles is the so called local-field enhancement [45]. This effect can be demonstrated by solving the Laplace equation ($\nabla^2\Phi = 0$) for the scalar potential of the incident wave in the region occupied by the nanoparticle (considered spherical to simply the calculations). Calculating

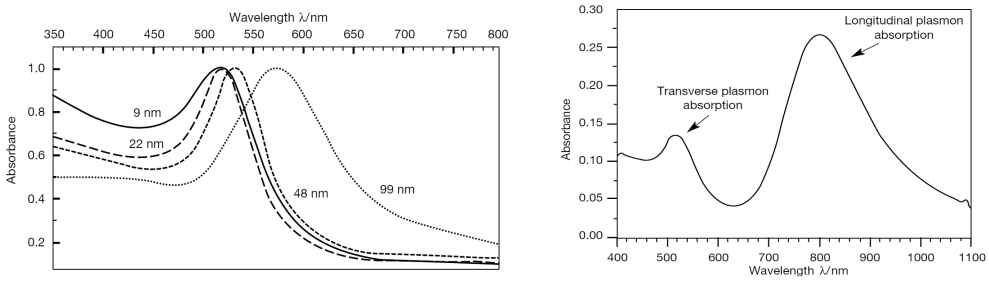

(a) **(b)**

Figure 1.4: Au nanoparticles size dependance of the plasmon resonance. (a) Optical absorption spectra of spherical nanoparticles of different radius. (b) Optical absorption spectra of nanorod-shaped nanoparticles. Both figures are taken from Link and El-Sayed [36].

the corresponding electric field configuration ($\mathbf{E} = -\nabla \cdot \Phi$), it is easily shown the presence of regions, localized in correspondence of the nanoparticle surface, characterized by a field amplitude greater than the incident one. This phenomenon can enhance the incident field by several orders of magnitude and, analogously to the traditional tip field enhancement, it was shown to be considerably larger for non-spherical nanoparticles than for comparable-sized spherical ones (Hao and Schatz [24]). The local field enhancement, along with the surrounding medium sensitivity and the optical properties tunability, constitutes one of the most appealing features of metallic nanoparticles for scientific and engineering applications, as will be pointed out hereafter.

One of the most known and well-established metal nanoparticles applications (Chang and Furtak [10]) is the Surface Enhanced Raman Spectroscopy (SERS), where the local field enhancement produced by the plasmonic excitation is exploited to measure Raman spectral lines for very small amount of probed sample: the enhancement can be high enough to observe Raman spectra even from a single molecule. As well as Raman spectroscopy, the field enhancement can contribute to enhance generic linear and nonlinear optical transitions in molecules within a nanoscopic distance from a metallic nanostructure. It has been used, for instance, to concentrate the local excitation density around a nearby fluorophore molecule, thus producing an enhancement of the fluorescence emission. This is only one of the possible plasmonic methods to manipulate the radiative decay properties of a fluorescent molecule: in general, they are referred to as *radiative decay engineering* (Lakowicz [34]). Other recent applications exploiting the local field enhancement include the usage of metallic nanoparticles for apertureless near-field microscopy and for the so called *plasmonic printing* used for photophabrication of nanostructures (Prasad [45]).

Another promising plasmonic application is in the field of optical wave guiding. In this case, a periodic array of metallic nanostructures embedded in a dielectric medium can be used to guide an optical electromagnetic wave in a regime dominated by near-field coupling (see Figure 1.5). The operation of such a wave guide relies on the fact that a plasmon oscillation in a single metallic nanoparticle can induce a plasmon oscillation in a closely spaced nearby one. This plasmon oscillation can thus propagate as a coherent mode along the array. The main advantages with respect to traditional optical wave guides are the possibility to confine the field over dimensions much lower than the wavelength of light (sub-wavelength confinement)

and to fabricate guiding paths featuring sharp bends without considerable leakage of light.

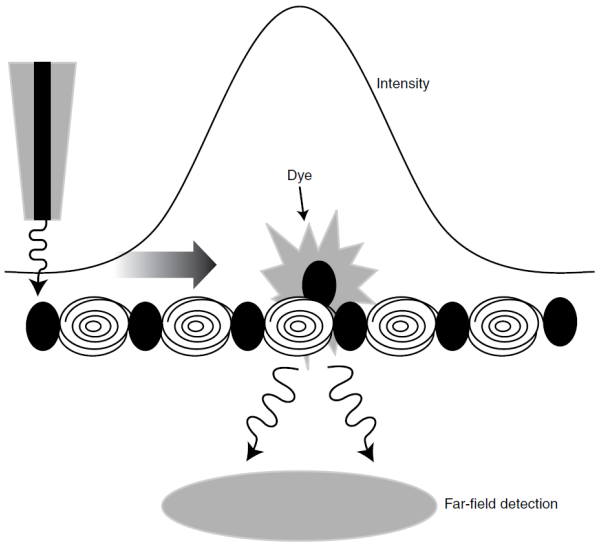

Figure 1.5: Schematic of plasmonic guiding and its use to generate fluorescence excitation in a dye. Figure taken from Maier et al. [39].

However, one of the most significant plasmonic applications is represented by the usage of metal nanostructures as sensors for detection of biological analytes. This application relies on the sensitivity on the surrounding dielectric of the plasmon resonance frequency given by the Fröhlich condition. A biological molecule which binds to the surface of a metallic nanoparticle produces a change in the dielectric environment that can be detected by measuring the corresponding resonance shift. The field of plasmonic biosensing application is quite wide and an extensive discussion can be found elsewhere (Prasad [45]).

Metallic nanoparticles can also be used for applications not directly related to their plasmon resonance: among all the others, they are of particular interest for the catalysis of chemical reactions. Catalysis is a fundamental stage of the fabrication process of many different industrial products. Most of the catalysts used nowadays consist of nanometer-sized particles dispersed on a high surface area support. The properties of such nanoparticles influence their catalytic performance and are thus of great interest both for science and industrial applications. For the case of the Au for example, while in the bulk form it tends to be inert, when arranged in nanometer-sized particles it has been proved to act as a highly efficient catalyst ([12], [3], [52], [38]).

The common feature to most of the applications presented is the great importance of the nanoparticles morphology and structure. These aspects are thus worth investigating in order to control the nanoparticles performances and to gain a deeper understanding of the nanoparticles formation process; the latter mainly depends on the preparation method exploited. Different methods have been explored for the fabrication of metallic nanoparticles so far (a detailed discussion is provided by Pelton et al. [44]). The most common way is based on lithographic techniques, such as optical or electron beam lithography (EBL). These techniques have the great advantage to be well established scaled-up fabrication processes, owing to their massive usage in the semiconductor devices industry. They allow to produce

a large number of 2D structures with a variety of different shapes, thus providing great flexibility. Nevertheless, it is difficult to produce features with dimensions below 5-10 nm and the high-quality needed for the exploitation of the plasmonic effect is still hard to achieve. The lithographically printed nanostructures are generally polycristalline, whose grains size, orientation and arrangement are not well controlled: this leads to nanostructure with a great surface roughness and size and shape dispersion. Different chemical fabrication processes have been used as an alternative to lithography. They guarantee the production of single crystal nanoparticles with nearly atomically smooth surfaces; on the other hand, the nanoparticles are in this case difficult to arrange in a predefined pattern and they are normally randomly distributed. In the next section a novel in-situ fabrication method will be presented, along with its main advantages for technological applications.

1.2 Monocrystalline gold nanoparticles embedded in a $SrTiO_3$ thin film: sample preparation and potentialities for technological applications

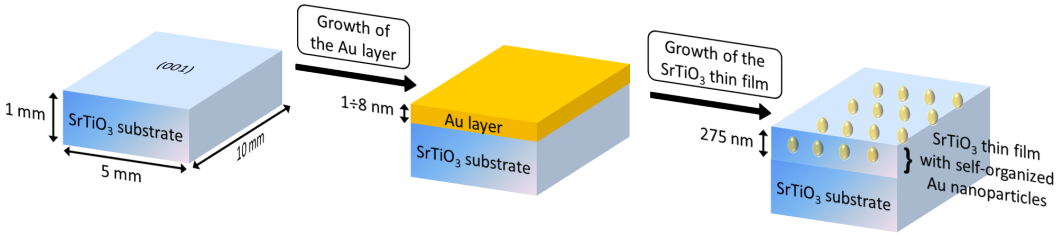

Figure 1.6: Schematic of the samples preparation steps.

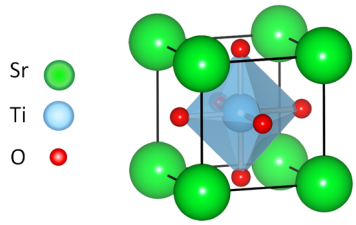

Figure 1.7: $SrTiO_3$ perovskite structure.

The samples object of the present work were kindly provided by the Institute of Solid State Physics of the Friedrich-Schiller-University in Jena, Germany. They are composed of self-organized monocrystalline Au nanoparticles embedded in a strontium titanate matrix (Christke et al. [13] and Katzer et al. [29]). They are obtained by a novel two steps deposition process, as displayed in Figure 1.6, performed on a single crystal strontium titanate commercial substrate (1 x 5 x 10 mm^3). Strontium titanate is a ceramic oxide with chemical formula $SrTiO_3$ (frequently abbreviated with STO). At room temperature it is a centrosymmetric paraelectric material and exhibits the well known cubic perovskite structure (see Figure 1.7) which belongs to the $Pm\bar{3}m$ space group. It is a widely documented compound in literature

as well as a very commonly used substrate for several type of thin film systems. For the case under study the three substrate facets were cut along the three main cubic axes (see Figure 1.8): from now on the normal to the growth direction will be labeled (001). Au thin films with thickness varying between 1 and 8 nm (namely 1, 1.5, 2, 3, 4, 5, 5.3 and 8 nm) were deposited on the ultrasonically cleaned substrate surface under high vacuum condition using magnetron sputtering (see Figure 1.9a) in an Ar atmosphere of $16 \cdot 10^{-4}$ Torr (1 Torr $\approx$ 133 Pa). The Au coated samples were then heated to 1070 K for 5 minutes: this annealing step causes the Au layer to thermally dewet: as a consequence, approximately hemispherical 3D islands are formed, as shown in Figure 1.10. Following the annealing process, a deposition

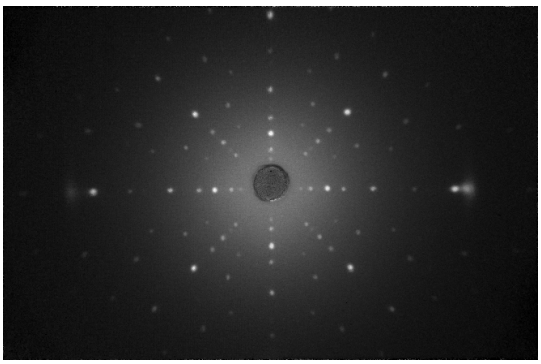

Figure 1.8: Substrate Laue picture. The cut of the crystal along the three main cubic axes is confirmed by the 4-fold symmetry of the spots. The image was recorded through a standard Laue back-reflection laboratory setup.

of a STO thin film with a fixed thickness value of 275 nm was carried out through the Pulsed Laser Deposition (PLD) setup of Figure 1.9b in an oxygen rich atmosphere of 100 Pa. Using a KrF excimer laser ($\lambda = 248$ nm, $\tau = 25$ ns) at a repetition rate of 5 Hz and a laser fluence of 1.5 J/cm^2 yielded a growth rate of 11 nm/min. After the STO layer was deposited, the samples were cooled to room temperature at a rate of 50 K/min in an oxygen atmosphere of 200 Pa. Further details on the sample preparation process can be found in the work of Bernhardt [4].

During the deposition of the STO thin film, the Au dewetted layer self-assembles to homogeneously arranged monocrystalline nanoparticles mostly located at a characteristic depth within the deposited STO layer. They generally exhibit an ellipsoidal shape, with the major axis (c axis) directed normally to the growth direction (see Figure 1.11). The production of nanostructure with such an anisotropic shape is of great interest for practical application, especially in the field of biological molecules sensors. The anisotropy promises a greater detection sensitivity owing to the corresponding increased local field enhancement with respect to spherical nanostructures (see previous section). For one of the samples investigated (namely the one with 5 nm of Au), the STO thin film deposition was not realized: as will be shown in Chapters 4 and 5, this sample will allow to compare the properties of the nanoparticles with those of the 3D islands present after the annealing step. Figure 1.12 displays the photos of the samples with different initial Au layer thickness values and STO top layer. The colors they exhibit (more intense as the amount of deposited Au increases) are due to the nanoparticles plasmon resonance as for Figure 1.1. Although some inhomogeneities

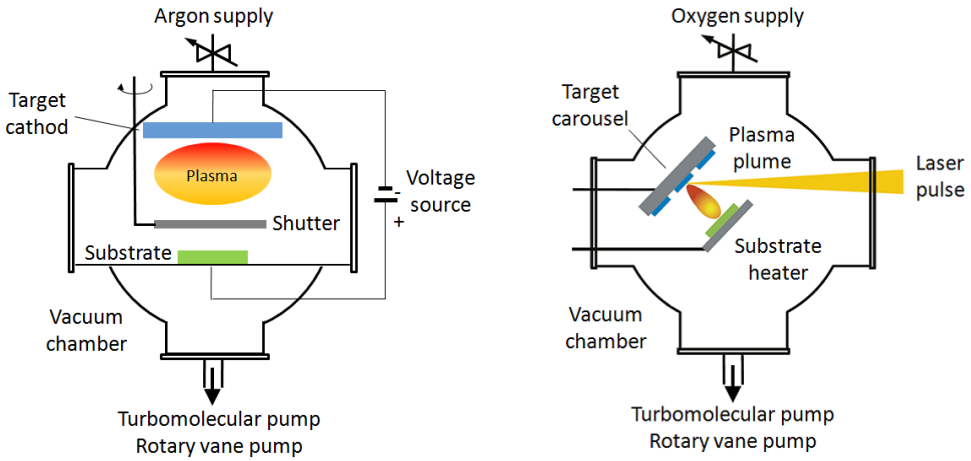

Figure 1.9: Schematics of the experimental setups used for the samples preparation. (a) Magnetron sputtering used for the growth of the Au layer. (b) Pulsed Laser Deposition (PLD) used for the growth of the STO thin film.

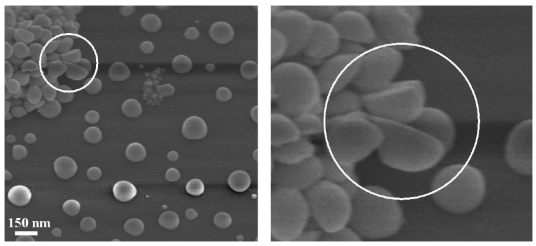

Figure 1.10: Scanning electron microscopy images of Au 3D islands formed by the thermal dewetting of the Au layer. The hemispherical shape derives from the former island/substrate interface. Figure taken from Katzer et al. [29]

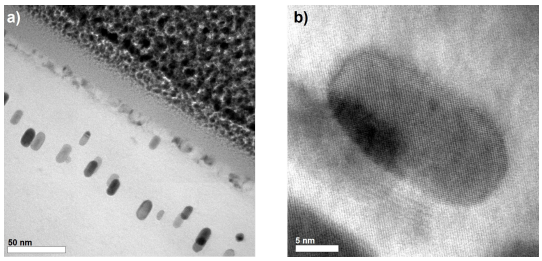

Figure 1.11: Transmission electron microscopy images of the embedded Au nanoparticles. The images refer to samples prepared similarly to the ones considered in the present work. (a) Characteristic alignment of gold nanoparticles within a STO matrix, here with a film thickness of 140 nm and a Au layer thickness of about 1 nm. (b) High resolution image of a Au crystallite. Figure taken from Christke et al. [13]

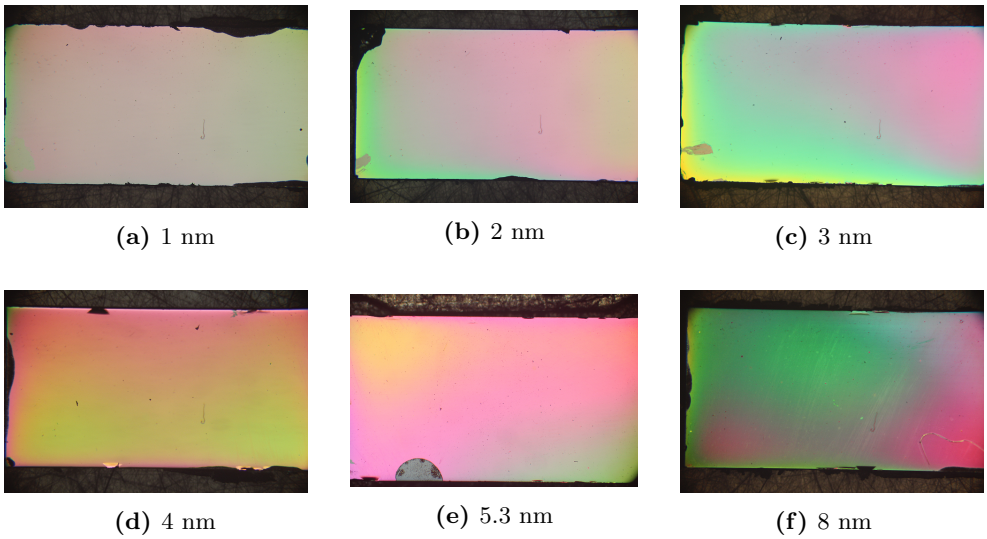

(a) 1 nm **(b)** 2 nm **(c)** 3 nm

(d) 4 nm **(e)** 5.3 nm **(f)** 8 nm

Figure 1.12: Photos of the samples with different initial Au layer thickness values and $SrTiO_3$ top layer.

are present, each sample can be considered sufficiently spatially uniform for the investigation presented in the present work. Nevertheless the probed region was precautionary kept roughly in the center to avoid possible defects localized near the borders.

As mentioned, contrary to what observed for other thin film materials [23] (where the Au nanoparticles preferentially grow at the film surface or the film/substrate interface), most of the Au nanoparticles are found within the STO layer. As shown by Christke et al. [13], the characteristic depth at which the nanoparticles are located seems to be correlated with the thickness of the STO layer: increasing the film thickness leads to a greater distance between the nanoparticles and the film/substrate interface. More relevantly, the film thickness was found to influence the nanoparticle shape: as the thickness increases a smaller aspect ratio c/a is observed, leading to more spherical nanostructures. Au nanoparticles with an aspect ratio c/a of 2:1 and typical dimensions of about 8-11 nm for the a axis and 17-23 nm for the c axis were found, for the initial Au layer thickness of about 1 nm probed by Christke et al. [13]. An opposite effect is produced by a variation of the initial Au layer thickness. A continuous enhancement of the aspect ratio from 1:2.5 to 1:3.2 varying the Au thickness from 4 to 8 nm was observed from Katzer et al. [29] for the same samples object of the present study. A consistent trend also emerged for the other Au thickness values considered, as shown by Bernhardt [4]. Furthermore, a greater Au layer thickness generally implies the formation of nanoparticles with a greater volume. These shape and size changes directly influence the optical properties of the Au nanoparticles. A clear example is provided by the extinction measurements shown in Figure 1.13: multiple extinction maxima are observed, as expected for rod-like nanoparticles (see Figure 1.4b) and the greater peak exhibits a red shift as the Au layer thickness is increased. This is consistent with the aforementioned trend for the size and the shape of the nanoparticles.

In summary, the two steps deposition process presented in the present section represents a promising alternative to the methods traditionally used for nanoparticles fabrication. It

indeed allows to obtain monocrystalline anisotropic nanoparticles, tunable in size and shape by simply modifying the growth conditions, without the necessity of expensive lithographic facilities or of laborious chemical processes (more complex if anisotropic nanoparticles have to be fabricated). Moreover, the possibility of a selective etching of the STO matrix has already been proved (Katzer et al. [29]), thus allowing to expose the nanoparticle to air. This in turn would make possible the adsorption of biological molecules at the smallest radii of the nanostructures where the maximum amplitude of the electric field of the plasmonic excitation is localized. Au nanoparticles prepared in an analogous way have also been used as flux pinning centers for high temperature superconducting YBCO thin film (Grosse et al. [23] and Katzer et al. [28]): in this case the embedded nanoparticles allow to reduce the dissipative losses caused by the movement of the magnetic vortices present in high temperature superconductors. The influence of the nanoparticles presence on the YBCO grain boundaries has also been exploited for the engineering of Josephson junctions (Michalowski et al. [40]).

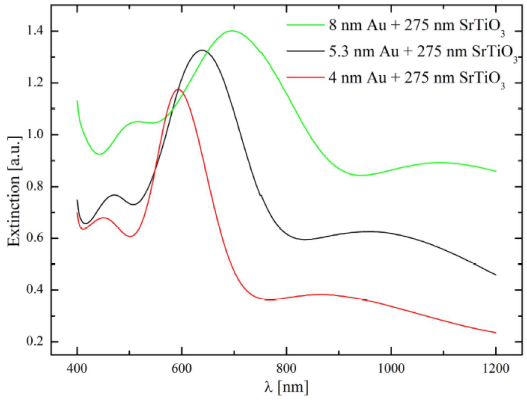

Figure 1.13: Extinction spectra of the embedded Au nanoparticles for different values of the Au seed layer thickness. Figure taken from Katzer et al. [29].

Despite the great potentialities just pointed out, little is known about the growth process leading to the Au nanoparticles formation as well as the structural properties of both the nanoparticles and the STO thin film. These properties are not only important for the potential practical applications of this kind of systems, but are also of great relevance for the physics involved in the growth of metals on ceramic substrates, still not widely explored (especially for the case of the Au). The influences of the nanoparticles on the surrounding STO structure are particularly important for the cases where the nanoparticles are used to modify the properties of the ambient medium, as for the application as flux pinning centers. The present work precisely aims to fill this gap of knowledge, by presenting an investigation of the crystallographic properties of such a system performed by means of X-ray diffraction. An introduction to the basics concepts which the latter technique is based on will be provided in the following chapter, as well as an overview of the crystallographic properties of similar systems. The discussion of the experimental results will be then undertaken in Chapters 4 and 5, after the presentation of the experimental setup (Chapter 3).

Chapter 2

Theoretical background

In this chapter, the most relevant theoretical concepts which the present work is based on are introduced. Most of these concepts are extensively used throughout the discussion of the experimental data provided in Chapters 4 and 5. In Section 2.1 the basic principles underlying the experimental technique exploited for the sample investigation, namely X-ray diffraction, are outlined. Section 2.2 provides a general overview of the physical background and the phenomenology of the growth process of metal thin films on ceramic substrates, along with a summary of the main experimental results found in literature for the $Au/SrTiO_3$ system. Finally, in Section 2.3, a detailed discussion about the mathematical description of the various steps involved in the study of the texture properties of a given material is presented. In this section the conventions about the coordinate systems and the names of the angles used in the subsequent chapters are introduced: their knowledge is needed for a complete understanding of the data analysis and the experimental results discussed in Chapters 4 and 5.

2.1 X-ray scattering by atoms and crystals

Figure 2.1: *Hand mit Ringen* (Hand with Rings): print of Wilhelm Röntgen's first "medical" X-ray picture of his wife's hand, taken on 22 December 1895 [49].

Since the first observation of X-rays by Wilhelm Conrad Röntgen in 1895 (first Nobel prize in physics in 1901), a great understanding has been gained of the properties of X-ray electromagnetic radiation and its interaction with matter. Nowadays, X-rays are a widely used investigation probe in many different fields of research. One of the most widespread and significant applications is the X-ray crystallography, which exploits the diffraction of X-ray radiation produced by periodic atom arrangements for the study of crystal structures in solid state physics.

An X-ray beam incident on a certain material undergoes many different types of interaction phenomena, that are extensively described in the dedicated literature. The one of interest for the present work is the coherent scattering by the electrons of the material atoms. This can be fully understood by means of a classical picture, starting from the case of a single free electron, commonly known as *Thomson scattering*. The electric field of the incident X-ray results in an acceleration of the electron, which causes it to oscillate along the direction of oscillation of the incident field. The oscillating electron, in turn, becomes a source of electromagnetic radiation and it radiates transverse electromagnetic waves around it. Considering a point at a distance R from the electron, the electric field of the scattered radiation lies in the plane of R and the electron acceleration vector $\mathbf{a}$. In terms of the more convenient *cgs* units, the corresponding intensity I is given by

$$I = I_0 \frac{q^4}{m^2 c^4 R^2} \sin\alpha \tag{2.1}$$

where I_0 is the incident intensity, q is the electronic charge (negative), m is the electronic mass and α is the angle between R and the direction of oscillation of the electron. The previous formula states that the scattered intensity is maximum for the waves propagating in the plane normal to the oscillation direction and vanishes along it. For an unpolarized incident beam, an average of equation (2.1) over all possible transverse directions for the electric field leads to the Thomson scattering equation:

$$I = I_0 \frac{q^4}{m^2 c^4 R^2} \frac{1 + \cos^2 2\theta}{2} \tag{2.2}$$

being 2θ the angle between the incident and scattered wave vectors. $\frac{1+\cos^2\phi}{2}$ is often referred to as the *polarization factor* since it is related to the change in magnitude of the electric vector lying in the plane containing the scattering angle 2θ. For $2\theta = 90°$, a linearly polarized scattered wave results.

The scattered intensity by the collection of electrons in an atom is the result of the interference of the waves scattered by each electron. If the X-ray wavelength λ is much smaller than any of the absorption edge wavelengths in the atom (large incident photon energies), the electrons can be treated as free: in this case the Thomson scattering equation can be applied for the intensity scattered by each electron. It is convenient to define the so called *atomic scattering factor* f (also known as *atomic form factor*) as the ratio between the electric field amplitude scattered by an atom E_a and that scattered by an isolated free

electron E_e:

$$f = \frac{E_a}{E_e} \tag{2.3}$$

The maximum value for f is given by the atomic number Z. It occurs when all the electrons of the atom scatter in phase with each other: this happens only when the forward scattering direction is considered. A complete derivation of the expression of the atomic scattering factor according to a classical wave mechanical treatment can be found elsewhere (e.g. Warren [56] and Azaroff [2]). Calling $\mathbf{K}_{in}$ and $\mathbf{K}_{out}$ the wave vectors of the incident and scattered waves respectively and $\mathbf{r}$ the position vector with respect to the reference system chosen, the atomic scattering factor is given by

$$f = \int \exp\left[i(\mathbf{K}_{out} - \mathbf{K}_{in}) \cdot \mathbf{r}\right] \sum_n \rho_n(\mathbf{r})\, d\mathbf{r} = \int_0^\infty 4\pi r^2 \sum_n \rho_n(r) \frac{\sin Hr}{Hr}\, dr \tag{2.4}$$

Here $H = \frac{4\pi \sin\theta}{\lambda}$ represents the modulus of the momentum transfer $\mathbf{H} = \mathbf{K}_{out} - \mathbf{K}_{in}$ of the scattering process and ρ_n is the charge density associated to the n-th electron of the atom normalized to the electronic charge q ($\int \rho_n(r)\, dr = 1$). The second equality is obtained by expressing the first volume integral in spherical coordinates and it is valid only for spherically symmetrical electron charge distributions. From the previous formula, the atomic scattering factor is known once the radial dependence of the electron charge density $\sum_n \rho_n(r)$ is available. The electron charge density satisfies the following condition

$$\int_0^\infty 4\pi r^2 \sum_n \rho_n(r)\, dr = Z \tag{2.5}$$

For any element, f is a function of $\sin\theta/\lambda$ and it approaches Z at small value of $\sin\theta/\lambda$ (see Figure 2.2). Since f is a ratio of field amplitudes, the scattered intensity by an atom is proportional to $|f|^2$. If the hypothesis of an incident wave wavelength much smaller than any of the absorption edge wavelengths in the atom is no more valid, a complex dispersion correction has to be taken into account and the expression for the atomic scattering factor modifies as follows

$$f = f_0 + \Delta f'(E) + i\Delta f''(E) \tag{2.6}$$

where f_0 is the atomic scattering factor far away from the absorption edges and $\Delta f'(E)$ and $\Delta f''(E)$ are the real and imaginary part of the dispersion correction respectively, both dependent on the incident photon photon energy E (see Figure 2.3). A detailed derivation of equation (2.6) can be found in Azaroff [2].

When a great number of atoms are periodically arranged in a crystal structure, the incident X-ray beam will give rise to multiple peaks of scattered radiation along particular directions in space: these peaks constitute the so called X-ray diffraction (XRD) pattern of the sample and their positions carry information about the atoms spatial arrangement of the particular crystal structure considered. The study of the atomic and molecular structure of crystalline samples represents the principal interest of that wide field of research known as *X-ray crystallography*. This technique traces back to the beginning of the 20th century when a diffraction diagram of a copper sulfate crystal was first recorded by Friedrich et al. [17].

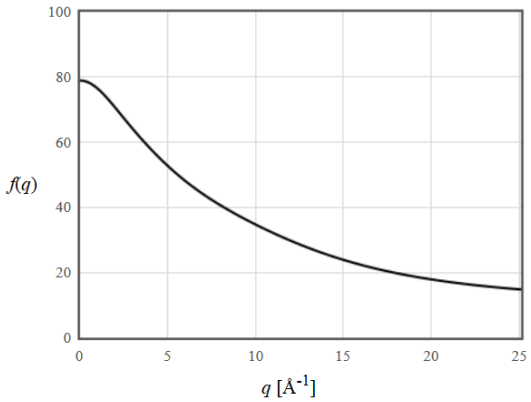

Figure 2.2: Au atomic scattering factor as a function q (the quantity called H in equation (2.4)). Figure taken from [43].

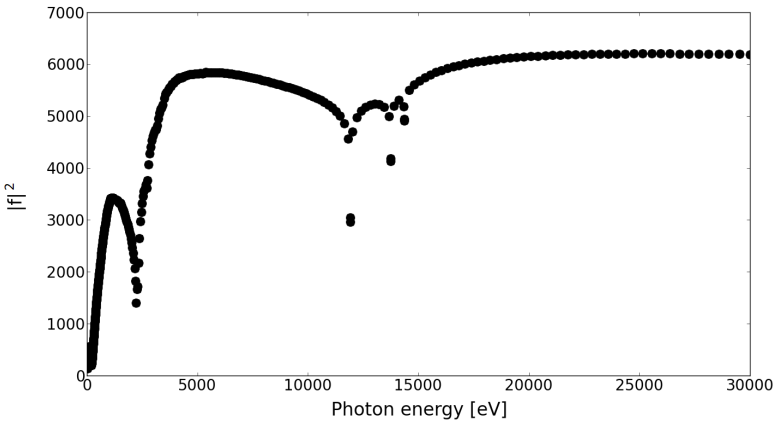

Figure 2.3: Modulus squared of the Au scattering form factor including the dispersion correction as a function of the incident beam energy. The depressions are due to the Au absorption edges. Atomic form factor values taken from [48].

A diffraction pattern arises from the superposition of the electromagnetic waves scattered by each atom of the crystal: whenever the scattered waves constructively interfere, an intense beam of diffracted radiation results. The requirement for constructive interference to occur is given by the well known Laue diffraction condition (Max von Laue, 1912):

$$\mathbf{K}_{out} - \mathbf{K}_{in} = \mathbf{Q} \tag{2.7}$$

where $\mathbf{Q}$ is one of the vectors of the reciprocal lattice. Given a crystal structure whose underlying Bravais lattice [1] is generated by the three base vectors $\mathbf{a}$, $\mathbf{b}$ and $\mathbf{c}$, the corresponding reciprocal lattice originates from the following three base vectors

$$\begin{aligned} \mathbf{a}^* &= 2\pi \frac{\mathbf{b} \times \mathbf{c}}{\mathbf{a} \cdot (\mathbf{b} \times \mathbf{c})} \\ \mathbf{b}^* &= 2\pi \frac{\mathbf{c} \times \mathbf{a}}{\mathbf{b} \cdot (\mathbf{c} \times \mathbf{a})} \\ \mathbf{c}^* &= 2\pi \frac{\mathbf{a} \times \mathbf{b}}{\mathbf{c} \cdot (\mathbf{a} \times \mathbf{b})} \end{aligned} \tag{2.8}$$

such that a general reciprocal lattice vector $\mathbf{Q}$ can be expressed as $\mathbf{Q} = h\mathbf{a}^* + k\mathbf{b}^* + l\mathbf{c}^*$, with h, k and l being the well known Miller indices. The Laue diffraction condition can be very simply and intuitively represented by the famous Ewald construction (Paul Peter Ewald, 1913) , displayed in Figure 2.4. It shows that, for a given incident wave vector $\mathbf{K}_{in}$, a beam of diffracted radiation is observed for every reciprocal lattice point lying on the Ewald sphere. This is the sphere passing through the reciprocal space origin and with radius equal to $|\mathbf{K}_{in}|$. The corresponding diffracted wave vector is obtained connecting the center of the sphere with the reciprocal lattice point considered.

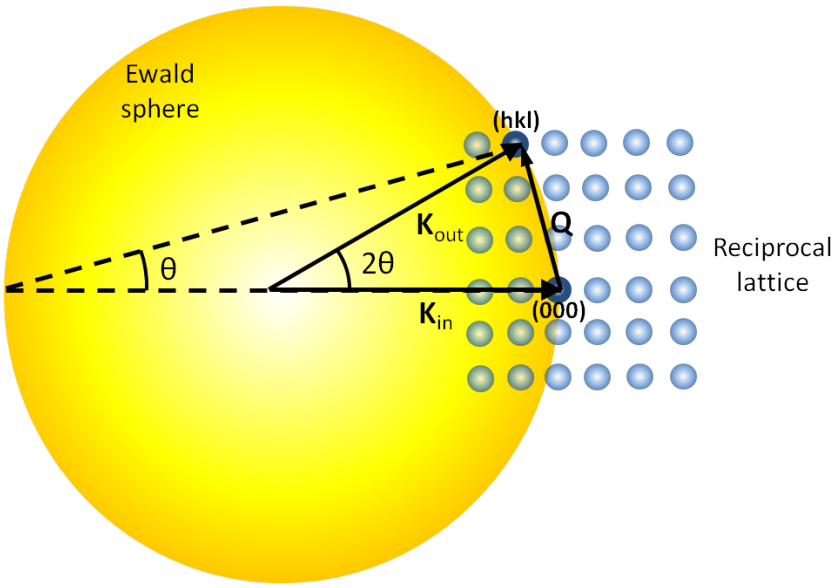

Figure 2.4: Ewald construction.

An alternative, but equivalent (as demonstrated in Ashcroft and Mermin [1]), condition to the Laue one for the constructive interference of the waves scattered by the crystal atoms was provided in 1913 by W.L.Bragg and his father W.H.Bragg, leading to the famous Bragg formula. It states that for a given family of crystalline planes with a certain value of the interplanar spacing d, constructive interference occurs when the angle θ between the planes and the incident wave vector satisfies the following

$$n\lambda = 2d\sin\theta \qquad n = 1, 2, 3, \ldots \tag{2.9}$$

The interplanar spacing d_{hkl} of a certain family of crystalline planes (hkl) is inversely proportional to the modulus of the shortest reciprocal lattice vector $\mathbf{Q}_{hkl}$ normal to the planes, of components h, k and l:

$$d_{hkl} = \frac{2\pi}{|\mathbf{Q}_{hkl}|} \tag{2.10}$$

In the case of a (simple) cubic crystal, $|\mathbf{a}^*| = |\mathbf{b}^*| = |\mathbf{c}^*| = 2\pi/a$, with a being the side of the cubic unit cell, and the previous formula leads to the following

$$d_{hkl} = \frac{a}{\sqrt{h^2 + k^2 + l^2}} \tag{2.11}$$

For a crystal structure where the periodic atoms arrangements can be described by a monoatomic basis (see Ashcroft and Mermin [1] for further details), equation (2.7) can be directly use to predict the occurrence of peaks of diffracted radiation. On the contrary, in the case of a polyatomic basis, the interference between the waves scattered by the different atoms within the basis has to be taken into account. This leads to a $\mathbf{Q}$ dependence of the diffracted intensity, which, for a certain reciprocal lattice vector $\mathbf{Q}_{hkl}$, turns out to be proportional to the so called structure factor F_{hkl}, given by the following

$$F_{hkl}(\mathbf{Q}_{hkl}) = \sum_{n}^{N} f_n(\mathbf{Q}_{hkl}) \exp\left[i\mathbf{r}_n \cdot \mathbf{Q}_{hkl}\right] \tag{2.12}$$

where f_n is the atomic scattering factor of the n-th atom of the basis (defined by equation (2.3)) and $\mathbf{r}_n$ is its corresponding position vector in the cell. The summation is done over all the N atoms which form the basis. For a polyatomic basis containing different atomic species F_{hkl} is in general different from zero, unless there is some fortuitous relation between the form factors of the different atoms. On the other hand, in the case of the presence of a single element (f_n is a constant that can be taken out from the summation (2.12)), the atoms in the basis can be arranged such that a complete destructive interference occurs for certain values of $\mathbf{Q}_{hkl}$. In this case the structure factor vanishes and the corresponding diffraction peak is not observed. This also happens in the case of a monoatomic basis for body or face centered Bravais lattices. With regard to the case of a face centered cubic (FCC) lattice (of interest for the present work, since the Au exhibits this ordering) the structure factor is given

by

$$F_{hkl} = f\left[1 + e^{i(h+k)\pi} + e^{i(h+l)\pi} + e^{i(k+l)\pi}\right] = \begin{cases} 4f & h,k,l \text{ all even or all odd} \\ 0 & h,k,l \text{ both even and odd} \end{cases} \quad (2.13)$$

Only the crystalline planes with all even or all odd Miller indices give then rise to a diffraction peak. For the expression of the structure factor for other crystal structures the reader should refer to the dedicated literature.

2.2 Crystallographic properties and surface morphology of FCC metals deposited upon single crystal ceramic substrates

In the present section a brief overview of the structural and morphological properties of face centered cubic (FCC) metals deposited on single crystal ceramic substrates is presented. Most of the discussion is of course centered on Au thin films deposited on a $SrTiO_3(001)$ single crystal substrate. The interest of such a system for the present work is justified by the fact that it actually constitutes the result of the first deposition step described in Section 1.2: it thus represents the starting point of the Au nanoparticles formation process. Much research has been devoted to the study of FCC metal heteroepitaxy on (001)-oriented ceramic substrate. However, the general characteristics of the metal/ceramic interface are still not well understood. Most of the work present in literature deals with Pt films: a much smaller number is dedicated to the epitaxial growth of other FCC metal, especially Au. Hereafter, a brief description of the main parameters which impact the metal film growth along with a round up of the most relevant experimental results concerning Au films grown on a $SrTiO_3(001)$ substrate can be found.

The structure and the morphology of a metal thin film (and thin films in general) are the result of an intricate combination of several thermodynamic and kinetic factors, which are in turn strongly affected by the growth processing conditions, particularly the deposition temperature. Therefore a theoretical prediction of the thin film structural and morphological properties resulting from the growth is in most cases unfeasible. The three main factors affecting thin film epitaxy are: the metal surface energy anisotropy, the interfacial energy between the film and the substrate and the surface diffusion of the metal atoms.

The surface energy γ_{hkl} of the (hkl) bulk termination of a crystalline solid is defined as the energy per unit area necessary to cut the perfect infinite crystal along the (hkl) crystallographic planes. As everybody knows, the surface energy of a crystalline material is in general strongly anisotropic, since it depends on the crystallographic direction chosen. In the case of a FCC metals the closed packed $\{111\}$ planes have the lowest surface energy: therefore FCC metals naturally prefer to grow with a $\{111\}$ orientation relative to the substrate surface. To achieve epitaxy along another orientation (i.e. the (001), which is of interest for the present work), the natural tendency to grow along the $\{111\}$ direction must be overcome by a second factor, normally an energetically favorable interfacial relationship with the substrate surface.

The surface energy anisotropy decreases as the temperature increases (up to the fully isotropic liquid state): at elevated temperature the preference of a FCC metal to grow along the {111} direction diminishes and (001) epitaxy can thus be achieved. There is no wide agreement on the absolute values of the FCC metals surface energy in literature. Concerning Au (the only FCC metal, together with Pb, for which reliable equilibrium crystal shape data are available), an experimentally determined value of 1.040 for the ratio $\gamma_{001}/\gamma_{111}$ at 1123 K is reported in the work of Wang and Wynblatt [55]. This is greater than the corresponding values of 1.004 and 1.025 reported respectively in [11] and [26] for Cu and Pb.

The second important factor in thin film heteroepitaxy is the interfacial energy $\gamma_{M/S}$ between the metal and the substrate surface. As mentioned, a low interfacial energy can induce the FCC crystal growth to deviate from the {111} direction. It is also involved in the thermodynamical relation used to determine which of the various possible growth modes tends to occur for a certain metal/substrate pair. Labeling with γ_M and γ_S the metal and substrate surface energies respectively, if

$$\gamma_{M/S} > \gamma_S - \gamma_M \tag{2.14}$$

the metal/substrate interface is energetically unfavourable: 3D metal islands will thus tend to cluster (Volmer-Weber growth mode), leaving regions of clean substrate surface between. This generally occurs for transition metals on ceramic surfaces, as extensively discussed in the work of Campbell [9], and in particular on $SrTiO_3$ surfaces [54]. If, on the other hand, $\gamma_{M/S} \leq \gamma_S - \gamma_M$, the metal atoms will tend to wet the substrate surface (Frank - van der Merwe growth mode) and a continuous metal film will thus result. The work of Wagner et al. [54] has shown that the interface energy is mainly influenced by two factors: the oxygen affinity (P_0) and the lattice mismatch (f). Investigating the growth of different transition metals on a $SrTiO_3$(001) substrate, the authors proposed an epitaxial phase diagram (Figure 2.5a) based on these two quantities: different regions corresponding to different structural properties of the resulting overlayer metal are highlighted. In that work is explained that the growth of a crystalline epitaxial layer is favored for metals with low lattice mismatch and high oxygen affinity. Lattice mismatch has then been demonstrated to have a minor role (Francis and Salvador [16]) and the new phase diagram of Figure 2.5b has been proposed. In both the aforementioned works, Au was found to belong to the polycrystalline growth region, mainly as a consequence of its low oxygen affinity.

The surface energy anisotropy and the interfacial energy primarily deal with the metal crystalline orientation, that is to say its structure. Although the metal overlayer growth mode is governed by energy balances like the one of equation (2.14), its final morphology is strongly influenced by a kinetic factor, the surface diffusion D_S of the metal adatoms. This is in turn strongly dependent on the growth temperature, as expressed by the empirical relation found by Gjostein [21]:

$$D_S = 0.014 \exp \frac{-13 T_M}{2T} \tag{2.15}$$

where T_M is the metal melting point. As the growth temperature increases, the thermal kinetic energy available for the metal adatoms to diffuse on the surface increases and so does

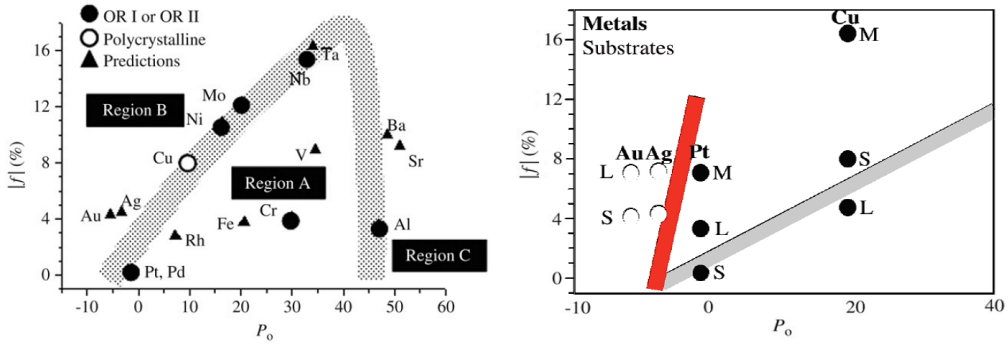

(a) (b)

Figure 2.5: Phase diagram displaying different metals deposited on $SrTiO_3(001)$ as a function of both the oxygen affinity P_0 and the lattice mismatch f. For each metal investigated, the corresponding crystal structure is shown. (a) Phase diagram as reported by Wagner et al. [54]. Three different regions are proposed. Region A: epitaxial growth of metals. Region B: polycristalline growth of metals. Region C: chemical reaction of metals. OR I and OR II correspond to two different crystal orientation of the metal with respect to the substrate: they are defined by the relations (2.16). (b) Phase diagram as reported by Francis and Salvador [16]. The grey line corresponds to the epitaxial/polycrystalline regions boundary of Figure 2.5a: the new boundary proposed is represented by the steep red line. The letters M, S and L stands for different substrate material, namely (in the order) $MgO(001)$, $SrTiO_3(001)$ and $LaAlO_3(001)$.

the diffusion coefficient. The diffusion coefficient is a measure of the mobility of the metal adatom on the substrate surface: the higher the diffusion coefficient the more the adatoms are inclined to move. The diffusion coefficients as a function of the growth temperature for four different FCC metals are reported in Figure 2.6. As previously mentioned, thermodynamic

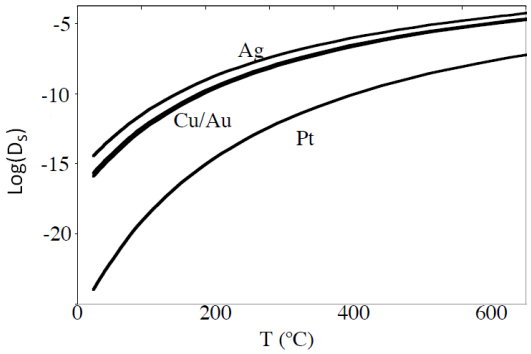

Figure 2.6: Surface diffusion coefficients as a function of the growth temperature for four different FCC metals as given by equation (2.15). Figure taken from Francis and Salvador [16].

considerations of the surface and interfacial energies indicate that, in most cases, transitions metals should not wet ceramic surfaces, instead forming 3D islands. However, this can actually occur only if the diffusion coefficient is big enough to allow the adatoms to freely diffuse over distances large enough for the 3D islands to form. If the temperature is not high enough for this to happen, the Frank-van der Merwe growth mode can prevail, thus resulting in a continuous metal film. As a general guideline, the root mean square metal surface roughness increases as the diffusion coefficient increases [16]. The diffusion coefficient also impacts the crystal structure of the metal overlayer since fast diffusion coefficients at high

temperature allow the metal adatoms to easily locate their preferred crystalline orientation.

A summary of the epitaxial relations between overlayers of different metals grown on $SrTiO_3(001)$ can be found in Table 6 of the work of Fu and Wagner [19]. As reported in this work, in the case of a TiO_2-terminated $SrTiO_3(001)$ surface, the low interface energy tends to stabilize the following two epitaxial relations (respectively called **OR I** and **OR II** in [19]):

$$\begin{aligned} &(001)_{SrTiO_3} \,||\, (001)_M \;,\; [100]_{SrTiO_3} \,||\, [100]_M \quad \text{“cube on cube”} \\ &(001)_{SrTiO_3} \,||\, (001)_M \;,\; [100]_{SrTiO_3} \,||\, [110]_M \quad \text{“cube on cube with 45° rotation”} \end{aligned} \tag{2.16}$$

where the subscript “M” refers to a generic FCC or BCC metal. The previous notation for the epitaxial orientations, commonly found in literature, is composed by two parts: the first one indicates the vertical direction of growth (that is to say the one normal to the metal/substrate interface), while the second defines the in-plane metal crystal orientation. If $SrTiO_3(001)$ is SrO-terminated, in the case of an FCC metal the following orientation has been observed: $(001)_{SrTiO_3} \,||\, (111)_{FCC-M}$, $[100]_{SrTiO_3} \,||\, [110]_{FCC-M}$ (**OR V** in [19]).

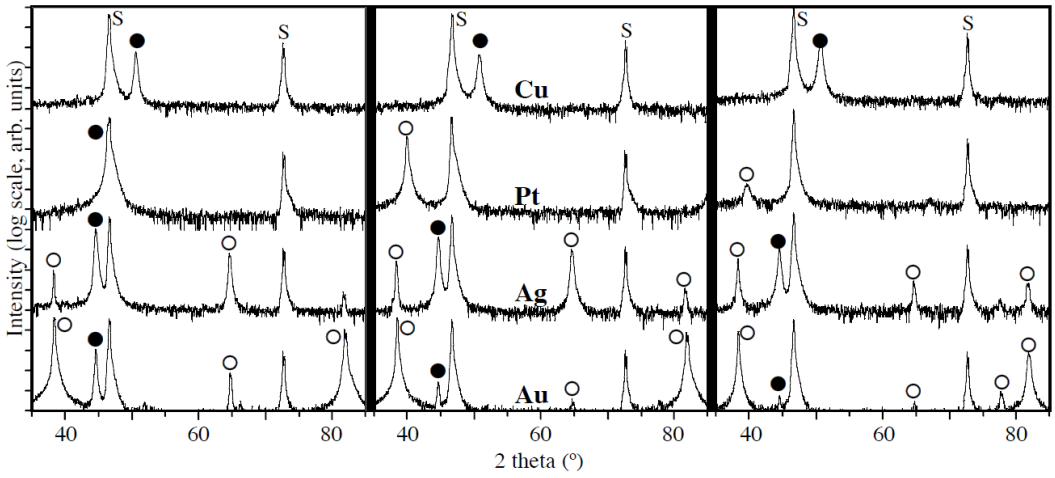

Figure 2.7: XRD pattern of different FCC metals deposited on $SrTiO_3(001)$ at different temperatures as presented in the work of Francis and Salvador [16]. The graphs are arranged such that the deposition temperature decreases for each metal reading from left to right. The metal are arranged top-to-bottom in order of decreasing oxygen affinity. The peaks marked with "S" are the substrate (001)-type peaks, the same for all the metals. The peaks marked with a filled circle are the metal (001)-type peaks, while the ones marked with an empty circle derive from other (hkl) planes.

For the particular case of the Au, the crystallographic properties of the system Au-$SrTiO_3(001)$ are not widely documented in literature. The work of Francis and Salvador [16] shows how (see Figure 2.7), among the FCC metals considered, Au is the one with the strongest preference to grow along the {111} direction over a wide temperature range (the {111} peaks are the ones highlighted by the open circles around $2\theta = 40°$). The Au(002) and Au(022) peaks are also present and on the whole the Au overlayer is polycrystalline. This experimental evidence is in perfect agreement with the high surface energy anisotropy end the low oxygen affinity of Au.

In the same work, the crystallographic in-plane orientation for the Au(002) oriented grains was found to be consistent with **OR I** mentioned before. However, this epitaxial relation seems to occur not as strictly as for the other metals investigated: other additional features appear in the corresponding diffraction pattern. Results consistent with **OR V** have been found by Silly and Castell [46], who have observed the following epitaxial relations for Au grown on a $SrTiO_3(001)$ - (2 x 1) substrate:

$$\begin{aligned} &(001)_{SrTiO_3} \,||\, (111)_{Au} \;,\; [110]_{SrTiO_3} \,||\, [110]_{Au} \\ &(001)_{SrTiO_3} \,||\, (111)_{Au} \;,\; [100]_{SrTiO_3} \,||\, [110]_{Au} \end{aligned} \tag{2.17}$$

With respect to the film morphology, Au tend to grow in 3D islands (as predicted by equation (2.14) and generally found for transition metal on ceramic substrates): due to the fast surface diffusion coefficient, the size of these islands is much bigger than for Pt and Cu and it is comparable to Ag ones [16].

2.3 Texture in polycrystalline materials and two-dimensional X-ray diffraction

2.3.1 Types of crystalline samples

The concepts and the experimental techniques presented in Section 2.1 constitute a valuable instrument for the study of a wide class of materials. The main feature which associates all of them is the presence of a certain degree of order: the length scale over which this order is present can be used as a first classification parameter. According to this criterion, three broad classes of X-ray diffraction samples can be distinguished. They are, namely (in decreasing degree of order): single crystals, polycrystalline textured samples and powder samples. They are schematically shown, along with the corresponding aspect of their typical diffraction pattern, in Figure 2.8.

Single crystals samples cover a very significant role, since they are the obvious manifestation of the concepts of order and periodicity which X-ray crystallography is based on. It is common knowledge that this kind of samples shows a periodic structure, that is to say the crystal lattice, which extends over macroscopic wide distances, infinite in the case of a theoretical perfect single crystal. In reality, single crystal samples are far from being perfect: on the contrary, they usually show a various number of defects (i.e. vacancies, dislocations, mosaic domains...) which limit the actual periodic structure to a region of finite size. The diffraction pattern produced by single crystal samples is characterized by the presence of bright and sharp regions (spots) of scattered light, one for each point of the reciprocal lattice. On the other extreme, there are the so called powder samples. They are formed by a large number of crystalline grains, also called crystallites: each of these is much smaller than the volume probed by the incident beam, but it is still large enough to show a regular crystal structure over distances much larger than the atomic scale. The grains possess a random orientation in space and the whole powder sample acts as an ensemble of small single crystals

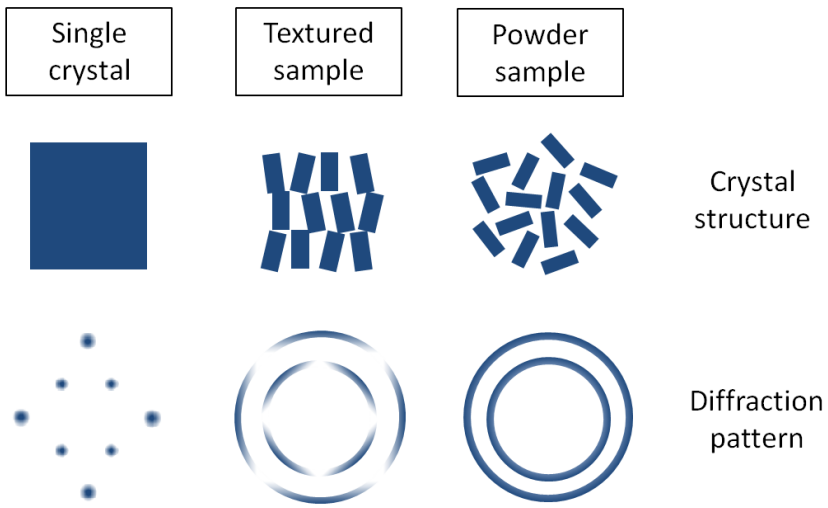

Figure 2.8: Schematic of the different types of crystalline samples and their corresponding diffraction pattern.

each of which scatters light in a different direction. The result is the formation of cones of diffracted radiation, each characterized by a fixed apex angle, equal to twice the scattering angle 2θ. On a flat detector positioned along the direct beam (with the detecting surface perpendicular to it) they give rise to the well known Debye powder rings. For a true powder sample with randomly oriented grains, the diffracted intensity along each ring is constant.

In addition, there is another class of materials with intermediate properties between those of a proper powder sample and those of a single crystal one. This class comprehends the so called textured polycrystalline samples. As for the powder samples they are made up by crystalline grains macroscopic on the atomic length scale. However, in this case, they are not randomly oriented: they exhibit instead an anisotropic orientation distribution, which is referred to as a preferred orientation or a *texture*. This happens when certain families of crystallographic planes are forced (for instance by the fabrication process) or find energetically favorable to "prefer" particular directions inside the sample. As a result, the diffraction rings produced by the crystallites of a textured sample display an intensity that is a function of the angular position along the ring. In some way textured materials represents the most general class of XRD samples: indeed both powder samples and single crystals may be regarded as special cases of a textured sample. The former can be considered as textured polycrystalline materials with a very weak texture (informally speaking, whose texture tends to zero); the latter are textured samples where the preferred orientation is so strong that each set of crystallographic planes presents only one possible orientation. Texture is present in most of engineered materials (such as metal wire or polymer fiber) and can have a great impact in the material properties. In the follow-up of this chapter the mathematical framework necessary for undertaking a full texture analysis will be presented.

2.3.2 Two dimensional X-ray diffraction: mathematical framework

The expression *Two dimensional X-ray diffraction* (XRD^2) [25] refers to X-ray diffraction experiments performed using an area (2D) detector. In the case of a conventional point (0D) detector, the collected data are usually presented as one-dimensional plots, displaying the diffracted intensity as a function of one of the goniometer angles. On the other hand, in the case of an area detector, the collected data consist of a two dimensional image frame, displaying the diffracted intensity as a function of the position on the detector surface. The main advantage of an area detector is the possibility to collect the diffracted light over a wide region in a single data acquisition (a single frame). Nowadays, in the area of single crystal diffraction, this advantage of area detectors becomes necessary to solve the structure of complex crystals (e.g. protein crystals). Nevertheless, area detectors are predominantly used in the field of polycrystalline samples studies, where they turn out to be necessary to collect multiple diffraction rings at the same time. Significant advantages are present when the analysis of the grains preferred orientation in a textured sample has to be accomplished: although it would be possible with a conventional point detector too, the usage of an area detector results indeed in a much lower acquisition time. Given the 2D diffraction data, the aim of a so called *texture analysis* is to determine which are the preferred orientations of the sample grains and display them by means of polar plots known as *pole figures*. In the remainder of the chapter the mathematical framework necessary to display the preferred orientations in a pole figure will be outlined. The conventions chosen are in agreement with the approach presented by He [25].

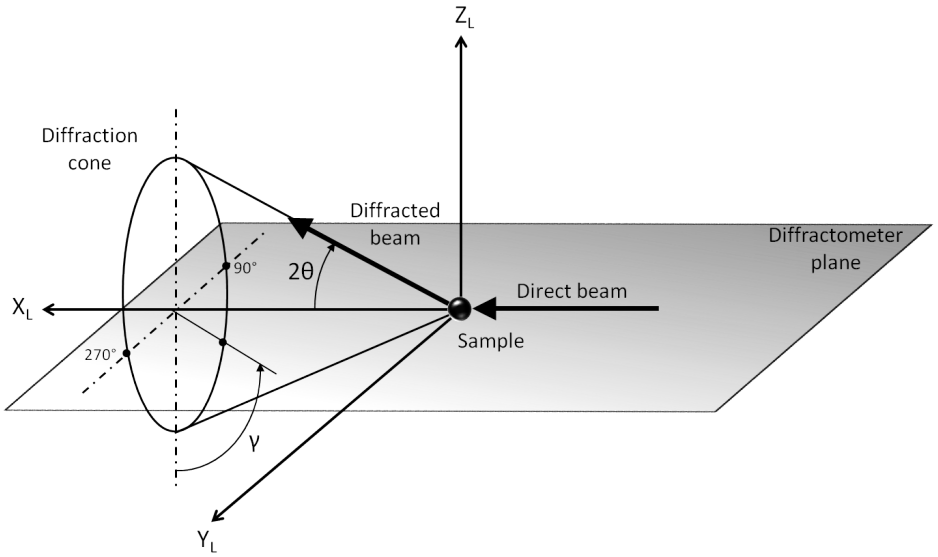

Figure 2.9: Experimental diffraction geometry, with the diffraction cone represented in the laboratory coordinate system.

The experimental scattering geometry can generally be described as shown in Figure 2.9, where the laboratory coordinate system $X_L Y_L Z_L$ is depicted. It is defined such that the direct beam incident on the sample propagates along the X_L axis. The X_L and Y_L axes define the so called *diffractometer plane*: the Z_L lies in the normal direction and points

upward. Considering these axes definitions, the rotation axis of a cone of diffracted light (referred to as the *diffraction cone*) coincides with X_L. The apex angle of the cone is given by the scattering angle 2θ defined by the Bragg equation: in particular, it is equal to twice the value of 2θ for forward reflection ($2\theta \leq 90°$) and twice the value of $180° - 2\theta$ for backward reflection ($2\theta \geq 90°$). The azimuthal position on the diffraction ring is given by the γ angle. The zero of γ corresponds to a beam diffracted in the vertical $X_L Z_L$ plane and pointing downward. For a diffracted beam lying on the diffractometer plane the possible values for γ are 90° or 270°. The direction of a diffracted beam is thus univocally determined by the pair of values $(2\theta, \gamma)$, which are referred to as the *diffraction space*: 2θ takes values from 0° to 180°, while γ takes values from 0° to 360° for a complete diffraction ring. These pair of values is fixed in the laboratory coordinate system, which is independent on the sample rotations and the position of the detector. The diffraction vector **H** is defined by the following

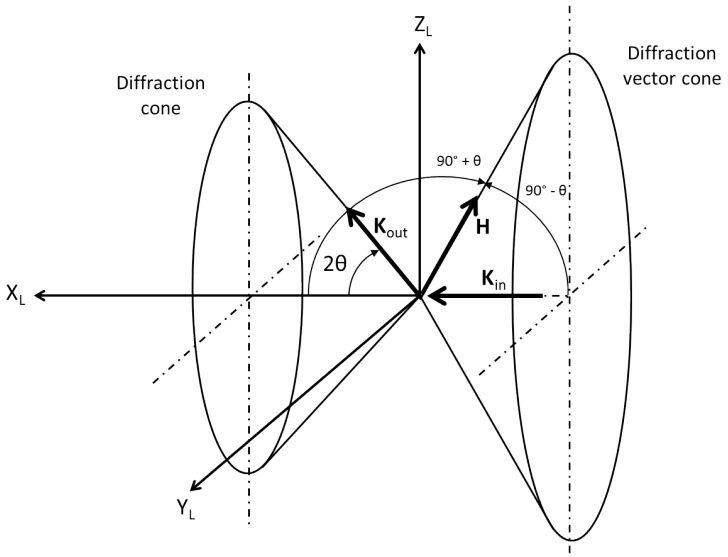

Figure 2.10: Schematic of the incident and diffracted wave vectors and of the corresponding diffraction vector cone.

$$\mathbf{K}_{out} - \mathbf{K}_{in} = \mathbf{H} \tag{2.18}$$

where $\mathbf{K}_{out}$ and $\mathbf{K}_{in}$ are the diffracted and incident beam wave vector respectively. The trace of all the diffraction vectors associated with a diffraction cone form the so called *diffraction vector cone*, as depicted in Figure 2.10. It's worth pointing out that, according to the definition (2.18), **H** does not necessarily satisfy the condition (2.7) for diffraction to occur. For each pixel of an area detector it is possible to calculate the corresponding diffraction vector even if the diffracted beam measured by the pixel does not originate from Bragg scattering. **H** has to be regarded as the vector whose direction bisects the incident and diffracted beam directions and whose modulus is equal to the momentum exchanged in the scattering process. In the particular case in which Bragg condition is satisfied, the diffraction vector will be equal to one of the reciprocal lattice vectors of the diffracting crystal. The incident and diffracted beam wave vectors can be expressed in term of the unit vectors $\mathbf{s}_{in}$

and $\mathbf{s}_{out}$, such that $\mathbf{K}_{in} = (2\pi/\lambda)\mathbf{s}_{in}$ and $\mathbf{K}_{out} = (2\pi/\lambda)\mathbf{s}_{out}$. In the laboratory coordinate system they are given by

$$\mathbf{s}_{in} = \begin{pmatrix} 1 \\ 0 \\ 0 \end{pmatrix} \quad , \quad \mathbf{s}_{out} = \begin{pmatrix} \cos 2\theta \\ -\sin 2\theta \sin\gamma \\ -\sin 2\theta \cos\gamma \end{pmatrix} \tag{2.19}$$

As previously noticed, $\mathbf{s}_{in}$ lies entirely on the X_L axis. In the same way, it is possible to associate to the diffraction vector $\mathbf{H}$ the corresponding unit vector $\mathbf{h}_L$ in the laboratory coordinate system, which identifies its direction :

$$\mathbf{h}_L = \frac{\mathbf{H}}{|\mathbf{H}|} = \begin{pmatrix} -\sin\theta \\ -\cos\theta \sin\gamma \\ -\cos\theta \cos\gamma \end{pmatrix} \tag{2.20}$$

Having outlined the scattering geometry and the corresponding relevant vectors quantities, the following step consists in describing the relation between each pixel of an area detector and the corresponding diffraction unit vector. This relation depends upon the shape of the surface of the particular area detector used. In the present work, only the case of a flat detector will be taken into account: a description valid for detectors with curved surfaces can be found in [25]. The position of a flat detector in the laboratory coordinate system is

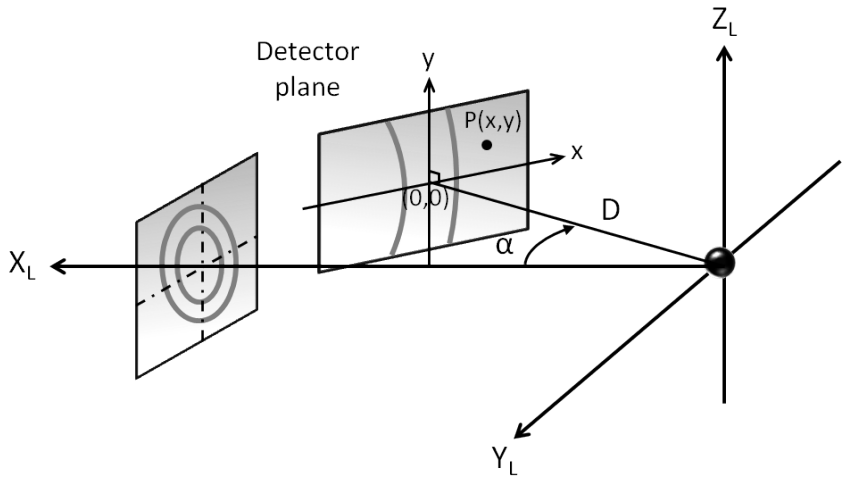

Figure 2.11: Schematic of the flat detector geometry in the laboratory coordinate system: the cases $\alpha = 0$ and $\alpha < 0$ are displayed.

described by specifying the sample to detector distance D along the direction normal to the flat detector surface and the detector swing angle α, as shown in Figure 2.11. The latter is defined as a right-hand rotation around the Z_L axis and the zero point corresponds to having the flat detector surface perpendicular to the incident beam. The pair of values (α, D) defines the so called *detector space*. For the case of the flat detector under discussion, the detection surface can be mathematically treated as a plane: the intersection between this plane and a diffraction cone gives rise to a conic section. Depending on the values of the detector swing

angle α and the apex angle of the diffraction cone 4θ, the resulting conic section can be an arc of ellipse ($2\theta > \alpha$), parabola ($2\theta = \alpha$) or hyperbola ($2\theta < \alpha$). In the particular case $\alpha = 0$ the resulting conic section is a circle: this is the case of a traditional powder diffraction experiment, where the well known Debye rings are obtained on the detector. One fundamental step in the data analysis of a XRD^2 experiment consists in relating each pixel of the detector to the corresponding diffraction unit vector $\mathbf{h}_L$, given the detector position (α, D). In order to accomplish this task, a 2D coordinate system is defined in the plane of the flat detector surface. The origin of this coordinate system is known as *Point of Normal Incidence* (*PONI*): it is defined as the intersection between the detector plane and the perpendicular distance to the laboratory system origin. In this way, the position of a generic pixel is described by the pair of values (x, y) which are related to the diffraction space coordinates $(2\theta, \gamma)$ by the following

$$2\theta = \arccos \frac{x \sin\alpha + D\cos\alpha}{\sqrt{D^2 + x^2 + y^2}} \qquad (0 < 2\theta < \pi) \tag{2.21}$$

$$\gamma = \frac{x\sin\alpha - D\cos\alpha}{|x\sin\alpha - D\cos\alpha|} \arccos \frac{-y}{\sqrt{y^2 + (x\sin\alpha - D\cos\alpha)^2}} \qquad (-\pi < \gamma < \pi) \tag{2.22}$$

Inserting the 2θ and γ values obtained through the (2.21) and (2.22) in the (2.20), the diffraction unit vector in the laboratory coordinate system related to the (x, y) pixel is finally obtained. For further information, the inverse functions of equations (2.21) and (2.22) are reported hearafter:

$$x = \frac{\cos\alpha \tan 2\theta \sin\gamma + \sin\alpha}{\cos\alpha - \sin\alpha \tan 2\theta \sin\gamma} \qquad (-\pi \leq \alpha \leq \pi,\ 0 \leq 2\theta < \pi) \tag{2.23}$$

$$y = -(x\sin\alpha + D\cos\alpha)\tan 2\theta \cos(\gamma) \qquad (-\pi \leq \alpha \leq \pi,\ 0 \leq 2\theta < \pi) \tag{2.24}$$

They allow to calculate the (x, y) pixel position where the diffracted beam of coordinates $(2\theta, \gamma)$ is incident.

Up to this point, the position of the sample in the laboratory coordinate system has never been considered. In a diffraction experiment the sample is generally mounted on a goniometer, made up by a set of rotational (as well as translational) stages driven by dedicated motors, which allows to modify the sample orientation: in this way the diffraction condition for a certain family of lattice plane can be fulfilled. The center of all the goniometer rotations coincides with the origin of the laboratory coordinate system: the direct beam will then be incident on the same point on the sample, regardless the position of the rotational stages. In the study of textured materials, the ultimate aim is to express the preferred crystal orientation of one or more families of lattice planes (whose orientation in lab coordinates is specified by $\mathbf{h}_L$) in terms of a coordinate system attached to the sample. This coordinate system thus rotates along with the sample and its position in the laboratory system depends on the values of the angles describing the rotations. In order to describe the sample rotations a new coordinate system $X_G Y_G Z_G$, referred to as the *goniometer coordinate system*, is introduced. Its relative orientation with respect to the laboratory one for all the sample rotations set to zero is displayed in Figure 2.12a. As the name suggests, the goniometer coordinate system follows the rotations of the goniometer stages. Considering an Eulerian geometry, a generic

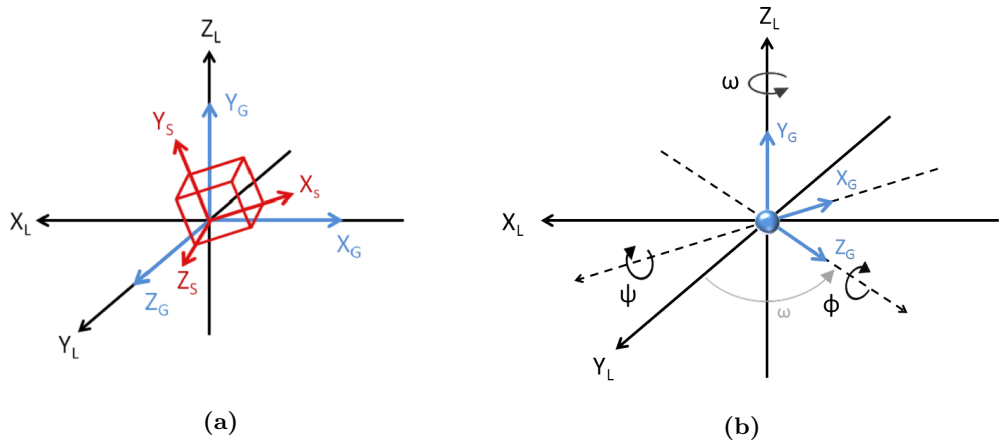

Figure 2.12: Goniometer and sample coordinate systems. (a) Goniometer (blue) and sample (red) coordinate system with all sample rotations set to zero. The latter does not coincide with the former as a result of the sample mounting. (b) Schematic of the sample rotations, namely, in the correct order, ω, ϕ and ψ. In the picture the ϕ and ψ angle are shown in their zero position: only the effect of the ω rotation is displayed. As shown, the goniometer coordinate system $X_G Y_G Z_G$ follows the sample rotations.

position of this system with respect to the lab one can be accounted for by three subsequent rotations around as many different axes. These are, in the order in which the rotations take place, ω, ϕ and ψ. In a traditional four-circle goniometer, a fourth rotation (usually referred to as 2θ) for the point detector is also present. The set of three values (ω, ϕ, ψ) (in the general case combined with a set of three values relative to the sample translations) is referred to as the *sample space*. As depicted in Figure 2.12b, ω is defined as a right-hand rotation around an axis coincident with Z_L. The ϕ axis depends on the value of ω and it coincides with Y_L for $\omega = 0$. Finally, the ψ axis depends on both the value of ω and ϕ: for $\omega = 0$ and $\phi = 0$, it coincides with X_L. The ϕ and ψ angle are here defined (see Figure 2.12b) as left-hand rotations around the corresponding axes. This convention is simply dictated by a matter of convenience: it is indeed consistent with the rotations physically present in the experimental setup which will be introduced in Section 3.2. For the same reason, the order of the rotations is different from the one proposed by He [25]. Adopting the aforementioned conventions, the diffraction unit vector in the goniometer coordinate system $\mathbf{h}_G$ is related to $\mathbf{h}_L$ through the following

$$\mathbf{h}_G = \mathbf{\Psi}\,\mathbf{\Phi}\,\mathbf{\Omega}\,\mathcal{A}\,\mathbf{h}_L \tag{2.25}$$

where $\mathbf{\Omega}$, $\mathbf{\Phi}$ and $\mathbf{\Psi}$ are the three-dimensional rotation matrices associated with the three goniometer rotations:

$$\mathbf{\Omega} = \begin{pmatrix} \cos\omega & 0 & -\sin\omega \\ 0 & 1 & 0 \\ \sin\omega & 0 & \cos\omega \end{pmatrix} \tag{2.26}$$

$$\mathbf{\Phi} = \begin{pmatrix} \cos\phi & -\sin\phi & 0 \\ \sin\phi & \cos\phi & 0 \\ 0 & 0 & 1 \end{pmatrix} \tag{2.27}$$

$$\mathbf{\Psi} = \begin{pmatrix} 1 & 0 & 0 \\ 0 & \cos\psi & -\sin\psi \\ 0 & \sin\psi & \cos\psi \end{pmatrix} \tag{2.28}$$

With all the angles set to zero the product of these three rotation matrices yields to the identity matrix $\mathbf{I}$:

$$\mathbf{\Psi}(\psi = \mathbf{0})\, \mathbf{\Phi}(\phi = \mathbf{0})\, \mathbf{\Omega}(\omega = \mathbf{0}) = \mathbf{I} = \begin{pmatrix} 1 & 0 & 0 \\ 0 & 1 & 0 \\ 0 & 0 & 1 \end{pmatrix} \tag{2.29}$$

However, within the adopted conventions, the goniometer coordinate system does not coincide with the laboratory one with all the sample rotation set to zero (see Figure 2.12a). This explains the presence, in equation 2.25, of the additional matrix

$$\mathcal{A} = \begin{pmatrix} -1 & 0 & 0 \\ 0 & 0 & 1 \\ 0 & 1 & 0 \end{pmatrix}$$

which describes a rotation of 180° about Z_L followed by a rotation of −90° about X_L.

Finally, the so called *sample coordinate system* $X_S Y_S Z_S$ is attached to the sample and it is defined such that its axes lie along significant directions of the sample itself. For instance, in the case where the texture properties of the sample are expected to be related to its elongated shape (e.g. in the case of a metallic rod), it is reasonable to make one of the axis to lie along the elongated direction. For the samples of interest for this work (described in Section 1.2) the obvious choice is to align the sample axes along the three main cubic axes of the monocrystalline STO substrate, as shown in Figure 2.12a. In general the sample coordinate system does not coincide with the goniometer one: indeed the sample can be arbitrarily mounted on the goniometer rotational stages. Even if one attempts to make them coincide, there will always be a shift between the two due the finite precision of the sample mounting. The sample and the goniometer coordinate system are related through the $\mathbf{U}$ matrix, such that

$$\mathbf{h}_S = \mathbf{U}\, \mathbf{h}_G \tag{2.30}$$

where $\mathbf{h}_S$ is the diffraction unit vector in the sample coordinate system. If the sample exhibits long range crystalline order, it may be convenient to express $\mathbf{h}_S$ in terms of the reciprocal lattice base vectors $\mathbf{a}^*, \mathbf{b}^*, \mathbf{c}^*$ (equation (2.8)). An additional matrix (commonly called $\mathbf{B}$), depending on the particular crystal structure considered, would then become necessary:

$$\mathbf{h}_{\mathbf{a}^*,\mathbf{b}^*,\mathbf{c}^*} = \begin{pmatrix} h \\ k \\ l \end{pmatrix} = \mathbf{B}\, \mathbf{h}_S \tag{2.31}$$

where $\mathbf{h}_{\mathbf{a}^*,\mathbf{b}^*,\mathbf{c}^*}$ is the diffraction unit vector in terms of the reciprocal lattice basis. For the case of a cubic crystal of interest for the present work, the $\mathbf{B}$ matrix reduces to the

identity $\mathbf{I}$: exept that for the present general discussion, it will be ignored in the rest of the present work and no difference will be made between $\mathbf{h}_S$ and the corresponding vector in the (hkl) notation. To sum up, the diffraction unit vector in terms of the reciprocal lattice basis $\mathbf{h}_{\mathbf{a}^*,\mathbf{b}^*,\mathbf{c}^*}$ can be calculated from the same vector in the laboratory coordinate system $\mathbf{h}_L$ through the following

$$\mathbf{h}_{\mathbf{a}^*,\mathbf{b}^*,\mathbf{c}^*} = \mathbf{B}\,\mathbf{U}\,\mathbf{\Psi}\,\mathbf{\Phi}\,\mathbf{\Omega}\,\mathcal{A}\,\mathbf{h}_L \tag{2.32}$$

If necessary, the previous relation can of course be reversed, thus allowing $\mathbf{h}_L$ to be expressed as a function of $\mathbf{h}_{\mathbf{a}^*,\mathbf{b}^*,\mathbf{c}^*}$:

$$\mathbf{h}_L = \widetilde{\mathcal{A}}\,\widetilde{\mathbf{\Omega}}\,\widetilde{\mathbf{\Phi}}\,\widetilde{\mathbf{\Psi}}\,\widetilde{\mathbf{U}}\,\widetilde{\mathbf{B}}\,\mathbf{h}_S = \mathcal{A}^{-1}\,\mathbf{\Omega}^{-1}\,\mathbf{\Phi}^{-1}\,\mathbf{\Psi}^{-1}\,\mathbf{U}^{-1}\,\mathbf{B}^{-1}\,\mathbf{h}_{\mathbf{a}^*,\mathbf{b}^*,\mathbf{c}^*} \tag{2.33}$$

It is worth noticing that most of the literature regarding angle calculations for diffraction goniometers aim to find the reverse relation, which lead to determine $\mathbf{h}_L$ starting from $\mathbf{h}_{\mathbf{a}^*,\mathbf{b}^*,\mathbf{c}^*}$. The matrices involved are then usually defined with respect to equation (2.33): as a consequence, the matrices $\mathbf{U}$ and $\mathbf{B}$ are usually the inverse of the ones defined in the present work and they correspond to those here named $\widetilde{\mathbf{U}}$ and $\widetilde{\mathbf{B}}$ respectively. The same stands for the matrices associated with the sample rotations.

In summary, starting from the data collected with a flat area detector, the calculations just presented allows to express the orientation of a certain family of lattice planes, that is to say the corresponding unit diffraction vector, in a reference frame attached to the sample. Ignoring for the moment the sample mounting (which is a constant in a diffraction experiment) and considering $\mathbf{B} = \mathbf{I}$, the $\mathbf{h}_S$ vector thus derived is a function of both the pixel position, which defines the pair of values $(2\theta, \gamma)$ through the (2.21) and (2.22), and the sample rotations (ω, ϕ, ψ):

$$\mathbf{h}_S = \mathbf{h}_S(2\theta, \gamma, \omega, \phi, \psi) \tag{2.34}$$

The $\mathbf{h}_S$ vector is in turn univocally associated to a certain value of diffracted intensity I:

$$I = I(\mathbf{h}_S) = I(2\theta, \gamma, \omega, \phi, \psi) \tag{2.35}$$

where the dependance of the intensity on the angle $2\theta, \gamma, \omega, \phi$ and ψ is due to the corresponding dependance of the $\mathbf{h}_S$ vector. For a given family of lattice planes (hkl), the value of 2θ is fixed by the Bragg law and equal to $2\theta_{hkl}$. The corresponding unit diffraction vector, namely

$$\mathbf{h}_S^{hkl} = \mathbf{h}_S(2\theta = 2\theta_{hkl}) \tag{2.36}$$

is thus only a function of γ, ω, ϕ and ψ. Integrating the diffracted intensity in the 2θ variable over an interval large enough to include the value of interest leads to the integrated intensity

$$I_{hkl} = I_{hkl}(\mathbf{h}_S^{hkl}) = I_{hkl}(\gamma, \omega, \phi, \psi) = \int_{2\theta_{hkl}-\Delta_{2\theta}}^{2\theta_{hkl}+\Delta_{2\theta}} I(2\theta, \gamma, \omega, \phi, \psi)\, d\,2\theta \tag{2.37}$$

As mentioned in Section 2.3.1, in a powder sample, where all the grains are randomly oriented, each family of lattice planes is isotropically distributed in space: the corresponding integrated

intensity is actually a constant. For the more general case of a material displaying texture properties, the diffracted intensity will be greater along the grains preferred directions. The resulting integrated intensity function I_{hkl} for each of the lattice planes of interest can be determined by acquiring multiple detector frames for different values of the sample rotations (more information about the data collection strategy can be found in reference [25]). Once the data have been collected, the following step consists in properly represent the function I_{hkl} on a bi-dimensional plot, as describe hereafter.

The most common way to present diffraction data of textured materials is the one based on the method of stereographic projections. A stereographic projection is one of the possible tools which allow to display the points of a spherical surface on a planar image. Its geometric construction is illustrated in Figure 2.13a in reference to the case under study. Considering a sphere of unit radius centered in the sample coordinate system, the $\mathbf{h}_S$ vector tip identifies a point, called *pole*, on the spherical surface. The projection of the pole on the equatorial plane $X_S Y_S$ of the sphere is obtained by connecting the pole with the south pole **S** of the sphere. The point of intersection **P** between the segment thus obtained and the equatorial plane is the desired projection: it univocally identifies the pole on the planar surface represented by the equatorial plane. The resulting 2D plot can be considered in the same way as a normal plot in polar coordinates, where the position of the projection **P** is described by the pair of values (r, β), where r is the distance from the origin and β is the angle with respect to the positive direction of the X_S axis. They are given by the following pole mapping equations:

$$r = \tan\frac{\chi}{2} = \tan\frac{\frac{\pi}{2} - \arccos\sqrt{(h_S^x)^2 + (h_S^y)^2}}{2} \tag{2.38}$$

$$\beta = \begin{cases} \arccos\dfrac{h_S^x}{\sqrt{(h_S^x)^2 + (h_S^y)^2}} & h_S^y \geq 0 \\ -\arccos\dfrac{h_S^x}{\sqrt{(h_S^x)^2 + (h_S^y)^2}} & h_S^y < 0 \end{cases} \tag{2.39}$$

where $\chi = \frac{\pi}{2} - \arccos\sqrt{(h_S^x)^2 + (h_S^y)^2}$ is the angle between the north pole of the sphere and the tip of the $\mathbf{h}_S$ vector. Equations (2.38) and (2.39) can be used to express the intensity function (2.37) in terms of the stereographic projection coordinates r and β: $I_{hkl} = I_{hkl}(r, \beta)$. One of the most widespread methods used to represent such a function provides to assign a color at each intensity value and to display the intensity as a colormap within the polar plot of Figure 2.13b. The resulting plot is commonly known as *pole figure*. This method of data visualization will be widely use in Chapter 4, where further details about the data analysis will be provided as well.

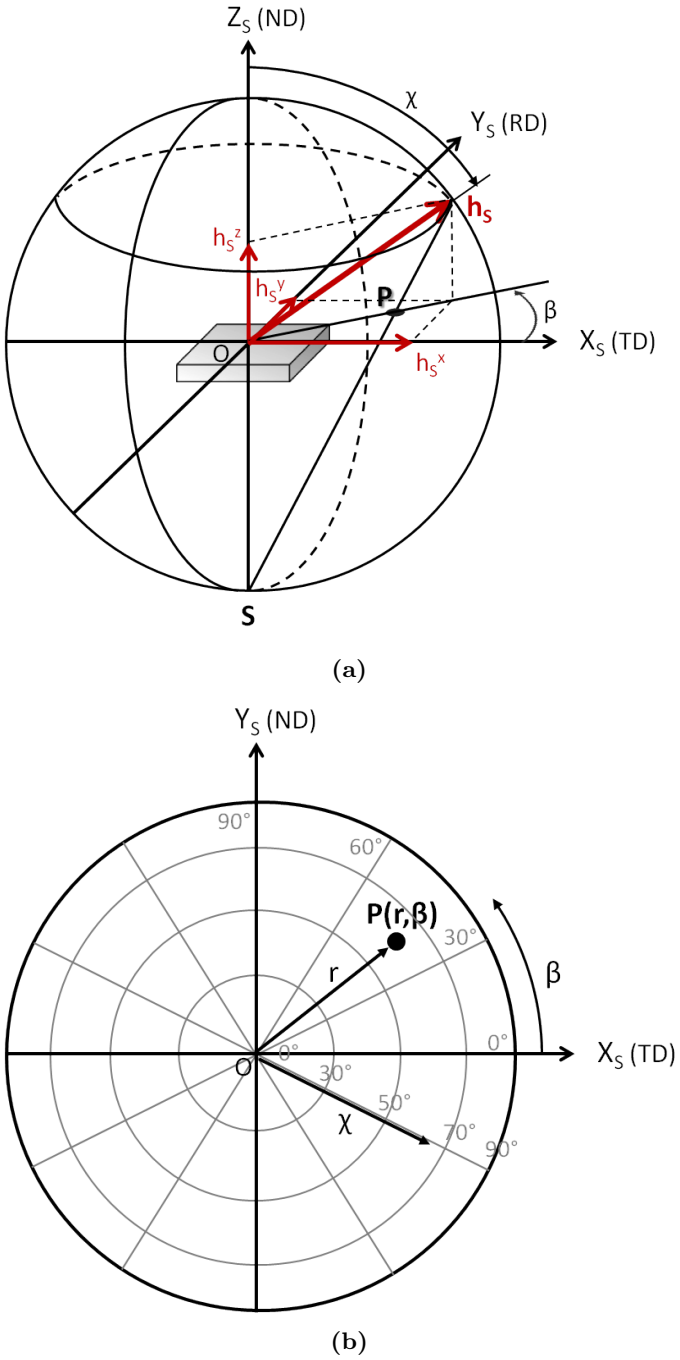

Figure 2.13: (a) Geometric construction underlying the definition of a stereographic projection, with a representation of the most relevant quantities. The traditional nomenclature of the axes used in this kind of representation is displayed: RD, TD and ND stands for rolling direction, transverse direction and normal direction respectively. (b) Stereographic projection obtained as diplayed in Figure 2.13a. As well as the radius r and the β angle, the projection of the χ angle values are represented.

Chapter 3

Experimental setup

In the present chapter, the experimental setup used to perform the measurements described in Chapters 4 and 5 is presented. In Section 3.1 a quick overview of the synchrotron beamline where the experiments took place is provided. The two most relevant components of the beamline instrumentation for the case under study, namely the CCD area detector setup and the diffractometer, are discussed more in details in Sections 3.2 and 3.3 respectively.

3.1 Overview of the beamline

The measurements presented in Chapters 4 and 5 were entirely performed in the beamline ID06 of the European Synchrotron Radiation Facility (ESRF), in Grenoble, France. Beamline ID06 was first operational in 2008 and it belongs to the ESRF Dynamics and Extreme Conditions group. Since its first year of operation, it has been mostly exploited as a techniques and instrumentation test beamline, serving as an internal support for the other ESRF beamlines. This task has been mainly concentrated in the Experimental Hutch 1 (EH1), which has been at the service of the group which is in charge of developing the X-ray optics for the beam conditioning. At the moment the experiments described in the present work were conducted, EH1 was involved in the overture of a long term upgrade program which is reshaping the hutch appearance. This upgrade program, still in progress, concerns the installation of a new setup for X-ray microscopy experiments: the aim will be to turn ID06 in a beamline available for potential external users. A smaller percentage of the beamtime is dedicated to diffraction experiments on different type of crystalline samples under extreme experimental conditions. This research activity, located in Experimental Hutch 2 (EH2) and available for external users, is concentrated in two main areas: investigation of polycrystalline samples at high temperature and high pressure (achieved through the Large Volume Press (LVP)), mainly with interest in the field of geology; study of single crystal magnetically and\or electrically ordered samples in pulsed magnetic (and\or electric) fields through traditional X-ray diffraction or Resonant Elastic X-ray Scattering (REXS). ID06 is a hard X-ray beamline: its undulators allow to cover a wide beam energy spectrum, ranging from a few keV to several tens of keV. As shown in Figure 3.1, it consists of two experimental

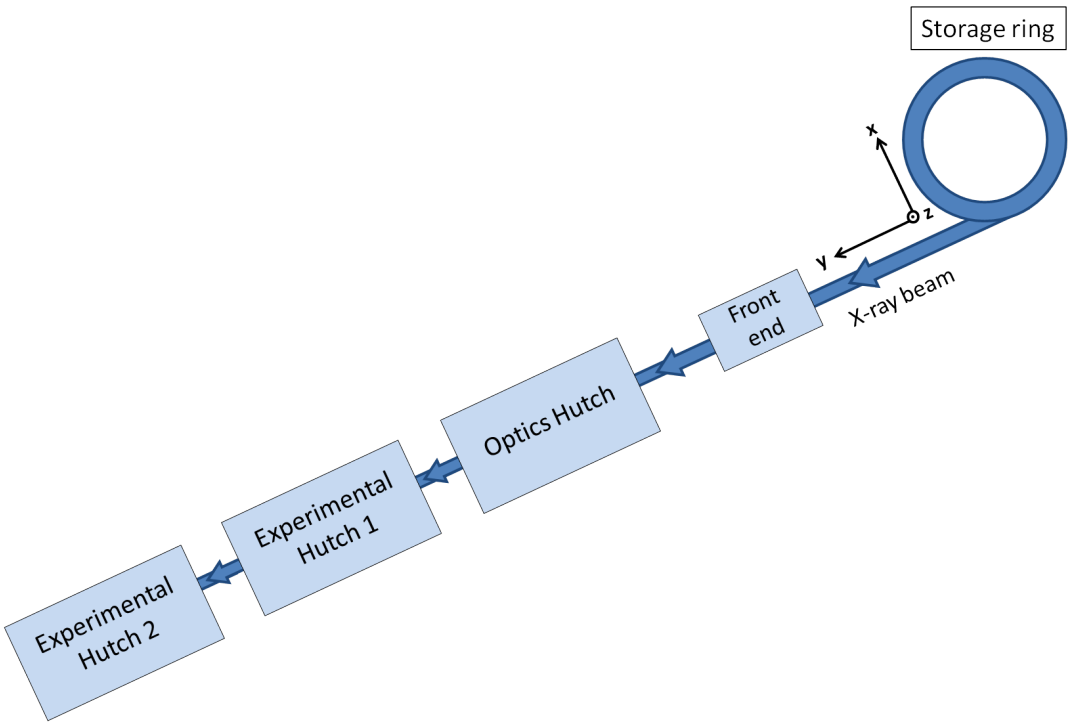

Figure 3.1: Schematic of the beamline ID06 of the European Synchrotron Radiation Facility (ESRF). The beamline coordinate system in use throughout all this chapter is also reported.

hutches, preceded by an optics hutch for the beam conditioning. Hereafter a brief description of the most important components of the optics and experimental hutches (summarized in Figure 3.2) will be provided: further details can be found in the ID06 wiki page [47] available on the ESRF website. For further information about the properties of synchrotron radiation and its potentialities in the field of solid state physics see Appendix A.

The main role of the optics hutch is to realize a set of preliminary operations of beam conditioning on the white beam exiting the beamline front end: these include attenuating and modifying the size of the beam, selecting a precise wavelength and focusing. Proceeding upstream to downstream, the first elements of the optics hutch are the high power attenuator, which aims to reduce the heat load on the monochromator, and the primary slits placed along the beam path. The monochromatization of the beam is the central role of the optics hutch. This task is accomplished through the Bragg reflection by a pair of silicon single crystals (optionally Si(111) or Si(311)), which allows to select the desired wavelength while keeping the beam along the horizontal (y axis) direction. The Si(111) monochromator guarantees a transmitted bandwidth of only 0.013% of the incident energy. In order to check the correct alignment of the beam, an intensity monitor is placed downstream of the monochromator, together with the secondary slits S2. Vertical or bidirectional focusing (as well as collimation) is achieved by the transfocator, which is made up by a series of parabolic (1D) or paraboloid (2D) compound refractive lenses. All the elements inside the optics hutch along the beam path are kept in a Ultra High Vacuum (UHV) environment by several ion pumps. This is done for mainly two reasons: preserving the cleanliness of the surfaces of the optical elements for the beam conditioning (e.g. the monochromator crystals) and avoiding the air absorption

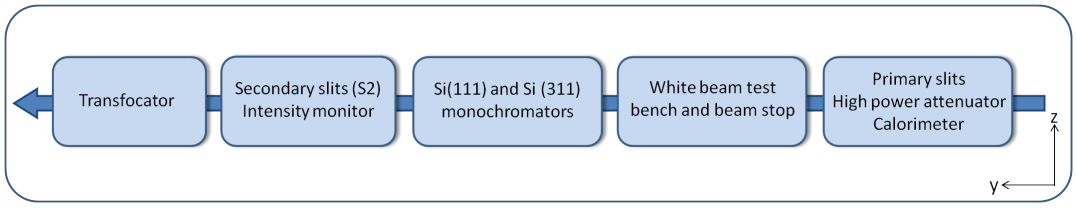

(a) Optics Hutch

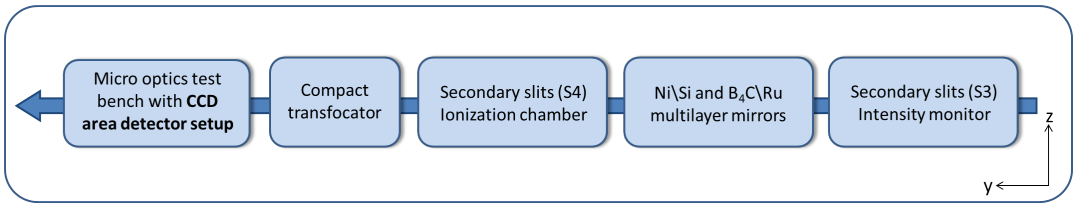

(b) Experimental Hutch 1

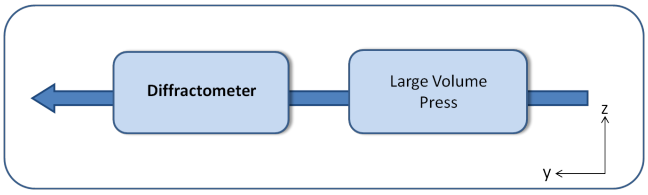

(c) Experimental Hutch 2

Figure 3.2: Main components of the three hutches of the beamline ID06.

losses, which otherwise would have a great impact on the intensity available on the sample (the optical path across the optics hutch is indeed about 15 m long). The vacuum also guarantees to thermally insulate the liquid nitrogen cooled crystals of the monochromator from the room temperature surroundings.

Inside EH1, the beam exiting the optics hutch first encounters an additional intensity monitor and the secondary slits S3, followed by a double mirror system. This is composed by a flat mirror for deflection of the beam in the horizontal plane, followed by a cylindrical mirror with dynamical bending in order to achieve focusing. The usage of two mirrors guarantees the possibility to focus the beam without altering (apart from an horizontal displacement) the propagation direction. The flat mirror can be moved to select one of four different stripes, each one of a different material and optimized for a different energy range. They are made by the following materials: Si (to be used at grazing incidence at the energy range 3÷5 keV); Ni (to be used at grazing incidence at the energy range 5÷8 keV); multilayers of B_4C\Ru with a period of 7 nm (energy range 8÷15 keV); multilayers of B_4C\Ru with a period of 2 nm (energy range 15÷20 keV). The double mirror system can be alternatively used to suppress the harmonic components of the wavelength transmitted by the monochromator: choosing the proper stripe for the wavelength of interest, the harmonics will experiment a much lower reflection and will be consequently attenuated (with a double mirror system an attenuation of 4-5 orders of magnitude of the second harmonic is easily achieved). Downstream to the mirrors, the secondary slits S4, an ionization chamber (used to monitor the beam intesity) and a compact trasfocator for the beam focusing are present. The central component of EH1 is the micro optics test bench, where different optics component can be installed. Regarding the experiments presented in this work, it has hosted the CCD area detector setup which will be described in the next section. The X-ray beam propagates in UHV maintained by an ion pump up to the compact transfocator (see Figure 3.2b). For experiments performed in EH2 a vacuum pipe can be mounted across the two hutches thus to remove most of the air along the beam path between the compact transfocator and the sample.

Finally, EH2 hosts the Large Volume Press for the high pressure studies mentioned at the beginning of the present section and the diffractometer for single crystal diffraction which will be presented more in detail in Section 3.3.

The data that will be presented in Chapters 4 and 5 were mainly acquired during two different experiments. The first one was performed using the CCD are detector setup in Experimental Hutch 1 and was meant to provide a first insight of the texture properties of the samples presented in Section 1.2. The second experiment exploited the diffractometer of Experimental Hutch 2 to examine in depth particular aspects emerged from the data acquired from the previous one. Both the area detector setup and the diffractometer are described more in detail in the following sections.

3.2 CCD area detector setup

The first experiment of the present work made use of a focused beam at an energy of 7 keV (selected using the Si(111) crystals of the monochromator), with harmonics rejection attained

through the $B_4C\backslash Ru$ multilayer mirror (period of 7 nm). The relative low energy chosen for the incident beam was justified by the necessity to limit as much as possible the penetration of the X-rays in the sample substrate. Indeed the experiment aimed to study the properties of the STO thin film and the embedded Au nanoparticles: probing the single crystal STO substrate would have had the only effect to produce intense beams of diffracted light on the detector, thus leading to a strong pixels saturation. The latter has a detrimental effect on the quality of the acquired CCD images, for it produces large bright regions which prevent weaker peaks in the surrounding area from being seen. This problem was not completely avoided, since the attenuation length of a 7 keV beam (considering for simplicity a sample composed entirely by STO) is anyway about 13 μm, much larger than the thin film thickness: further lowering the energy, would have implied intolerable air absorption losses. Already at 7 keV they are indeed quite strong, leading to an attenuation length of about 60 cm.

The setup is shown in Figure 3.3. The X-ray beam is scattered by the sample and the diffracted radiation is collected by the CCD detector, whose height and distance to the sample along the y axis of the beamline coordinate system could be adjusted. For the experiment under discussion they were chosen such that the corresponding sample to detector distance D (as defined in Section 2.3.2) was between 96 and 133 mm. The detector swing angle was maintained fixed at a value of about $-45°$. These values allowed the detector to be close enough to sample to limit the signal losses due to the absorption of the air. At the same time they permitted to cover the range of 2θ values between 27° and 92°. The sample-detector relative position corresponds to a *Bragg* (or reflection) *diffraction geometry*, where the incident and the diffracted beam are located on the same side of the sample. This reduces the optical path of the beam inside the sample, thus reducing the absorption losses and the volume of the substrate probed (preventing the appearance of the bright substrate peaks). It further implies that the diffraction vectors which is possible to probe are the ones enclosed in the hemisphere above the sample surface, that is to say such that the condition $h_S^z < 0$ holds (see Figure 2.13a and consider the relative orientation of the $X_L Y_L Z_L$ and $X_S Y_S Z_S$ coordinate systems). The detector used was a MarCCD detector, with 2048 x 2048 pixels of size 64.5 x 64.5 μm^2. The detector was cooled down at an operating temperature of 77 K. This resulted in a very low dark current: as reported by the manufacturer's specifications, even for a 1000 seconds exposure, the charge equivalent to 1 single photon of 12 keV is accumulated. As a consequence, it was not necessary to collect true dark current images with the same exposure time of the desired ones: a simple readout noise image (dark frame of zero exposure time) was sufficient.

The rotational (as well as translational) degrees of freedom of the sample mounting are shown in their zero position in Figure 3.4. The definitions of the various angles are consistent with the conventions used in Section 2.3.2. However, one additional rotation, here named η, is present. This rotation is located on top of all the others; the corresponding axis coincides with the ω one when all the other angles are equal to zero. Hence, in this particular case, the general relation (2.32) (and subsequently (2.33)) has to be modified as follows:

$$\mathbf{h}_S = \mathbf{B}\,\mathbf{U}\,\mathbf{\Sigma}\,\mathbf{\Psi}\,\mathbf{\Phi}\,\mathbf{\Omega}\,\mathcal{A}\,\mathbf{h}_L \tag{3.1}$$

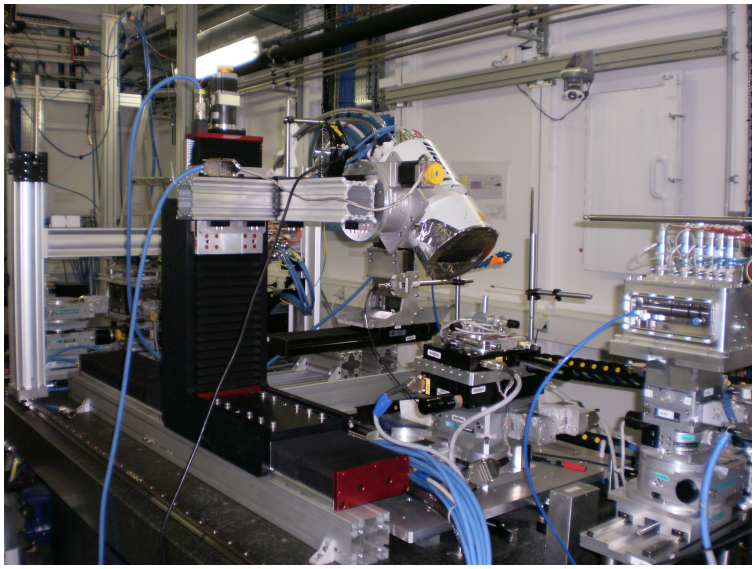

(a)

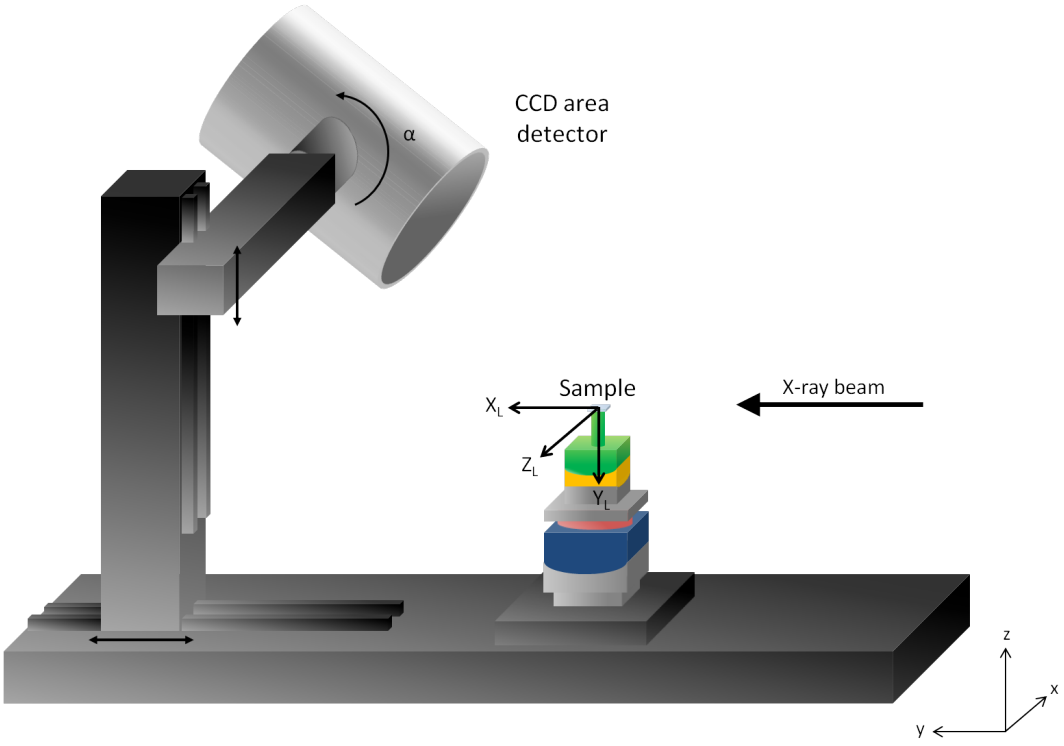

(b)

Figure 3.3: CCD area detector setup of EH1 used for the texture analysis experiment. (a) Photo of the experimental setup. (b) Schematic of the setup shown in the photo. The CCD detector (with its rotational and translational degrees of freedom) and the sample are shown. Both the sample laboratory reference frame introduced in Section 2.3.2 and the beamline coordinate system common to three hutches are displayed.

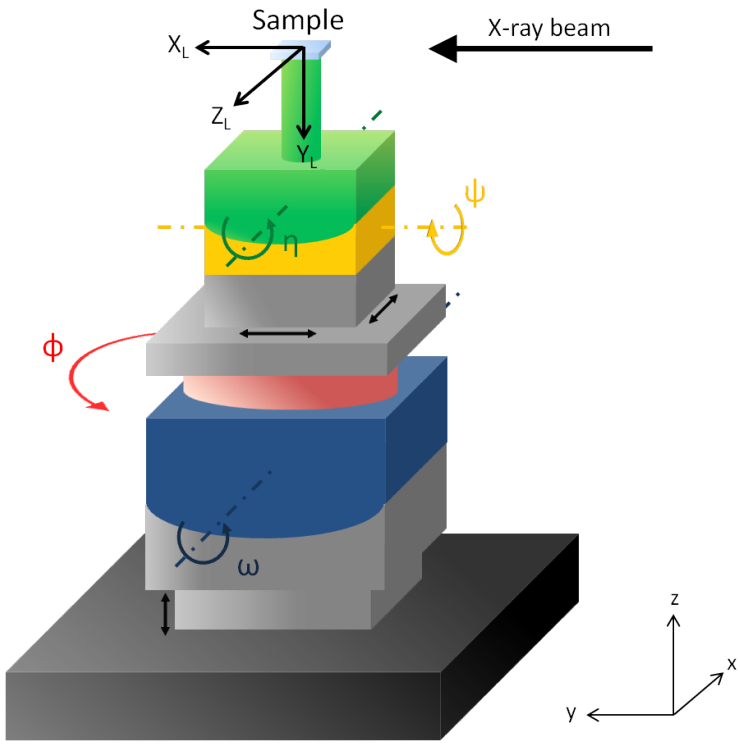

Figure 3.4: Detail of the sample mounting used in the setup shown in Figure 3.3b. The rotational and translational stages are highlighted, along with the sample laboratory reference frame introduced in Section 2.3.2. With respect to those discussed in Section 2.3.2, the additional sample rotation η is present. All the rotations are displayed in their corresponding zero position.

where

$$\mathbf{\Sigma} = \begin{pmatrix} \cos\eta & 0 & -\sin\eta \\ 0 & 1 & 0 \\ \sin\eta & 0 & \cos\eta \end{pmatrix} \tag{3.2}$$

The samples were fixed on the sample holder with the surface parallel to the horizontal plane, trying to manually align the main cubic axis of the substrate to the $X_L Y_L Z_L$ coordinate system. If this was the case, the **U** matrix would be equal to the identity **I** thus simplifying the analysis of the diffraction data. Of course a manual alignment cannot guarantee the previous condition to be rigorously fulfilled: hence the **U** matrix will be in general slightly different from the identity. Of the three angular offsets necessary to express **U**, only two can be measured and consequently compensated in this setup: this can be accomplished by adjusting η and ψ thus to make the sample surface lie on the horizontal plane. Unfortunately, the third offset, relative to the in-plane orientation of the sample, is left undetermined. This inconvenient, whose repercussions will be discussed in Chapter 5, can be easily overcome by exploiting a single crystal diffractometer, as the one presented in the following section.

3.3 Diffractometer

For the second experiment, most of the measurements were performed with a beam energy of 11 keV, while a smaller number made use of a 15 keV one. In both cases, harmonics rejection was achieved by slightly detune the Si(111) monochromator from the perfect Bragg condition. In order to use experimental parameters similar to the ones of the first experiment, a tentative to use a 7 keV beam was made. In spite of the presence of the vacuum pipe mentioned in Section 3.1, the air absorption losses turned out to be excessive and this value of energy was abandoned. Since the point detector mounted on the diffractometer allow to collect only one diffraction peak at a time, the presence of strong substrate peaks due the higher energy did not represent a significant limitation. On the contrary, a low incident intensity has a detrimental effect on the measurements of the Au peaks: the amount of diffracting material, especially for the samples with the lowest initial Au layer thickness, is small and the diffracted signal can be in general very weak. This problem will be pointed out again in the following chapters. Choosing the best value of the beam energy was actually one of the most puzzling aspect of the experiment, since it required to take into account several different factors:

- The air absorption. Given the great sample-to-source distance, it had a more critical role with respect to the first experiment: lowering the value of the energy would have implied a significant decrease in the intensity incident on the sample.
- The Bragg diffraction geometry. As will be shown heareafter, even in the case of the diffractometer, the experiment was performed in reflection geometry, with the diffracted beam emerging from the same side of the direct beam with respect to the sample. This restricts the (hkl) crystallographic planes which can be put in diffraction condition to the ones which satisfies the following

$$\theta_{hkl} - \theta_n = \omega > 0 \tag{3.3}$$

where θ_{hkl} is the Bragg angle of the (hkl) crystallographic planes, ω is the angle between the incident beam and the sample surface (positive for a beam incident from above the sample top surface) and θ_n is the angle between the normal to the sample surface and the reciprocal lattice vector $\mathbf{Q}$ satisfying equation 2.7. But θ_{hkl} is related to the wavelength of the incident beam by Bragg's law. For a given family (hkl) of lattice planes, it implies that, in order to observe the corresponding diffracted beam, a minimum value λ_{hkl} for the wavelength exists. This is given by

$$\lambda_{hkl} = 2d_{hkl} \sin \theta_n \tag{3.4}$$

where d_{hkl} is the (hkl) d-spacing. For smaller value of the wavelength, a switch to the so called *Laue* (or transmission) *diffraction geometry* occurs, which is not feasible with the sample mounting considered. Increasing the beam energy would then decrease the number of lattice planes that can be probed in the reflection geometry. A schematic of the Bragg diffraction geometry and all the angle involved in equation (3.3) is shown in Figure 3.5.

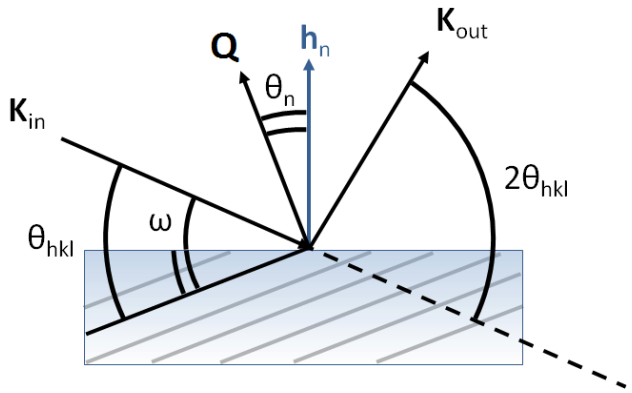

Figure 3.5: Schematic of the Bragg diffraction geometry. The angles involved in equation 3.3 are highlighted.

- The presence of atomic resonances. Another constraint in the choice of the beam energy was represented by the necessity to avoid resonances occuring in proximity of the atomic absorption edges. These resonances drastically modifies the atomic scattering factor, as introduced in Section 2.1: the depressions at 3.4, 11.9 and 13.7 keV that can be seen in Figure 2.3 for the case of the Au are due to the M_1, L_3 and L_2 absorption edges respectively. The beam energies in proximity of these values had thus to be discarded.

- The X-ray source. The energy of the primary beam is intrinsically related to the intensity by the characteristics of the X-ray source, that is to say the undulators which the X-ray photons generates from. In Figure 3.6 the number of photons generated per unit time (and normalized to a bandwidth of the 0.1% of the incident energy) are displayed as a function of the photon energy. The plot is related to the undulator exploited for the energy range E $>$ 10 keV: as can be clearly seen, the photons rate generally decreases as the energy increases.

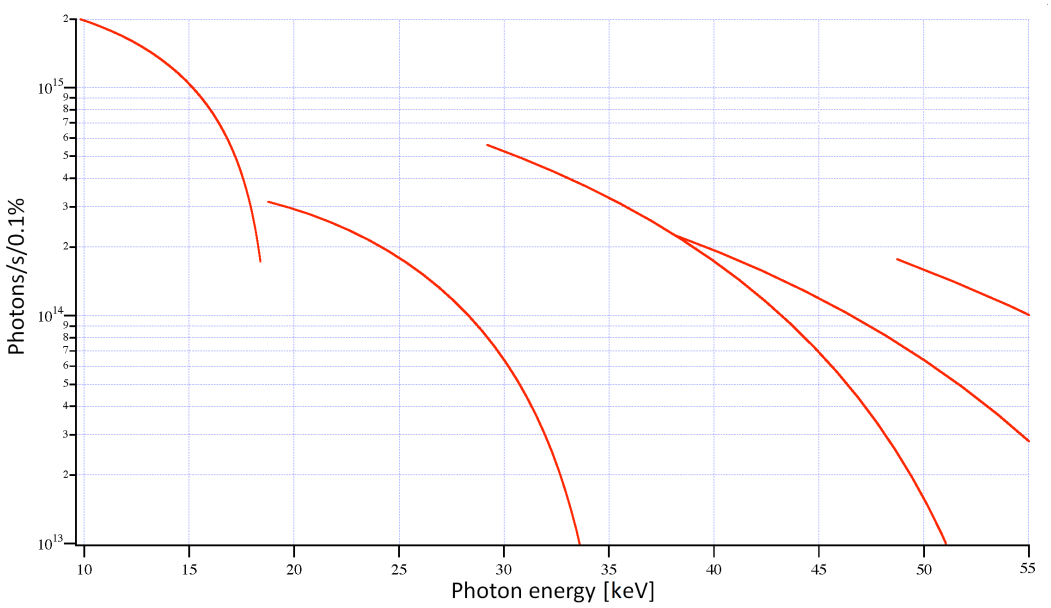

Figure 3.6: Photon rate as a function of the photon energy for the 18 mm period permanent magnet undulator of beamline ID06 [47]. The calculated photon rate is related to a bandwidth of 0.1% of the incident energy.

The experimental setup used for this second experiment consists of a single crystal diffractometer, with two detectors and one sample rotation (displayed in their zero position in Figure 3.7b). Additional translational stages to adjust the position of the sample with respect to the direct beam are not shown. The conventions chosen for the angles name are not related to the ones presented in Section 2.3.2 and used in Section 3.2. The only analogy is represented by the ω angle, which is also in this case the angle between the incident beam and the sample surface (as shown in Figure 3.5). The δ angle is defined around the same axis as the ω angle, while the γ axis lies along the x axis of the beamline coordinate system. The reader is encouraged to notice that the γ angle here considered is in no way related to the one used in Section 2.3.2: in the remainder of the present work will be clear from the context which one of the two angles the symbol refers to.Two different types of point (0D) detector were used: a traditional diode and an Avalanche Photo Diode (APD), the latter more suitable in cases of low signal. The massive sample basement of the diffractometer is conceived to host the heavy magnets necessary for pulsed magnetic field measurements. For the case under study, the sample was fixed on the same cylindrical sample holder used for the setup of Section 3.2, but with the sample surface lying this time on the vertical plane. The sample mounting was performed trying to approximately align the three main cubic axes of the sample substrate to the beamline coordinate system ones (for the sample ω rotation in its zero position). However, no further determination of the sample mounting offsets was here necessary. Given the incident energy and the lattice parameter of the diffracting crystals, the diffractometer control software can automatically calculate the **U** and **B** matrices from the motors values of two known substrate reflections (the so called primary and secondary reflection). Once these two reflections have been found, any other direction of the reciprocal

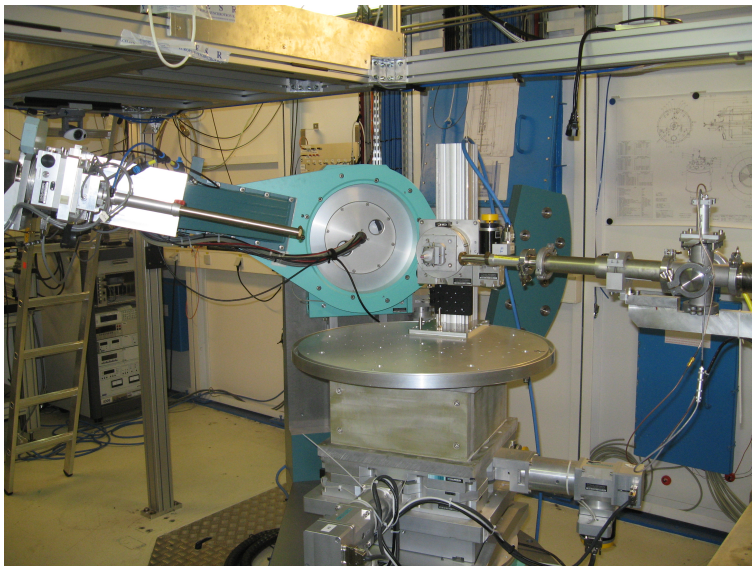

(a)

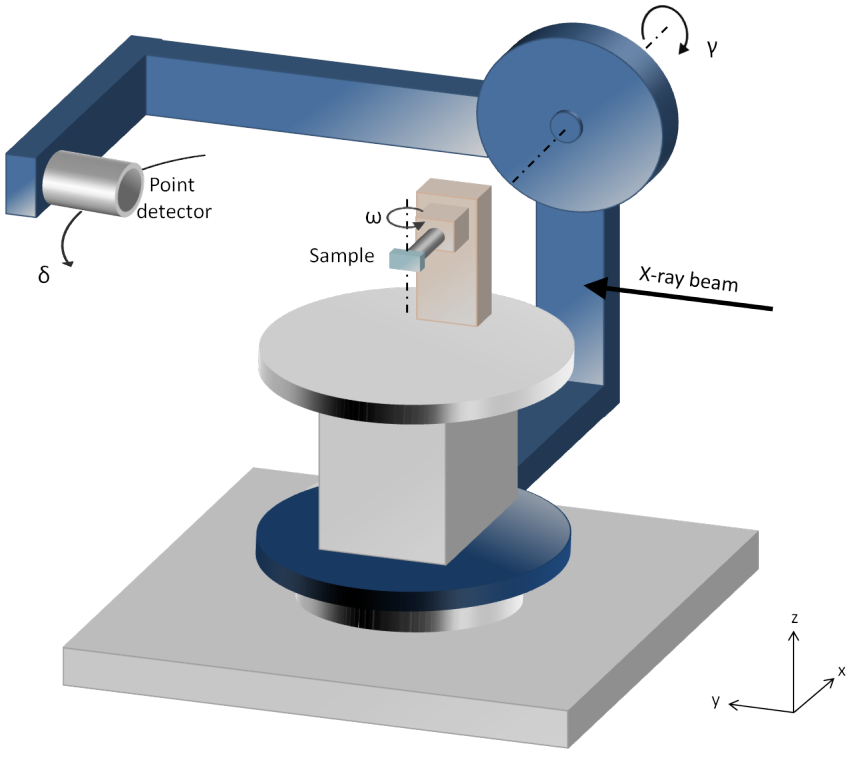

(b)

Figure 3.7: Diffractometer of EH2. (a) Photo of the diffractometer. (b) Schematic of the detector and sample rotational stages.

space can be simply specified in terms of the (hkl) coordinates of the substrate reciprocal lattice: a crystallographic absolute reference frame (the sample reference frame according to the nomenclature introduced in Section 2.3.2) is thus now promptly available. In other words, the analogue of the calculations presented in Section 2.3.2 (necessary for the analysis of the CCD detector data) are automatically carried out by the diffractometer control software. As well as extremely simplifying the analysis of the data, it allowed to completely get rid of the problem related to the mounting offset: a precise definition of the crystal preferred orientation could thus be achieved. The main drawback is represented by the limited field of view of the point detector as compared to the CCD one. A comprehensive investigation of the sample texture properties would be much slower and less effective: a traditional 0D diffraction experiment is really convenient only when one aims to investigate with a greater precision small circumscribed regions of the reciprocal space. Since no calculation had to be done, the mathematical description of a single crystal diffractometer is not reported and can be extensively found in literature: a description of the four-circle diffractometer is provided in the work of Busing and Levy [8], while an extension for the case of a six-circle diffractometer is presented by You [59].

Chapter 4

Gold and $SrTiO_3$ crystals preferred orientations

In this chapter, the preliminary texture analysis undertaken on the samples introduced in Section 1.2 is discussed. Starting from the data collected through the experimental setup described in the previous chapter, Section 4.1 outlines the first steps of the data analysis along with basic experimental results. Section 4.2 makes an extensively use of the tools presented in Section 2.3.2 to properly display the texture properties of the samples under study. A description of the main experimental findings is also provided: in particular, the presence of two Au nanoparticles preferred vertical (normal to the substrate surface) orientations, namely (111) and (002), is highlighted. The conclusions achieved constitute the starting point for the investigation constituting the subject of the following chapter.

4.1 Azimuthal regrouping of the CCD diffraction images and textured rings integration

The starting point of the texture analysis presented in this chapter is constituted by the images (also called *frames*) acquired through the CCD area detector setup introduced in Section 3.2. An example is provided by Figure 4.1, which shows a single raw frame (with dark noise correction) relative to the sample with 8 nm of Au for fixed values of the sample mounting rotations (see Figure 3.4). As can be clearly seen, a single acquisition allows to collect the diffracted intensity of multiple diffraction rings (each corresponding to a different 2θ value), originating from both the STO thin film and the Au nanoparticles. The reader is encouraged to notice that the rings labeled with "STO" in Figure 4.1 come from the thin film grown over the annealed Au layer and not from the substrate: the latter indeed produces sharp and bright spots rather then powder-like Debye rings. Their origin is briefly discussed later in this section. The dark areas at the image edges are simply due to the fixing glue of the optical fibers used to connect the CCD active area to the detector fluorescent screen. The vertical white stripe of low intensity derives from a beam stopper exploited to avoid a

bright substrate reflection in the middle of the frames.

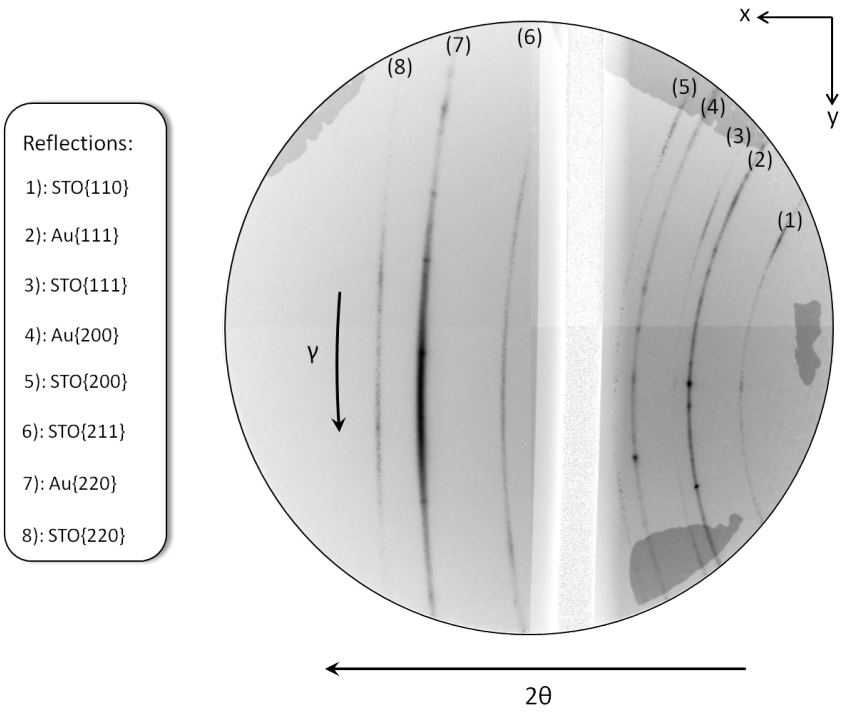

Figure 4.1: Single acquisition (*frame*) of the CCD area detector (exposure time of 5 ms) described in Section 3.2. The different textured diffraction rings are numbered in increasing order of the 2θ angle. The increasing directions of the diffraction space angles $(2\theta, \gamma)$ are specified, along with the detector plane axes (defined in Section 2.3.2). The image refers to the sample with 8 nm of Au.

The presence of a strong texture is immediately evident through a quick look at the detector frame. In general the diffraction rings are far from displaying the typical uniform intensity of an ideal, untextured powder sample: on the contrary, they exhibit bright spots alternated to regions of lower intensity. This means that both the Au nanoparticles and the STO thin film are characterized by the presence of crystalline preferred orientations: the framework within which the present work is placed is thus the one outlined in Section 2.3. At this point it is worth noticing that the samples addressed by the present investigation are not the traditional polycristalline samples encountered in the field of textured materials studies (as introduced in Section 2.3.1). Rather than the usual polycrystalline grains, they are indeed made up by nanoparticles grown on a single crystal substrate and dispersed in a host matrix of a different material. Nevertheless, the small crystal constituting each Au nanoparticle actually acts in the same way as a grain of a polycrystalline sample. The crystallographic orientational properties of the collection of all the nanoparticles can thus be investigated resorting to the same tools normally used for traditional polycrystalline textured materials.

Another promptly evident feature is that the diffraction rings produced by the STO thin film can be seen only in the samples with 8 and 5.3 nm of Au. Their presence is clear evidence of the polycrystalline character of the STO overlayer above a certain value of the initial Au layer thickness. This threshold value seems to lie between 4 and 5.3 nm. In fact, as can be seen in Figure 4.2, for the sample with 4 nm of Au they are already absent and

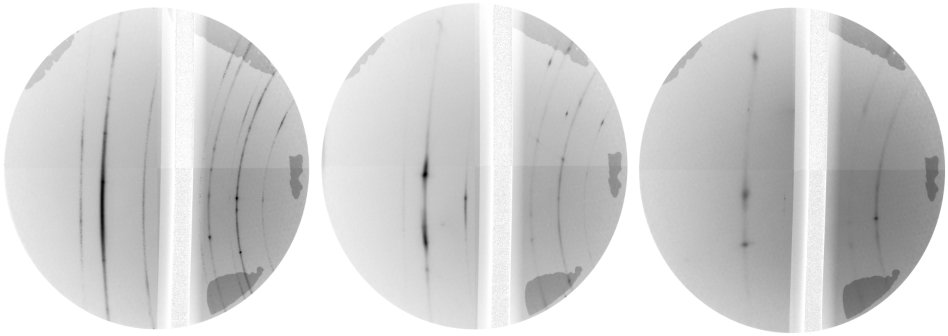

(a) 8nm **(b)** 5.3nm **(c)** 4nm

Figure 4.2: Diffraction images for the different values of the initial Au layer thickness: the absence of the STO rings for the sample with 4 nm of Au is evident. The image for 8 nm of Au is the same shown in Figure 4.1.

the same stands for lower Au thicknesses. For these samples then, the overlayer epitaxially grows along the (001) direction, as expected for the homoepitaxial system STO thin film / STO(001) single crystal substrate. This is particularly evident from the diffraction pattern of Figure 4.3, displaying the integrated intensity along the γ direction as a function of the scattering angle 2θ. The peaks originating from the STO rings (marked with an arrow) are clearly present in the 8 nm sample and, even though with a definitely smaller integrated intensity, in the 5.3 nm one too. On the contrary, they are absent for the 4 nm sample, where only the Au peaks can be seen. The loss of the perfect (001) epitaxy might be attributed to structural modifications of the STO lattice induced by the presence of the embedded Au nanoparticles: it is possible indeed to imagine that when the amount of deposited Au is high enough the resulting great number of nanoparticles significantly distort the perfect crystalline arrangement of the STO atoms. An almost complete coverage of the substrate surface by the Au islands (see Section 1.2) could also explain the loss of the perfect epitaxy: in this case, the STO layer would actually grow over the Au layer, without being influenced anymore by the underlying substrate. This hypothesis is ruled out by the Scanning Electron Microscopy images of Figure 4.4, where it is shown that even for the sample with the greatest amount of Au, large areas of the substrate surface are left uncovered. However, for these Au thicknesses, the Au islands are significantly larger than the ones at lower thickness values. Therefore, for the STO atoms deposited on top of these large islands should be more difficult to diffuse to the substrate surface regions left uncovered by the Au atoms. They would then interact only with the Au 3D islands surface, without being directly influenced by the presence of the underlying substrate: this could possibly lead to the loss of the (001) epitaxy.

Another feature which emerges from Figure 4.3 is the drastic decrease (notice the scale factor used to represent the different curves) in the diffracted intensity coming from the Au nanoparticles as the initial Au layer thickness is decreased. The intensity drop is much more pronounced than expected if one tries to relate the diffracted intensity to the total volume of the diffracting crystal probed: going from 8 to 4 nm the Au total volume present is halved, while the intensity varies by more than two order of magnitude. One might argue that if

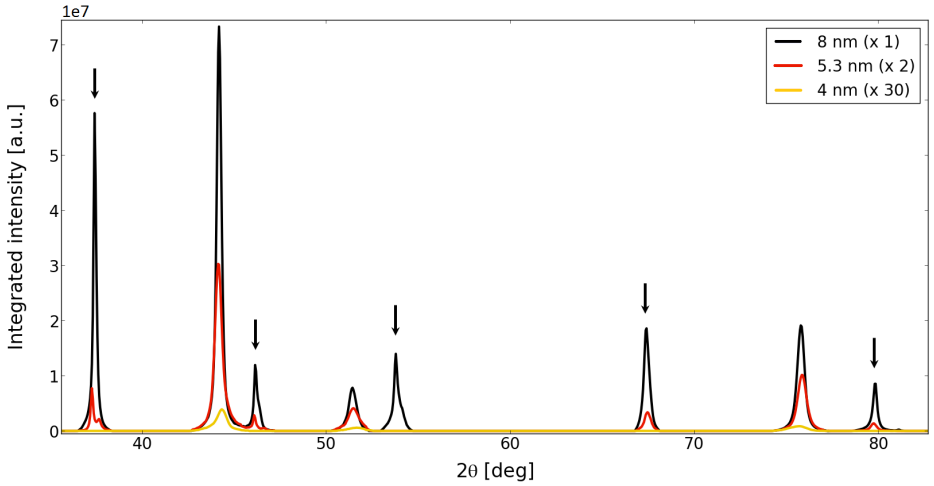

Figure 4.3: Diffracted intensity integrated over the γ angle as a function of the scattering angle 2θ for different Au thicknesses. The peaks coming from the STO thin film are marked with an arrow.

the particle size is smaller than the coherence length of the incident radiation (that is the case for the ESRF beamline ID06, where the coherence length is in the micrometer range) all atoms contribute coherently to the scattering intensity. In that case the intensity should be proportional to N^2, where N is the number of scattering atoms: if the density remains constant, the scattered intensity from each nanoparticle should be then proportional to V^2, being V the nanoparticle volume. However this aspect was not examined in depth and it will need further investigation. The weak signal for the samples with the lowest Au thicknesses represented a significant complication in the analysis of the corresponding diffraction data. It constituted a substantial problem particularly in the experiment performed with the diffractometer, as has been discussed in Section 3.3.

The first step to analyze the texture properties of such images is represented by the procedure known as *azimuthal regrouping*, also called *caking* (see Appendix B for more details). It consists of a polar transformation (performed by a dedicated software) which reduces the detector acquisitions to 2D patterns that can be treated in a more comfortable way. The azimuthal regrouped image derived from the detector acquisition of Figure 4.1 is shown in Figure 4.5. All the points on a vertical line of this 2D pattern share the same 2θ value: moving along such a line corresponds to span different values of the γ angle. Therefore, each diffraction ring of the detector acquisition is transposed to a vertical line on the azimuthal regrouped image. This is of course strictly true only in the ideal case of a perfect calibration of the analyzing software: in general there will be a small deviation due to the finite precision of the calibration process. For the data of the present work, the PyFAI [32] python tool was used to perform the azimuthal regrouping. This software package also applies some corrections to the raw detector frame: among these, the solid angle correction (which takes into account the different solid angles subtended by pixels in different positions) was used.

For every detector acquisition, each one acquired with a specific set of values for the sample rotational stages, the corresponding azimuthal regrouped image was calculated. In a textured material like the one considered, for a fixed sample position only the grains (in

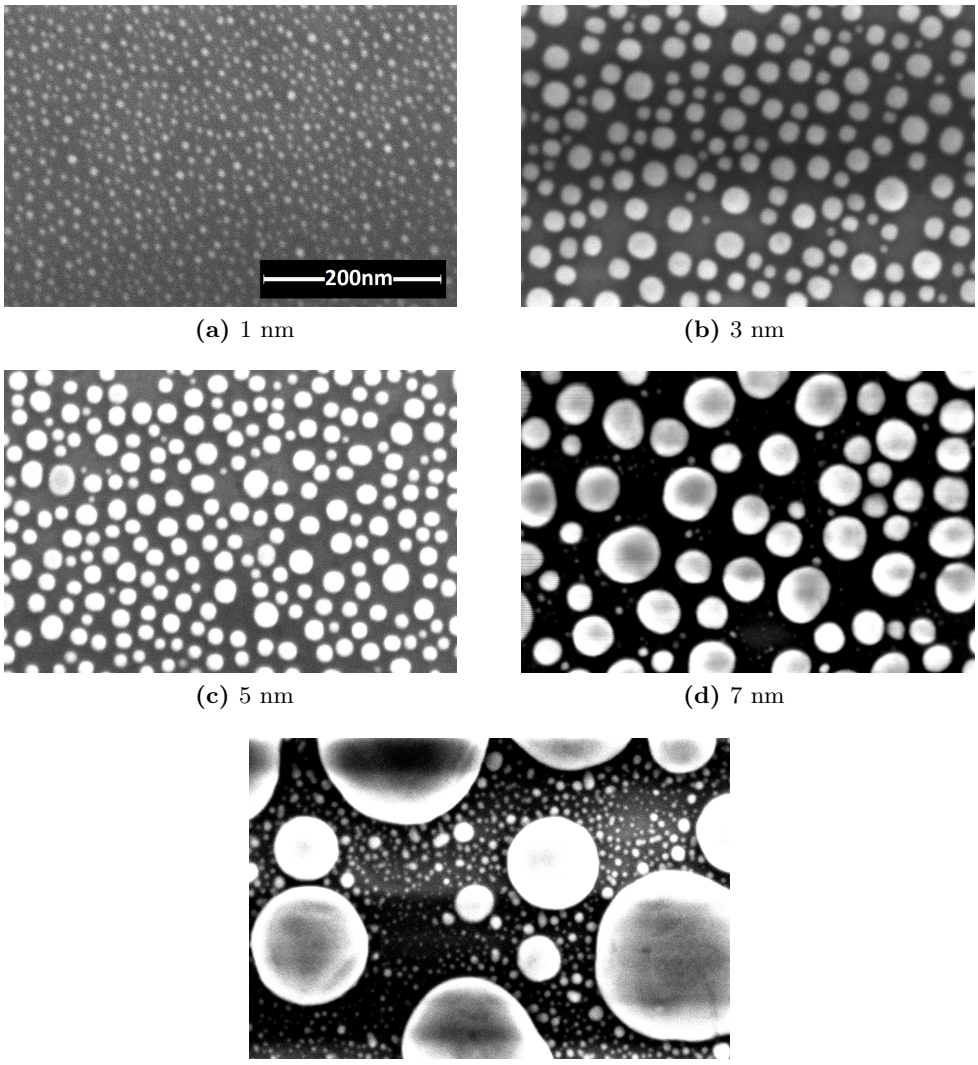

(a) 1 nm

(b) 3 nm

(c) 5 nm

(d) 7 nm

(e) 9 nm

Figure 4.4: Scanning electron microscopy images of the 3D Au islands formed by the thermal dewetting of the Au layer for different thickness values [5]. The images refer to samples prepared similarly to the ones considered in the present work, but without the STO thin film deposition step. The spatial scale is the same for all the images (see Figure 4.4a).

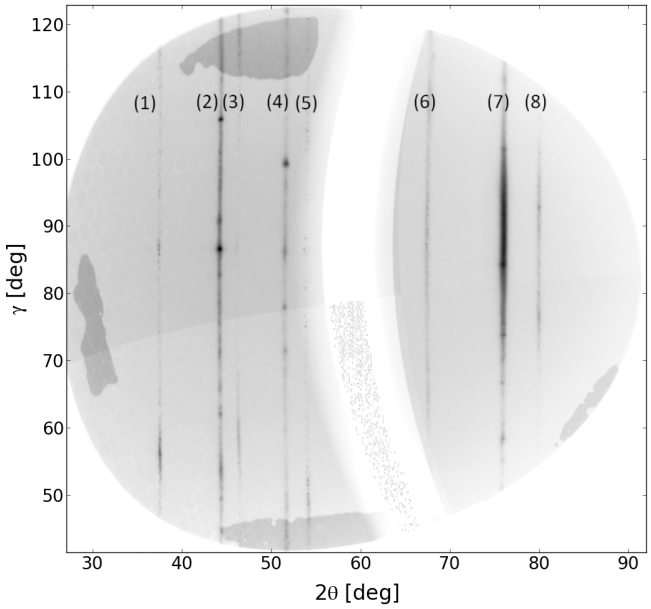

Figure 4.5: Azimuthal regrouped image as obtained through the PyFAI azimuthal regrouping algorithm (see Appendix B) applied to the detector frame shown in Figure 4.1. The numeration of the diffraction rings is the same adopted in the latter figure.

the case here considered the Au nanoparticles and the grains of the STO thin film) with a specific crystallographic orientation produce a beam of diffracted light on the detector. In order to probe the multiple preferred crystallographic orientations is then necessary to rotate the sample: this brings Au nanoparticles and STO thin film grains (for 8 and 5.3 nm of Au) with different orientations into diffraction conditions, thus allowing them to be seen on the detector. As a direct consequence, changing the values of the sample rotations causes the distribution of the diffracted intensity along the diffraction rings to vary. As an example, in Figure 4.6 is shown how the intensity of the Au{111} azimuthal regrouped diffraction ring varies along the γ direction as the ω angle (see Figure 3.4) is varied.

This approach can be undertaken in a more systematic way, through a procedure which is the natural extension of the one shown in Figure 4.6. Multiple detector frames are acquired, each with a different value of one of the sample rotations. To analyze the texture properties of a certain family of lattice planes, for instance Au{111}, the corresponding azimuthal regrouped diffraction ring is selected for each value of the sample rotation spanned. Then an integration of the type of equation 2.37 is performed over a 2θ range $2\Delta_{2\theta}$ large enough to include the whole diffraction ring. It is a good practice to choose a range sufficiently large to cover at least two times the FWHM of the ring. The result of the integration, for each position of the sample rotational stage considered, is the function $I_{hkl}(\gamma)$ of the {hkl}-ring intensity distribution (I_{111} if the Au{111} family is considered): it corresponds to I_{hkl} of equation 2.37 with fixed values for ω, ϕ and ψ. Calculating the function $I(\gamma)$ for each value of the sample angle varied leads to the intensity maps shown in Figure 4.7. In this particular case the sample rotational stage involved is the ω one: in the measurements performed it

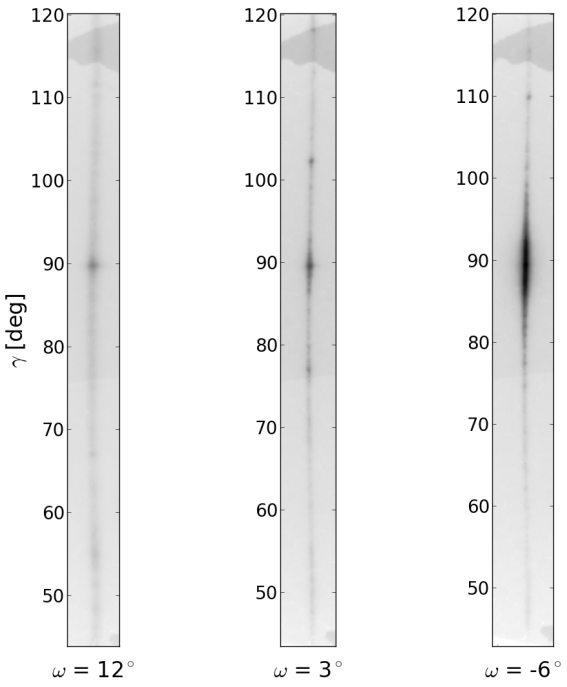

Figure 4.6: Azimuthal regrouped Au{111} diffraction rings (sample with 8 nm of Au) for three different values of the ω angle, as defined in Figure 3.4. Notice how the intensity distribution along the ring changes as ω is varied. Starting from an azimuthal regrouped image analogous to that of Figure 4.5, each one of the three images shown has been obtained through a selection over a 2θ interval centered on the Au{111} ring.

was varied over a range of 27° (or 28°) at steps of 0.1°. At the same time either the ψ or the η rotation (or both in the case $\phi \neq n\,90°$, $n = 0, 1, 2, 3$) were adjusted to a fixed value, such that the angle between the incident beam and the sample surface was kept positive (necessary condition for the Bragg diffraction geometry adopted). By means of a proper colorscale, each row of the intensity maps represents the function $I_{hkl}(\gamma)$ for a fixed value of ω, that is to say the intensity distribution of a diffraction ring for a fixed sample position. Different rows correspond to the function $I_{hkl}(\gamma)$ for different ω values. The maps therefore provide a straightforward visualization of the dependence of the diffraction rings integrated intensity distribution on the sample position.

4.2 Representation of the gold nanoparticles and $SrTiO_3$ grains preferred orientations: pole figures

Despite of their capability to show intensity variations following sample rotations, the intensity maps shown in the previous section do not provide an immediately comprehensible visualization of the sample preferred orientations. This task is much better accomplished by calculating the corresponding pole figures. After the 2θ integration described in the previous section, the integrated intensity for each value of the γ angle and each sample position $I_{hkl}(\gamma, \omega, \phi, \psi, \eta)$ is known. The function $I_{hkl}(\mathbf{h}_S^{hkl})$ to be represented in a pole figure can

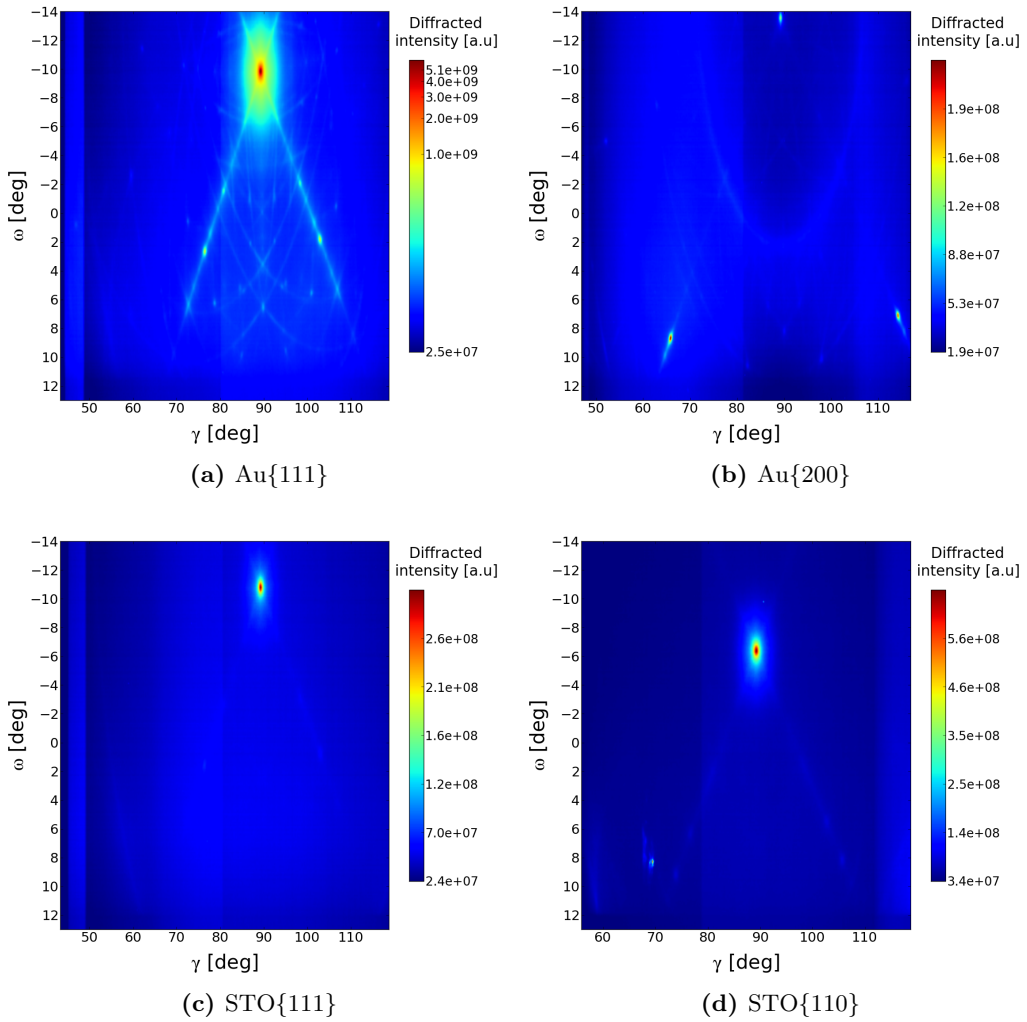

(a) Au{111} **(b)** Au{200}

(c) STO{111} **(d)** STO{110}

Figure 4.7: Intensity maps for different Au and STO crystalline planes families for the sample with 8 nm of Au. Each map shows through a colorscale the function $I_{hkl}(\gamma)$ of the intensity of the light diffracted by the {hkl} planes for different ω values. The angles mentioned are defined in Section 2.3.2.

thus be obtained by calculating the relation $\mathbf{h}_S^{hkl}(\gamma, \omega, \phi, \psi, \eta)$: this can be done through the extension 3.1 of the calculations presented in Section 2.3.2. As mentioned in Section 3.2, one of the offset in the sample mounting was not exactly known. An estimate could be attained through the pole figures of the STO{112} substrate peaks, whose presence could not be completely avoided despite of the experimental precautions adopted. The unknown offset directly affects the β values at which these peaks occur. If the $\mathbf{U}$ matrix was equal to the identity, they would give rise to peaks at $\chi = 35.26°$ and $\beta = n\,45°$ ($n = 1, 3, 5, 7$) (the angles here mentioned are defined in Figure 2.13). As can be seen in Figure 4.8, this occurs within a reasonably small error, which was estimated to be in any case smaller than 5° for the rotational unknown offset around the vertical axis. For this reason, in the pole figures reported from now on, the angular direction will be labeled using the substrate crystallographic Miller indices rather than the β values: $\beta = 0°$ and $\beta = 90°$ will then be labeled (100) and (010) respectively (having assigned the (001) direction to the substrate surface normal). This would be strictly true only if the relation $\mathbf{U} = \mathbf{I}$ was exactly valid. Hereafter, the pole figures for the Au{111} and Au{200} nanoparticles crystalline planes (Figures 4.10 and 4.12) and STO{111} and STO{110} thin film ones (Figures 4.14 and 4.15) are reported for all the different values of the initial Au layer thickness available at the time the first experiment was performed. They were all obtained by varying the ω sample rotational stage as described earlier in this section. It is evident how the type of scans performed allow to cover only a limited angular region: this is nevertheless sufficient to rough out some preliminary conclusions.

The main feature which immediately stands out is the presence, for all the samples, of a strong Au{111} peak along the direction normal to the substrate surface, i.e (001). It represents a clear proof that a very large number of Au nanoparticles are oriented with the {111} crystal direction along the major axis of the ellipse (see Figure 1.11), pointing toward the sample surface. This is also a nice confirmation of previous XRD and TEM measurements results obtained by Christke et al. [13] and Bernhardt [4]. Moreover, the {111} orientation of the Au nanoparticles is consistent with the strong tendency of Au to grow along the {111} direction over $SrTiO_3$(001) substrate, predicted by the thermodynamical and kinetical consideration presented in Section 2.2 and documented in literature [16]. It is important to notice that the system under study is not the traditional Au layer grown over an STO substrate found in literature. The STO thin film growth, which leads to the embedded nanoparticles formation, may in principle modify the crystallographic orientation of the underlying Au dewetted layer. The Au nanoparticles may then be oriented in a different way with respect to the Au islands present prior to the thin film deposition. Actually, this does not seem to be the case, since the Au{111} peak in the vertical direction was also clearly found in the sample without the STO top layer, as can be seen in Figure 4.9a. Therefore, as long as the direction normal to the substrate surface is considered, the crystallographic orientation of the Au nanoparticles seems to directly descend from that of the 3D islands forming the Au dewetted layer; in other words the deposition of the STO overlayer does not significantly modify the main Au crystallographic orientation (at least for an initial Au layer thickness around 5 nm).

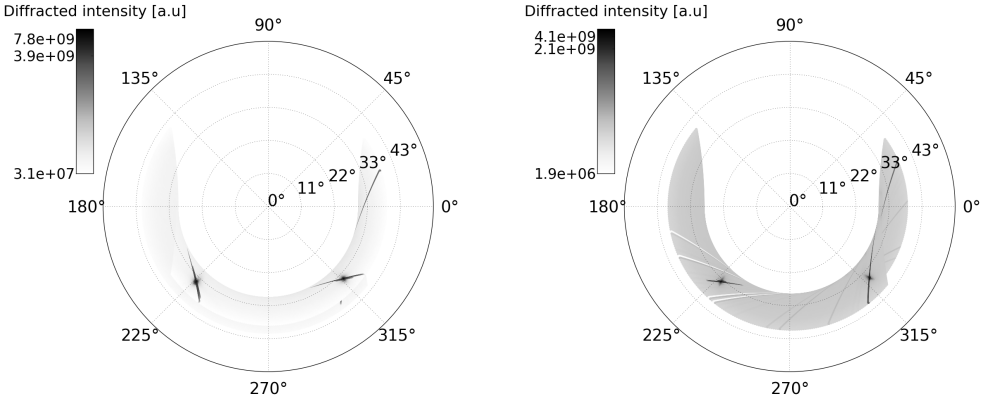

(a) 8 nm

(b) 5.3 nm

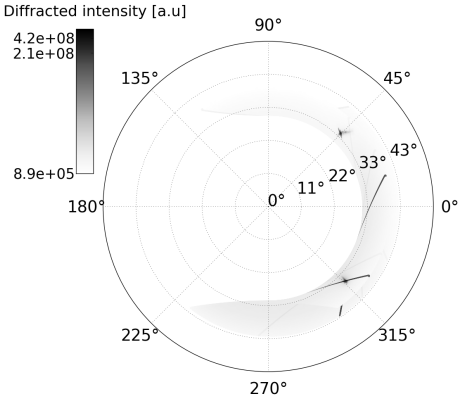

(c) 4 nm

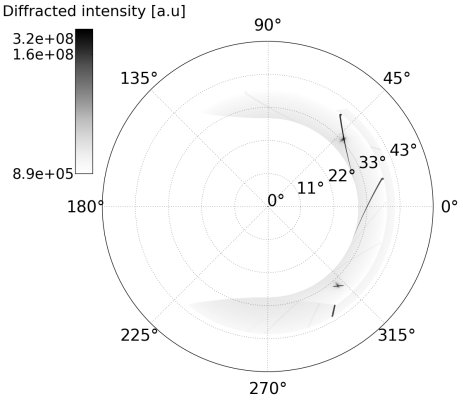

(d) 3 nm

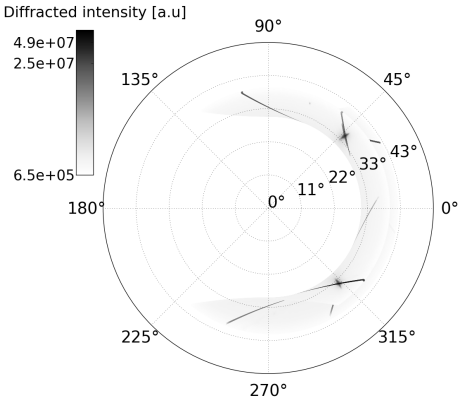

(e) 2 nm

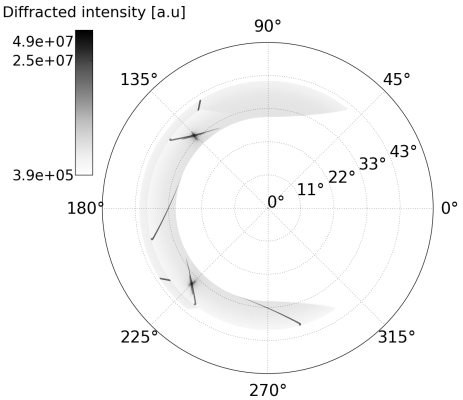

(f) 1 nm

Figure 4.8: Substrate {112} pole figures for the several samples studied.

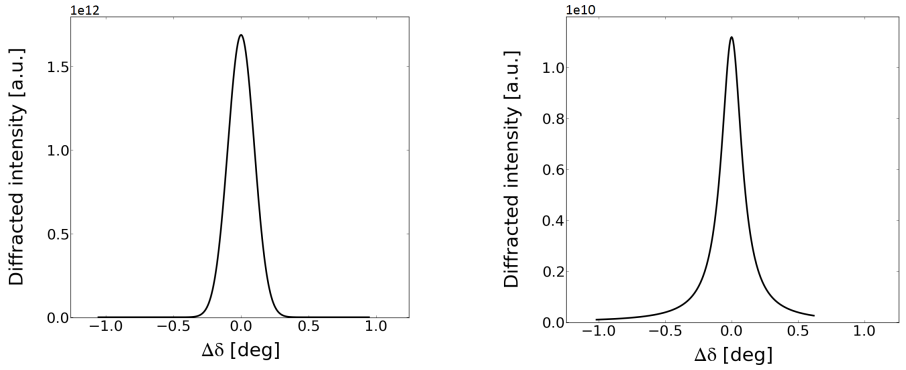

(a) Au(111) **(b)** Au(002)

Figure 4.9: Au peaks along the substrate (001) direction, normal to the substrate surface, for the sample with 5 nm of Au layer thickness without STO thin film. The peaks were recorder through a detector scan of the diffractometer (Figure 3.7b). Note the different intensity scale between the two peaks.

A possible exception may be provided by the sample with 1 nm of initial Au layer thickness. While the central Au{111} peak exhibits a rounded shape for all the samples with a Au layer thickness between 8 nm and 2 nm, for the 1 nm sample it displays a cross-like shape, with arms extending along the {110} substrate directions (see Figure 4.10f). The presence of this intriguing feature was clearly confirmed by the data collected during the second experiment: coupling the detector and the sample degrees of freedom of the diffractometer, the HK mesh-scan shown in Figure 4.11a was realized. As in the (*hkl*) labels in the pole figures, H and K represent the diffraction vector components (i.e. the Miller indices) which lie on the plane of the sample surface. Considering again the diffractometer data, an even more pronounced cross-like feature of the same type was found also in the sample with 1.5 nm of Au (Figure 4.11b). From these mesh-scans the presence of 4 peaks of diffracted radiation (sharper for the 1.5 nm sample) distributed around the central one along the H=K lines is clearly highlighted. A similar mesh-scan performed for greater values of the Au thickness led to the central peak only, as would be expected by the inspection of the corresponding pole figures. From the data collected it is not possible to determine whether the occurrence of this odd peak shape is somehow induced by the growth of the STO thin film or is already present before its deposition. To resolve the issue, samples with 1 and 1.5 nm of Au, grown in the same conditions but without the deposition of the STO layer, would have been available. Anyway this is not the only peculiarity displayed by the samples with the lowest available initial Au layer thickness. Their crystallographic properties seems to significantly differ from the other samples, as will be discussed extensively in Chapter 5.

Another aspect shown by the Au{111} pole figures is that the central peak for the sample with 8 nm of Au is much more smeared out and larger than for the other samples. This could be attributed to the greater amount of Au present in this case. It is possible to imagine that the number of Au nanoparticles to accomodate inside the STO matrix is too large for a rigid crystallographic orientation to hold. A possible interaction between neighboring nanoparticles can even be supposed. In general, the situation looks somehow more confused,

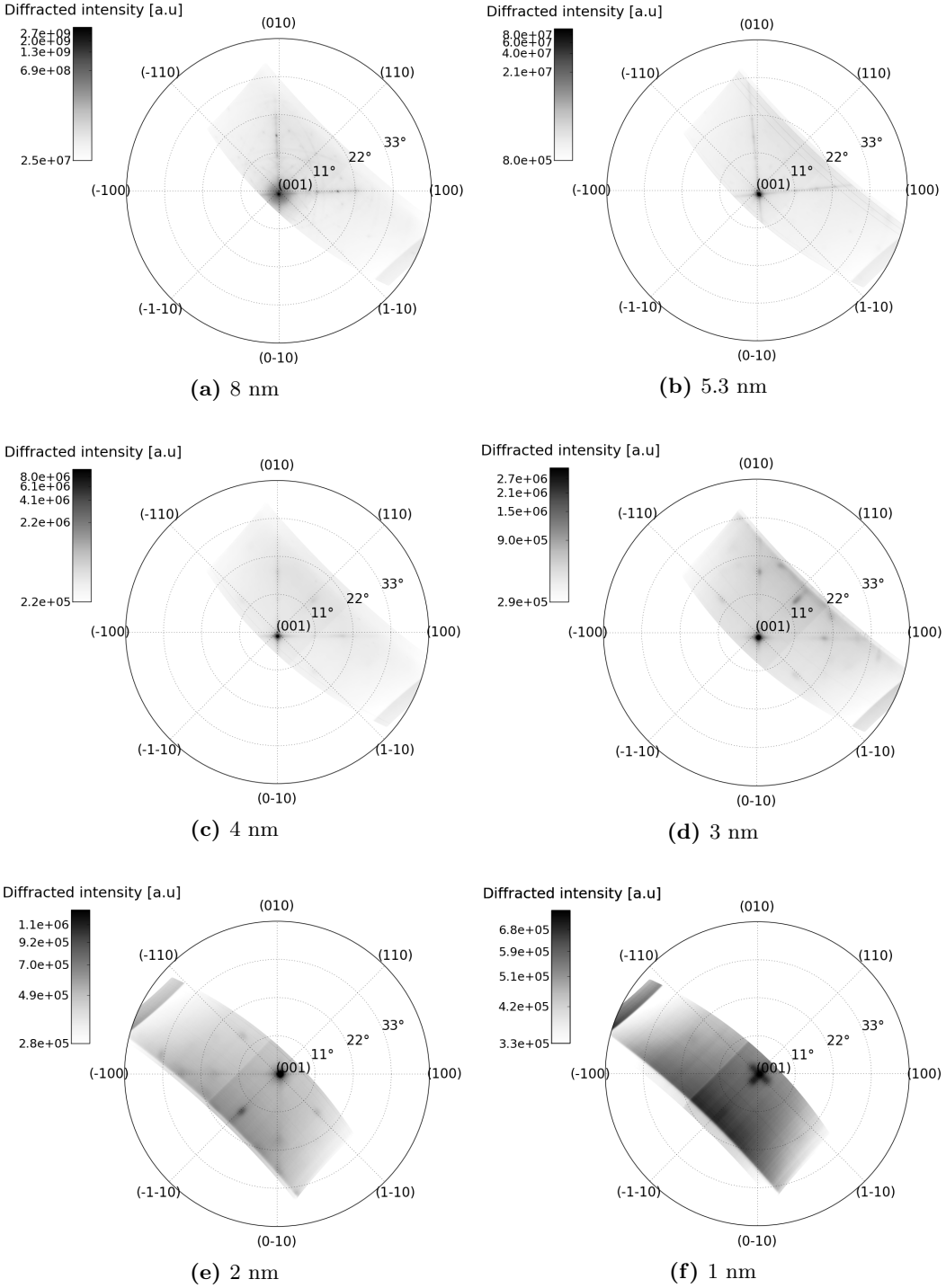

(a) 8 nm **(b)** 5.3 nm

(c) 4 nm **(d)** 3 nm

(e) 2 nm **(f)** 1 nm

Figure 4.10: Au{111} pole figures for different values of the initial Au layer thickness.

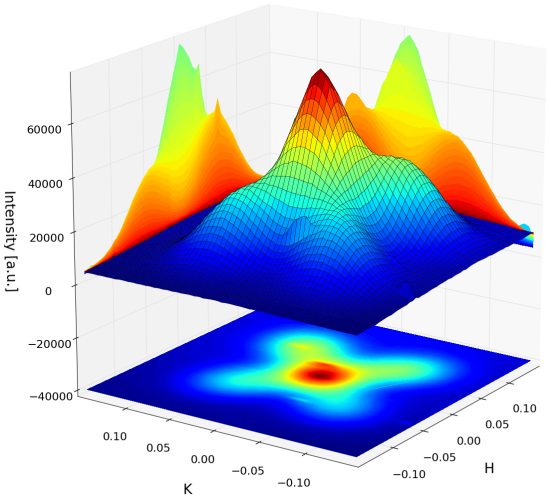

(a) 1 nm

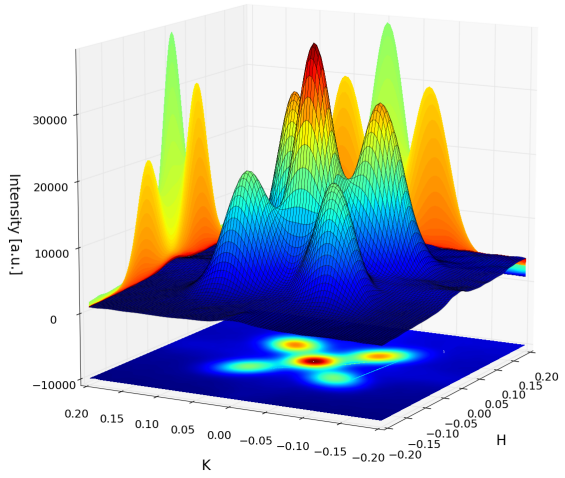

(b) 1.5 nm

Figure 4.11: Au{111} diffracted intensity for two different initial Au layer thicknesses as a function of the diffraction vectors components in the plane of the sample surface. Four peaks of diffracted intensity are present around the central, more intense, one.

as the presence of additional lines and small spots (along the (100) and (010) at $\chi \approx 11°$ and $\chi \approx 16°$) testifies. Other Au nanoparticles preferred orientations in addition to the central one are also clearly visible for the samples with 3 and 2 nm of Au. In both cases they cause the presence of spots in the region between $\chi = 11°$ and $\chi = 22°$ along the {110} and {100} substrate directions. These additional features are less visible in the 4 nm sample and seem not to be present for the samples with 5.3 and 8 nm of Au. For these latter samples, dark continuous lines of diffracted intensity instead appear along directions almost parallel to the (100) and (010) (the small deviation observed could be simply due to the limited precision of the caking program calibration).

As well as the {111}-oriented nanoparticles, there seem to be present a certain fraction of nanoparticles oriented with the {200} direction normal to the substrate. All the Au{200} pole figures indeed present a tiny peak in the center (Figure 4.12). This result was not expected since the previous XRD measurements performed before the experiments presented in this work had not shown the presence of such a peak: this is likely to be attributed to the lower resolution and intensity available with the laboratory conventional source used. Nonetheless, the presence of {200}-oriented nanoparticles was subsequently confirmed by XRD and TEM measurements conducted by Bernhardt et al. [5]. Even for this second family of nanoparticles, the orientation very likely originates from that of the Au islands present prior to the deposition of the STO thin film. A Au(002) peak was indeed clearly found in the sample without STO layer, as shown in Figure 4.9b (here the (002) notation is used rather than the more general {200} to stress the alignment along the vertical (001) substrate direction). Since the structure factor of all the allowed Au peaks (equation (2.13)) is constant and equal to $4f$, f being the atomic form factor, a rough indication of the abundance of the two orientations can be obtained evaluating the ratio of the corresponding diffracted intensities (a precise calculation is beyond the scope of the present discussion). An evaluation of the peaks areas led to a ratio $I_{111}/I_{002} \approx 110$: the {111} orientation thus seems to be much more abundant than the {200} one, at least for the sample without STO top layer. Actually the same observation seems to be valid also for the samples with the STO thin film, whose Au(111) and Au(002) diffraction peaks along the vertical direction are shown in Figure 4.13. The value of the ratio I_{111}/I_{002} varies from one Au thickness to another, but a large minimum value of 43.7 was in any case found. The values estimated seem to be in agreement with the ones obtained by Bernhardt et al. [5]. This great difference in the relative abundance represent a reasonable explanation for the absence of this peak in the diffraction data collected by Bernhardt [4] before the experiments here considered. The presence of multiple Au growth directions is in agreement with the expected polycrystalline character of Au films grown over $SrTiO_3$(001) substrates, discussed in Section 2.2. Moreover the high I_{111}/I_{002} is consistent with the high Au surface energy anisotropy and diffusion coefficient on the substrate surface.

As for the Au{111} pole figures, other features are present in addition to the central peak. In particular, bright spots are present approximately along the (100) and the (010) substrate directions at a χ angle around 33° for the samples with 8, 5.3 and 3 nm of Au. The pole figure for the 5.3 nm sample displays an evident sequence of circularly arranged peaks as well.

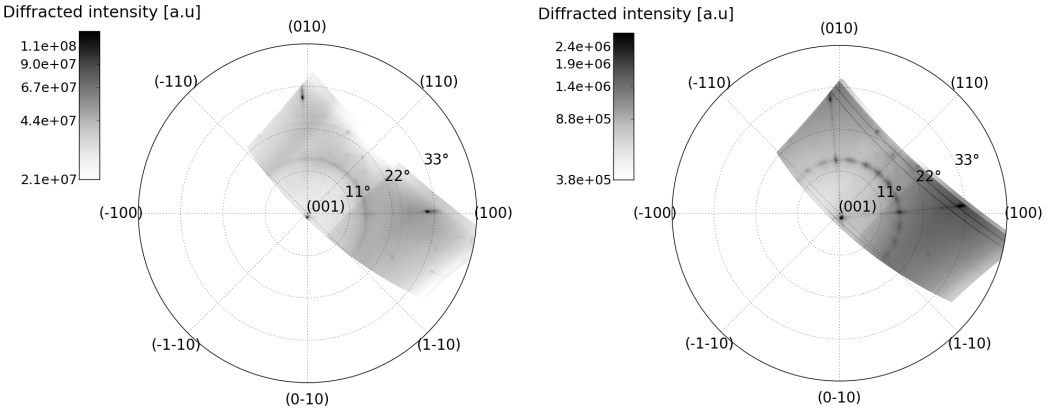

(a) 8 nm

(b) 5.3 nm

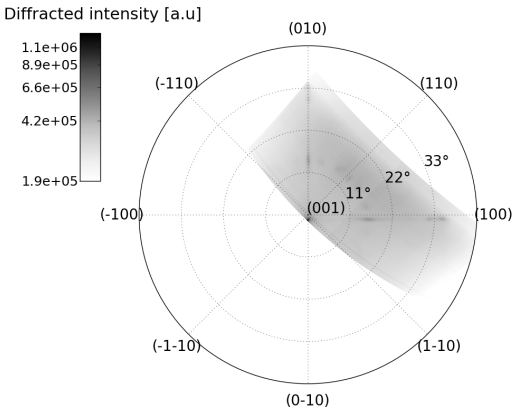

(c) 4 nm

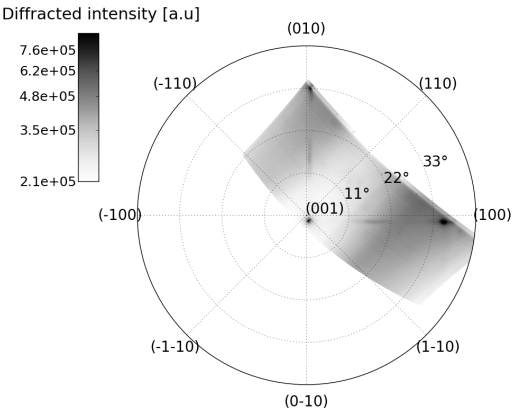

(d) 3 nm

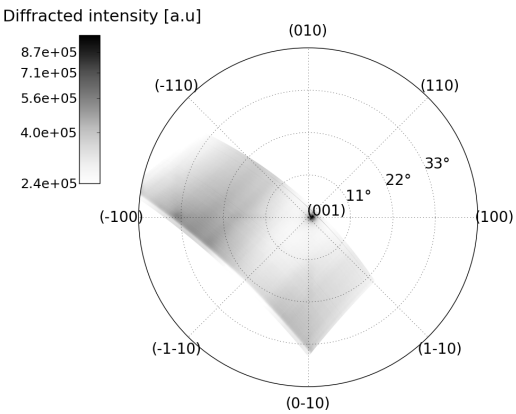

(e) 2 nm

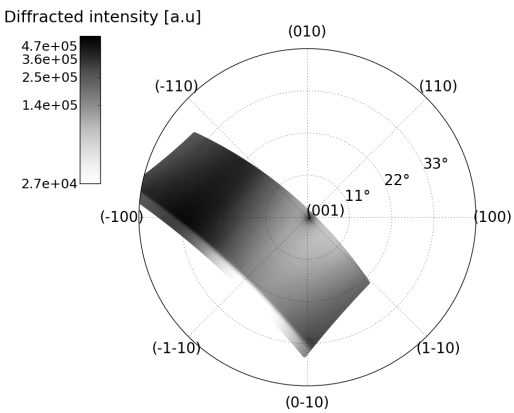

(f) 1 nm

Figure 4.12: Au{200} pole figures for different values of the initial Au layer thickness.

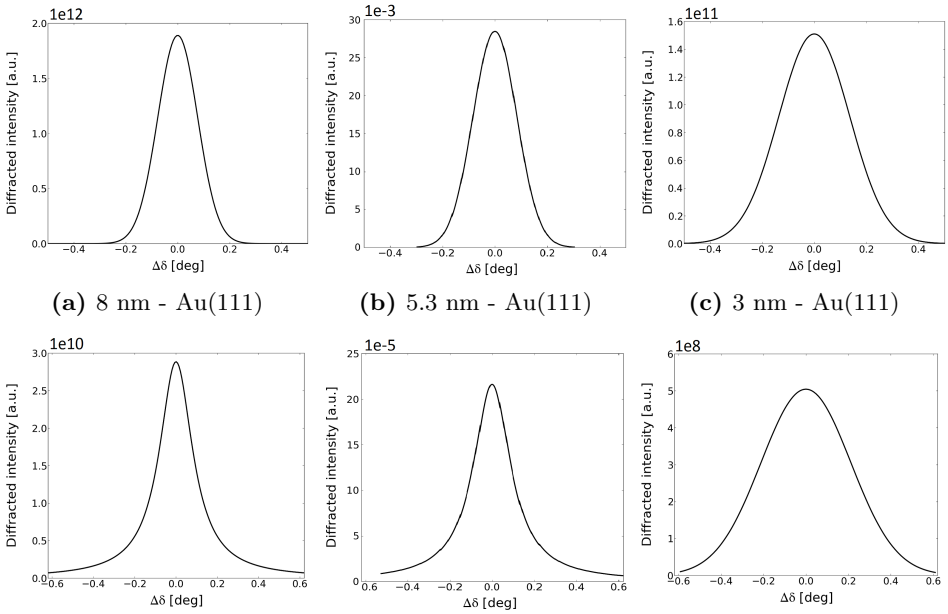

(a) 8 nm - Au(111) **(b)** 5.3 nm - Au(111) **(c)** 3 nm - Au(111)

(d) 8 nm - Au(200) **(e)** 5.3 nm - Au(200) **(f)** 3 nm - Au(200)

Figure 4.13: Au peaks along the substrate (001) direction, normal to the substrate surface, for samples with different initial Au layer thickness. The peaks were recorder through a detector scan of the diffractometer (Figure 3.7b). Note the different intensity scale between the Au(111) and the Au(002) peak for each thickness value.

The reader is invited to notice that the out of vertical additional features of the Au{200} pole figures cannot be simply attributed to the presence of the {111}-oriented nanoparticles (and viceversa for the Au{111} pole figures). This can be easily verified considering the χ value of the additional spots mentioned above and the angle between the (111) and the (002) lattice directions, equal to 54.74° (see also Figure 5.13).

With respect to the STO thin film, as mentioned earlier in this chapter, it exhibits an almost perfect (001) homoepitaxy on the $SrTiO_3$(001) substrate surface for an initial Au layer thickness between 1 and 4 nm. For these samples the STO thin film can be regarded as a perfect single crystal with no textured properties to be investigated. On the contrary, for the samples with 5.3 and 8 nm of Au, a rather polycrystalline thin film is obtained. As shown in Figures 4.14 and 4.15, the polycristalline thin film mainly exhibits two types of grains, which will be referred to as the STO *secondary phases*. They differ for the preferred crystalline orientation along the substrate surface normal, namely the {111} for the first type of grain and the {110} for the second type and they have also been observed by Bernhardt [4]. For both types, the corresponding central peak in the pole figures is weaker and sharper for the sample with 5.3 nm of Au. This evidence, as well as the absence of this secondary phases for lower Au thickness, leads to the obvious conclusion that the polycrystalline character is induced by the Au presence and increases as the amount of Au increases. As proposed earlier in this section, it's origin may be attributed to structural modification induced by the Au nanoparticles or the large 3D islands of the initial Au layer.

As a conclusion of the present chapter, it is possible to claim that the scenario emerged at the end of the preliminary textured analysis just presented is rather diversified. Many

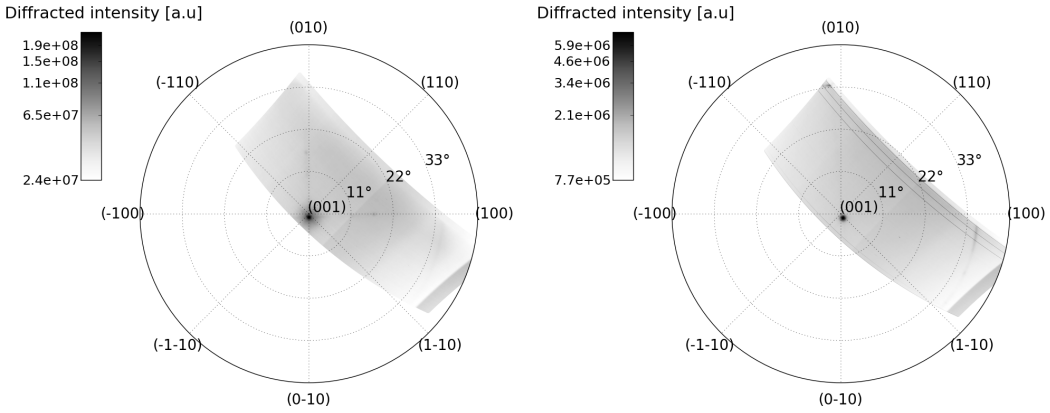

(a) 8 nm **(b)** 5.3 nm

Figure 4.14: STO{111} pole figures for different values of the initial Au layer thickness.

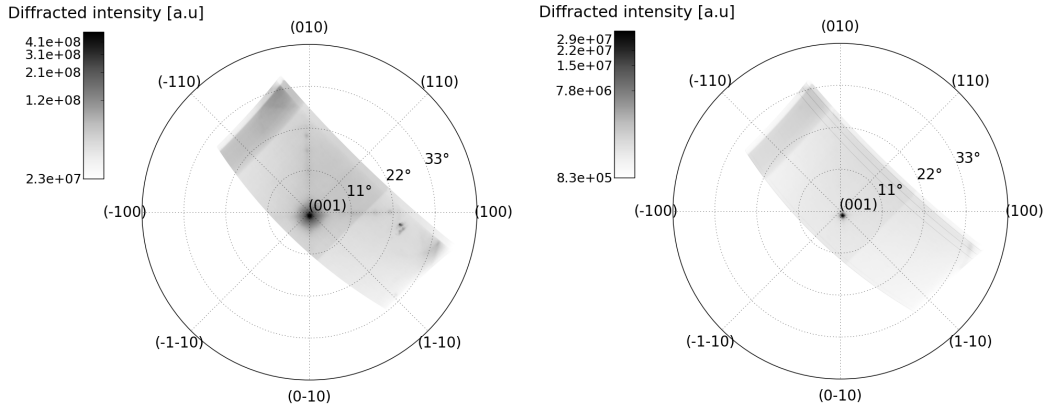

(a) 8 nm **(b)** 5.3 nm

Figure 4.15: STO{110} pole figures for different values of the initial Au layer thickness.

different features (more than predicted by the preliminary results of Bernhardt [4]) have been highlighted. In such an intricated situation, the challenge lied in identifying the potentially interesting aspects to study. A detailed investigation of all of them will in any case require future work. The following chapter focus on an aspect intentionally not discussed in this one, but which is nevertheless based on its findings. It consists of the investigation of the in-plane orientation of the two families of Au nanoparticles whose presence has been highlighted.

Chapter 5

Gold nanoparticles in-plane orientation

Starting from the experimental evidence presented in Chapter 4, the present chapter aims to extensively discuss a particular aspect of the nanoparticles crystalline properties, namely their in-plane orientation. In Section 5.1 important symmetry considerations necessary to properly interpret the experimental data are presented. Section 5.2 discusses in detail the investigation of the in-plane orientation of the Au nanoparticles. The experimental findings are shown and a possible interpretation is provided on the basis of the concepts outlined in Chapter 2 and of the symmetry considerations of Section 5.1. In particular the existence of two Au nanoparticles in-plane families for each vertical orientation found is highlighted and a dependance of the in-plane orientation on the amount of deposited Au is pointed out.

5.1 In-plane peaks periodicity: symmetry considerations

In the previous chapter, general experimental results emerging from the preliminary textured analysis undertaken on the samples have been presented. In particular, the presence of two families of Au nanoparticles has been shown, with either the {111} or the {200} aligned along the substrate (001) direction. Adopting the common notation found in literature (and already used in Section 2.2) these two families will be labeled throughout this chapter $(001)_{STO}||(111)_{Au}$ and $(001)_{STO}||(002)_{Au}$ respectively. Here the choice to consider the (111) and the (002) directions along the normal to the substrate surface, among all the equivalent {111} and {200} directions respectively, is purely arbitrary and dictated only by reasons of convenience. From now on this convention will be adopted, avoiding the usage of the curly brackets when referring to the vertical direction.

The orientation is not fully defined by the preferred orientation along the vertical axis (normal to the substrate surface) alone. A complete characterization of the crystalline preferred orientation of both the nanoparticles families thus requires the investigation of the in-plane orientation, that is to say in a direction parallel to the substrate surface. Generally speaking, in order to determine the in-plane orientation, it is sufficient considering a recip-

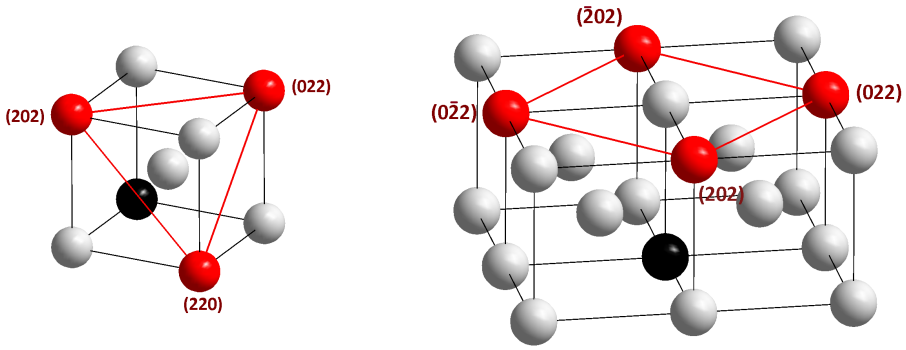

(a) (111) direction **(b)** (002) direction

Figure 5.1: Geometry of the Au{220} equivalent reciprocal lattice points for two different reciprocal lattice directions. The reciprocal lattice origin is represented by a dark sphere.

rocal space direction which has a non-zero projection on the plane of the substrate surface (in other words, that is not collinear with the vertical direction considered) and then measuring the periodicity of the corresponding diffraction peaks. In the remainder of the present chapter, such an investigation will be presented. The reciprocal lattice direction used to accomplish this task varied from one experiment to the other and for the two families of Au nanoparticles as well.

Let us take first the case of the $(001)_{STO} \,||\, (111)_{Au}$ nanoparticles. This is probably the most important case since most of the nanoparticles seems to prefer this orientation. There is also another reason which makes this case more intriguing. For this direction of growth, the Au(111) crystalline planes, with their 3-fold rotational symmetry, are indeed located in an environment which exhibits a completely different symmetry, that is to say the 4-fold rotational symmetry of the surrounding STO (001)-oriented matrix. The question that naturally arises is then how the hexagonal lattice of the Au(111) atoms "decides" to arrange itself on the STO(001) planes square lattice. In this case, for the study of the in-plane orientation, the diffraction from the two families of lattice planes Au{220} and Au{331} were exploited, the first for the experimental setup described in Section 3.2 and the second for the one of Section 3.3 respectively. In the CCD area detector experiment the Au{220} reflection was used for the other family of nanoparticles as well. As viewed from the (111) direction, the three symmetrically equivalent Au{220} reciprocal lattice points describes an equilateral triangle and are related one to another by 120° rotations around the (111) direction (see Figure 5.1a). From Figure 5.2a it is also evident that, as long as the (111) direction is considered, the Au{331} reciprocal lattice points are symmetrically equivalent to the Au{220}, being also related by 120° rotations. The corresponding diffraction peaks are then expected to exhibit the same periodicity. It is worth noticing that in this context, with "equivalent direction" (and the corresponding notation in curly brackets) are not strictly meant all the symmetrically equivalent directions, as normally done. The intention is to include, among all of them, only the ones which form a fixed angle with one of the possible equivalent (in its general meaning) Au{111} directions. For instance, considering the (111) reciprocal lattice direction, the (220), (202) and (022) are considered equivalent, since they form with the (111) the same angle of 36.26°. On the contrary they are not equivalent to the

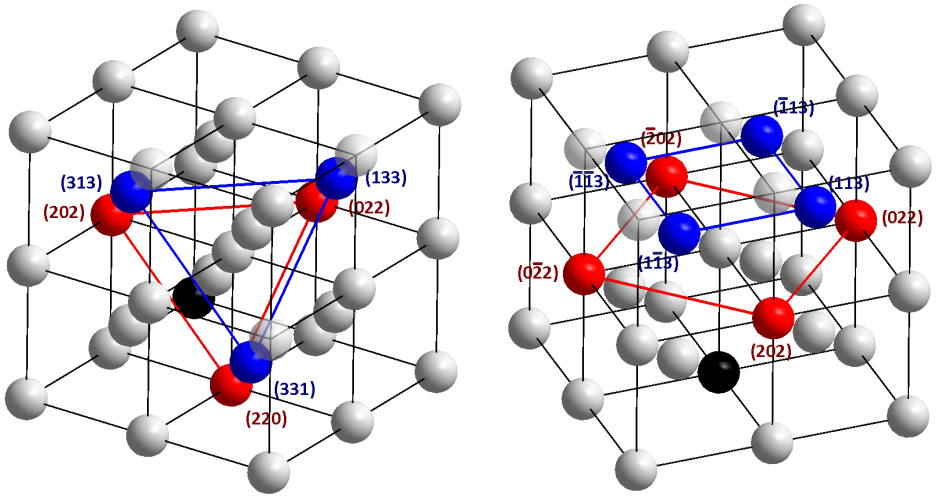

Figure 5.2: Geometry of two different families of reciprocal lattice points used for the in-plane investigation of the Au nanoparicles as alternatives to the Au{220} ones. The reciprocal lattice origin is represented by a dark sphere. (a) Au{331}. The 3-fold rotational symmetry around the (111) direction is equivalent to that of Au{220}. (b) Au{311}. The 4-fold symmetry around the (002) direction is equivalent to that of Au{220} apart from a 45° shift.

($\bar{2}02$), which is orthogonal to the (111). With reference to the aforementioned peaks, the in-plane orientation of the Au(111) lattice planes can be conveniently described introducing the β_{111} angle: as shown in Figure 5.3a, it is defined as the angle formed by the substrate (100) direction and the direction passing through one of the Au{220} (or equivalently Au{331}) lattice points and the center of the equilateral triangle they form (which turns out to be the ($11\bar{2}$)). It is important here to stress the fact that, though similarly defined, the β_{111} angle substantially differs from the β angle of the pole figures. The latter, as shown in Figure 2.13b, identifies the position of a generic diffraction peak through the method of the stereographic projections: for a fixed value of β_{111}, multiple peaks at different β values are obtained, as explained later in this section.

The equilibrium value of the β_{111} angle is expected to be mainly determined by energetic arguments. Both in the case of the 3D Au islands present prior to the thin film deposition and in the case of the embedded Au nanoparticles, the in-plane atomic arrangement will be the one which minimize the Au/STO interface energy. The situation is of course rather different depending on which of the two systems, 3D islands or embedded nanoparticles, is considered. In the former case, the only interface present is the one between the (111) lattice planes of the islands and the single crystal substrate. On the other hand, in the latter case the interface energy between the ellipsoidal nanocrystal as a whole and the surrounding STO thin film has to be taken into account. The interface is thus more complicated, since it depends also on the crystallographic orientation of the terminating facets of each Au nanoparticles (not investigated yet). Anyway, as found for the vertical orientation, it is plausible to think that, even for the in-plane orientation, the arrangement of the 3D islands plays a major role in determining the embedded nanoparticles one.

In considering the possible $(001)_{STO} \,||\, (111)_{Au}$ nanoparticles in-plane orientation, some

important symmetry considerations have to be undertaken. Although the β_{111} angle has been defined by referring to the STO(100) direction, the (100) and (010) in-plane cubic main axes of the $SrTiO_3$ are actually totally equivalent: hence no preference has to be expected for the nanoparticles to form a β_{111} angle with respect to the (100) rather than the (010) direction. Therefore, given a certain value of β_{111}, all the values obtained through rotations multiple of 90° are equally possible. Moreover, considering the presence of the cubic mirror planes along the (100) and (010) directions, even the direction chosen to define β_{111} is arbitrary: a positive (counterclockwise) value is as likely to be present as a negative (clockwise) one. Taking into account the intrinsic 3-fold symmetry of the Au{220} (or equivalently Au{331}) reciprocal lattice points around the (111) axis , the β values of the total 24 equivalent (in the sense precised earlier in this section) Au{220} diffraction peaks expected can be formally expressed by the following combination

$$\beta = \pm\beta_{111} + n\,90° + m\,120° \qquad n = 0,1,2,3 \qquad m = 0,1,2 \tag{5.1}$$

where $\pm$ accounts for the mirror symmetry of the STO(001) substrate, $n\,90°$ for its 4-fold rotational symmetry and $m\,120°$ for the 3-fold rotational symmetry of the Au(111) planes. It is easy to verify that given the previous combination of possible orientations, the mirror symmetry defined by the {110} cubic mirror planes is automatically satisfied. Changing β_{111}, the position of the Au{220} lattice points (and their corresponding diffraction peaks) varies: the resultant Au{220} pole figure will thus exhibits spots at different values of the polar angle β, according to equation (5.1). Certain values of the β_{111} angle correspond to degenerate cases, where the overall number of diffraction peaks reduces from 24 to 12. It happens for $\beta_{111} = n\,30°$ and $\beta_{111} = n\,30° + 15°$ (with $n = 0,1,2,\ldots,10,11$) which give rise respectively to the following sequences of 30°-periodical β values:

$$\beta = n\,30° = 0°, 30°, 60°, 90° \ldots \tag{5.2}$$

$$\beta = n\,30° + 15° = 15°, 45°, 75°, 105° \ldots \tag{5.3}$$

The reader is encouraged to notice that these two cases correspond to the second and the first of the relations 2.17 found by Silly and Castell [46] respectively.

For the case of the $(001)_{STO}||(002)_{Au}$ nanoparticles family the Au{220} equivalent lattice points exhibit the usual 4-fold symmetry around the (002) direction (see Figure 5.1b). The Au{311} lattice points also probed to study the in-plane orientation in this case, exhibit the same symmetry. Contrary to the case of the Au{331} exploited for the other family of nanoparticles, they are not completely equivalent to the Au{220} ones: they are indeed shifted by a 45° rotation around the (002) axis, as shown in Figure 5.2b. Let's focus for the moment on the Au{220} lattice points: the same considerations stand for the Au{311} provided that one considers the aforementioned 45° shift. As for the previous case, the in-plane orientation can be defined by specifing the relative rotation of the Au crystal relative to the surrounding STO matrix: the corresponding angle is called β_{002}. As shown in Figure 5.3b, this angle is defined in this case relative to the STO(110) direction: in this way the case $\beta_{002} = 0°$ corresponds to the "cube on cube with 45° rotation" orientation as specified by

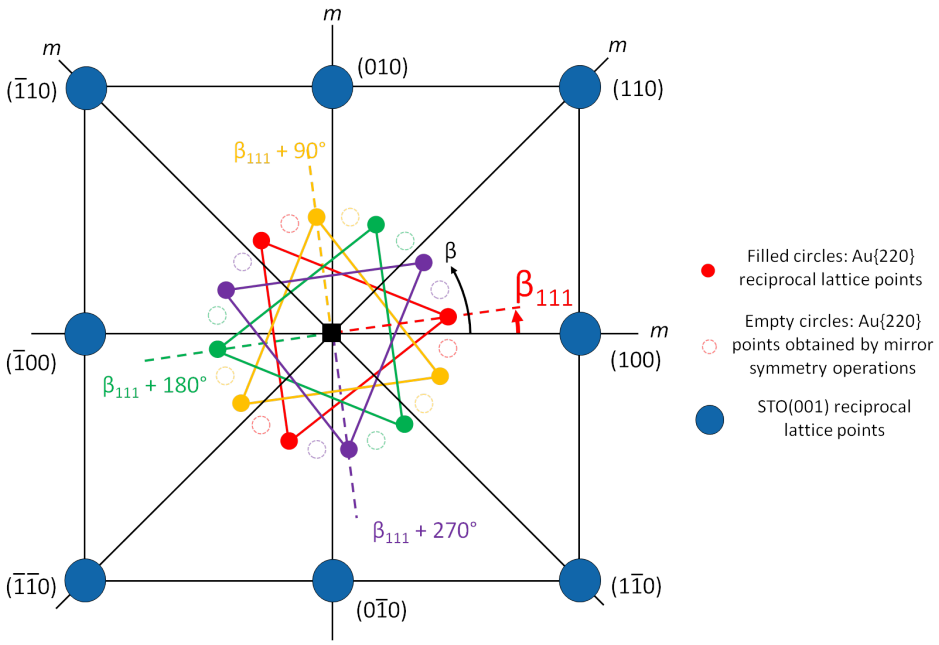

(a)

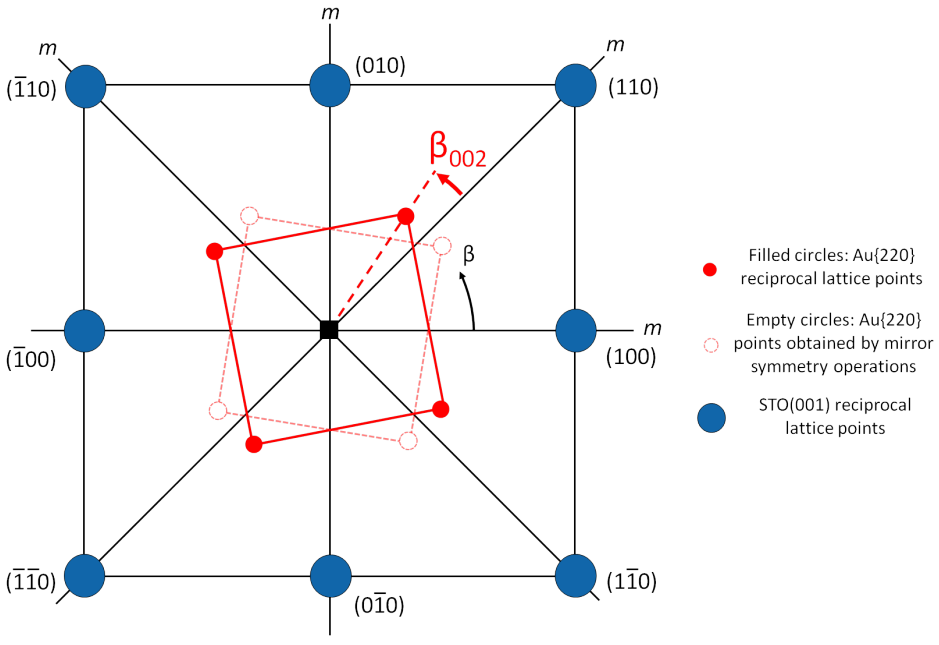

(b)

Figure 5.3: Au reciprocal lattice possible orientations with respect to the STO reciprocal lattice for two different vertical (normal to the plane of the page) directions of the Au lattice. In both cases the β pole figure angle is reported in black. (a) Au{220} reciprocal lattice points as viewed along the Au(111). Each colored triangle is equivalent to the red one described by the Au{220} points in Figure 5.1a. The in-plane orientation is defined through the angle β_{111}. (b) Au{220} reciprocal lattice points as viewed along the Au(002). Each colored square is equivalent to the red one described by the Au{220} points in Figure 5.1b. The in-plane orientation is defined through the angle β_{002}.

the second of the relations 2.16, while the case $\beta_{002} = 45°$ is equivalent to the "cube on cube" one.

The square described by the Au{220} lattice points automatically satisfies the 4-fold symmetry of the STO lattice (β_{002} could be indifferently defined relative to one of the equivalent STO{110} in plane directions). Only the mirror symmetry has to be additionally considered leading to the following combination for the equivalent diffraction peaks expected:

$$\beta = \pm\beta_{002} + n\,90° \qquad n = 0, 1, 2, 3 \tag{5.4}$$

where $\pm$ accounts for the mirror symmetry of the STO(001) substrate and $n\,90°$ for the 4-fold rotational symmetry of the Au(002) planes. In general 8 different values of β are present. As can be easily understood, the number of values reduces to 4 for the particular cases $\beta_{002} = n\,90°\,(n = 0, 1, 2, 3)$ and $\beta_{002} = n\,45°\,(n = 0, 1, 2, 3)$ which cause the Au{220} lattice points to lie on along the cubic face diagonal or the main STO cubic axis respectively. The equilibrium value of the β_{002} angle will in general result from the same energetic considerations outlined for the case of the $(001)_{STO}\,||\,(111)_{Au}$ nanoparticles.

5.2 Determination of the Au/$SrTiO_3$ relative in-plane orientation: dependence on the amount of deposited gold and role of the $SrTiO_3$ thin film

5.2.1 $(001)_{STO}\,||\,(111)_{Au}$ nanoparticles in-plane orientation

Given the symmetry considerations just discussed, this section aims to present the in-plane investigation experimental data collected and try to provide a possible interpretation. A first set of measurements were performed through the experimental setup of Section 3.2, addressing the $(001)_{STO}\,||\,(111)_{Au}$ nanoparticles in-plane orientation. For this purpose, the ω angle was set to the (negative) value necessary for the Au{220} lattice planes to satisfy the Bragg condition in the vertical $(X_L Y_L)$ scattering plane. In particular the ω value was chosen such that the latter condition would be satisfied for one of the Au{220} reciprocal lattice points of Figure 5.3a, all forming the same angle with the Au(111) direction. A scan of the ϕ angle over a range of 180° was then performed: in this way, every time one of the equivalent Au{220} reciprocal lattice vectors was to lie in the vertical scattering plane, a peak of diffracted light at $\gamma = 0°$ was observed on the CCD. The in-plane orientation could then be investigated by looking at the periodicity with whom the diffraction peaks appeared on the detector. In other words, such a ϕ scan allows to subsequently bring the Au reciprocal lattice points of Figure 5.3a into diffraction conditions. This kind of measurement is affected by the offsets in the sample mounting, which cause the ϕ axis to slightly deviate from the substrate normal. The offsets were found to be generally smaller than the FWHM of the ω scans for the Au peaks. Therefore, even if a precise evaluation of the diffracted intensity is not possible, they do not significantly affect the main experimental findings presented in the reminder of the present discussion. A more precise evaluation of the diffracted intensity was

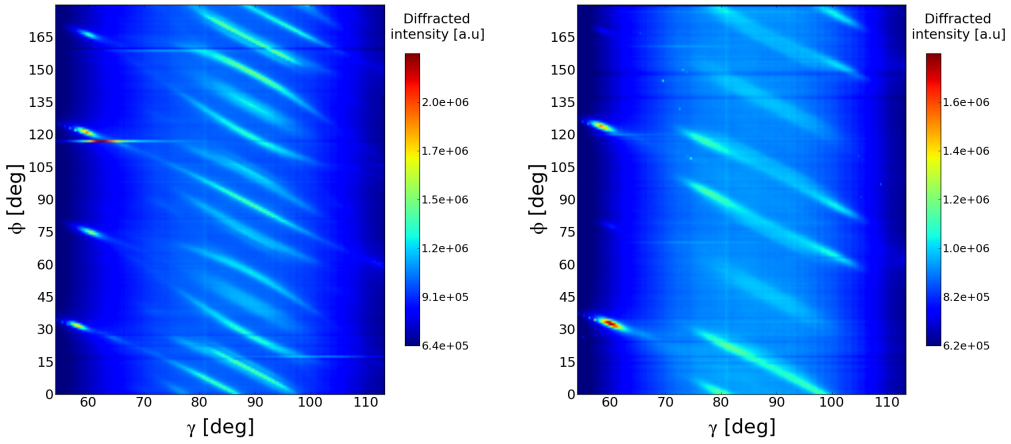

(a) 2 nm **(b)** 1 nm

Figure 5.4: Intensity maps corresponding to ϕ scans performed for samples with two different initial Au layer thickness values.

achieved by the usage of the diffractometer.

The collected data of each sample can be condensed also in this case in an intensity map analogue to the ones reported in Chapter 4. For the type of scan here considered, they show the ring intensity distribution as a function of the ϕ angle, instead of ω as for the previous chapter. As can be seen in Figure 5.4, these intensity maps exhibit bright streaks periodically spaced along the vertical direction: they are due to the differently oriented Au{220} lattice planes periodically entering and exiting the vertical scattering plane. To extract the information about the in-plane orientation from such intensity maps, it is sufficient to measure the periodicity of the aforementioned streaks along the ϕ-axis for $\gamma = 90°$ (vertical scattering plane). The graphs thus obtained are reported in Figure 5.5 and 5.6. The peaks

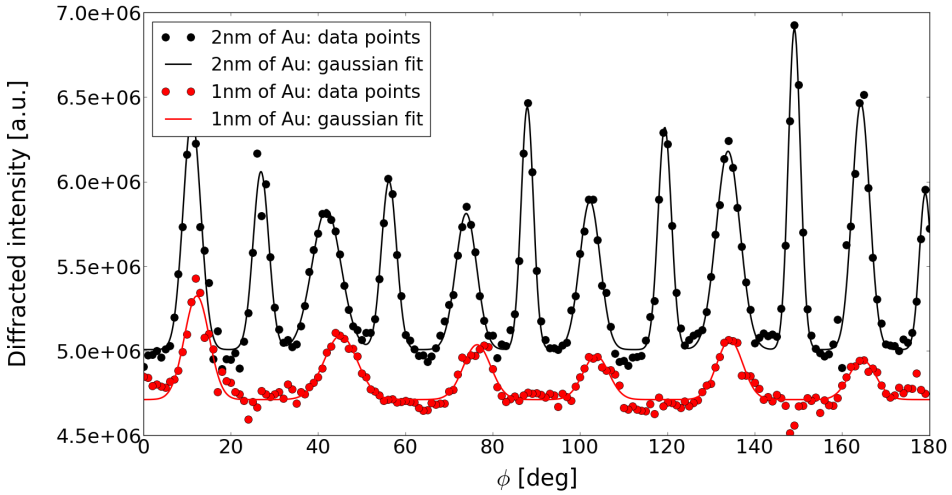

Figure 5.5: Diffracted intensity for $\gamma = 90°$ as a function of the ϕ angle for the samples with the two lowest initial Au layer thickness values. Each graph was obtained by plotting the intensity along the $\gamma = 90°$ vertical line of the corresponding intensity map of Figure 5.4.

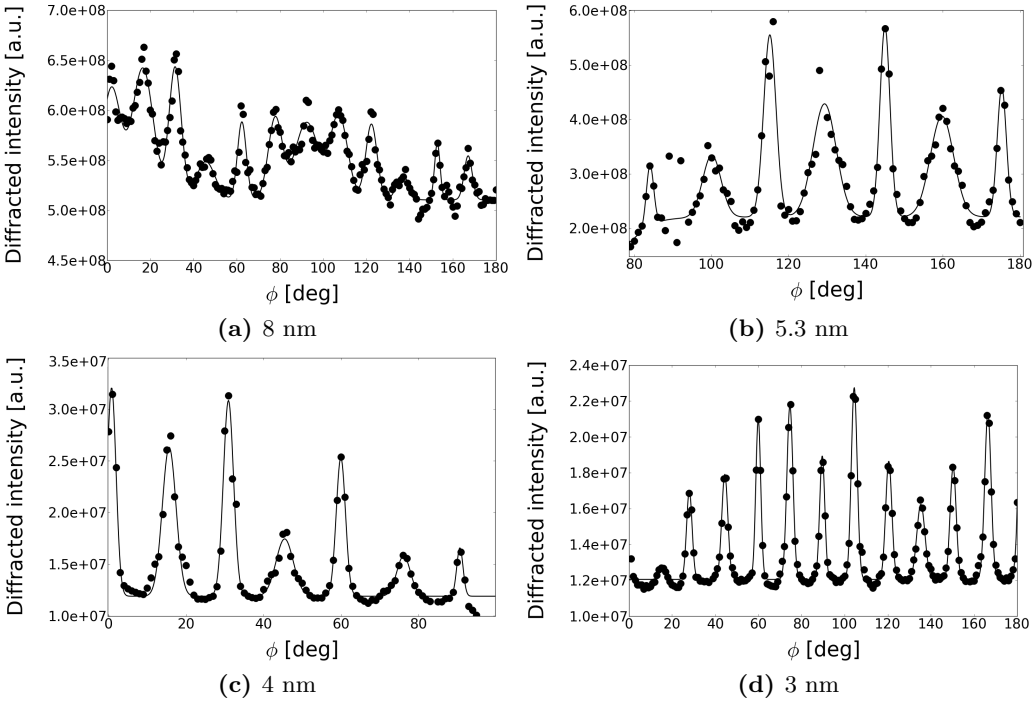

Figure 5.6: Diffracted intensity (• Data points and − Gaussian fit) as a function of the ϕ angle for samples with different initial Au layer thickness values. The graphs were obtained from the corresponding intensity maps as for Figure 5.5

of diffracted intensity show roughly the same periodicity varying the initial Au layer thickness from 8 nm down to 2 nm. An abrupt change seems to occur for the sample with 1 nm of Au, whose corresponding plot is shown in Figure 5.5 together with the 2 nm one for comparison: from the figure is clearly evident how the number of peaks for 1 nm of Au is halved with respect to the 2 nm case, one peak every two being missing. This feature was already evident through a simple inspection of the intensity maps of Figure 5.4. By fitting the data points with a train of gaussian curves, it has been possible to extract the peak-to-peak distance and thus to obtain a precise evaluation of the peaks periodicity. As immediately expected after a quick glance to the plots, the periodicity turns out to be practically identical for all the samples between 8 and 2 nm of Au, for which a value around 15° is obtained. On the contrary, the sample with 1 nm of Au diplays a double periodicity, with a peak-to-peak distance of about 30°. These results are summarized in the plot of Figure 5.7.

An evaluation of expression (5.1) leads to the conclusion that the presence of equally spaced peaks with a periodicity of 15° in the ϕ scans can be accounted for by two different scenarios. The first one implies the presence of a single nanoparticles preferred in-plane orientation, characterized by $\beta_{111} = 7.5°$: this value would give rise to the sequence of peaks positions 7.5°, 22.5°, 37.5°, ... The second one, on the other hand, requires two families of Au nanoparticles to be present, one with $\beta_{111} = 0°$ and the other with $\beta_{111} = 45°$ (or, equivalently, $\beta_{111} = 15°$). Each of these two orientations corresponds to one of the two degenerate cases mentioned in the previous section and hence produce a 30° peaks periodicity: since the peaks positions are shifted by 15° in the two cases, the observed 15° peak-to-peak

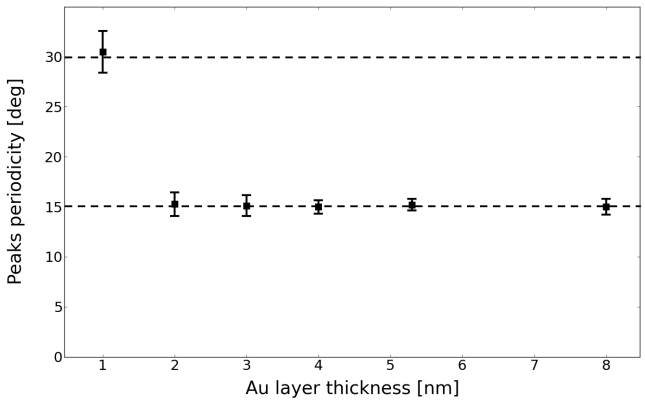

Figure 5.7: Periodicity of the peaks shown in Figure 5.5 and 5.6.

distance results. The sequence of values would be in this case 0°, 15°, 30°, ... The only difference between the two scenarios is a shift of 7.5° in the absolute peaks positions of the ϕ scans. Owing to the uncertainty in the sample mounting offset highlighted at the end of Section 3.2, a conclusive distinction between the two cases could not be made using the data of the area detector experiment. Nevertheless, given the estimation of the unknown offset carried out through the substrate peaks, the measured values of the ϕ scans peaks seem much more consistent with the sequence of values 0°, 15°, 30°, ... The two families picture thus appears to be more likely. This seems to be further suggested by the different peak shape observed for the 30°, 60°, 90°, ... and the 15°, 45°, 75°, ... peak series in Figure 5.5 for the 2 nm sample. The former appear to be sharper than the latter, thus resulting in a narrow-peak / broad-peak sequence. This feature (present also in the plots of Figure 5.6, even if less noticeably) was subsequently confirmed by the data collected with the diffractometer (see Figure 5.9)

In order to directly measure the in-plane orientation of the gold nanoparticle with respect to the STO substrate, a second experiment was carried out on the ID06 diffractometer. The graph obtained by the collected data is shown in Figure 5.8. Here the β angle (as defined in Section 2.3.2) univocally identifies the in-plane reciprocal lattice vector orientation with respect to the STO(100) direction (as discussed with respect to Figure 5.3a). Its role is the same hold by the ϕ angle of Figures 5.5 and 5.6. Each point of the plot was derived integrating, over a rocking scan of the sample, the diffracted intensity coming from the Au{331} lattice planes with different in-plane orientations (that is to say different β values). For the Au thicknesses probed, clear peaks are present around 0° and ±15°. Since the periodicity of the Au{331} and Au {220} reciprocal lattice points is the same (see Figure 5.2a), the values sequence 0°, 15°, 30°, ... is confirmed, thus ruling out the possibility of only one nanoparticles family with $\beta_{111} = 7.5°$. Nontheless it has to be noticed that deviations of the order of 1° from the exact $\beta = 0°$ and $\beta = \pm 15°$ positions seem to be present. The measurements performed using the diffractometer can theoretically guarantee a resolution much lower than 1°, thus leading to regard this small deviation as a real feature of the samples. Anyway, since they do not appear to follow a regular scheme, further investigation would be probably necessary to completely rule out the possibility of an experimental error.

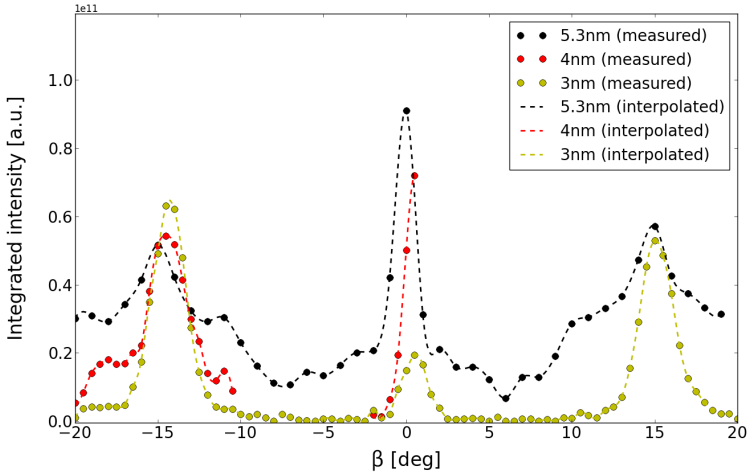

Figure 5.8: $(001)_{STO}$ || $(111)_{Au}$ nanoparticles Au{331} diffracted intensity for different values of the initial Au layer thickness. The measured points refer to the diffracted intensity integrated over a diffractometer rocking scan for Au{331} reflections with different in-plane orientations (different β values). The dashed lines are meant just to help displaying the trend. The red data-set could not be completed ($\beta \leq 1°$).

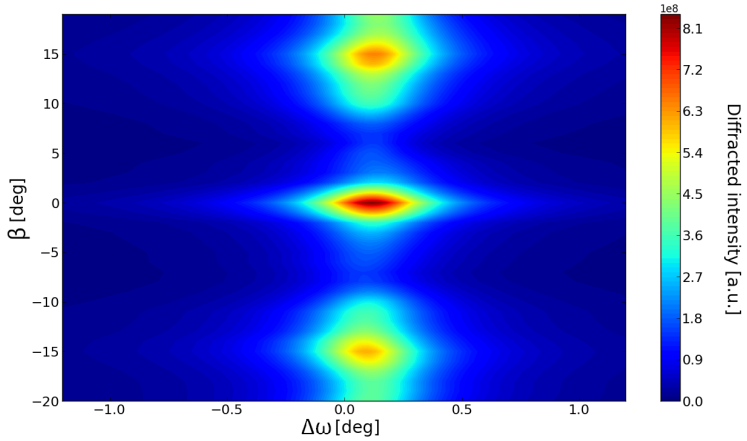

Figure 5.9: Au{331} diffractometer rocking scans for different $(001)_{STO}$ || $(111)_{Au}$ nanoparticles in-plane orientations for the 5.3 nm sample. The corresponding integrated intensity along the ω direction is shown in Figure 5.8.

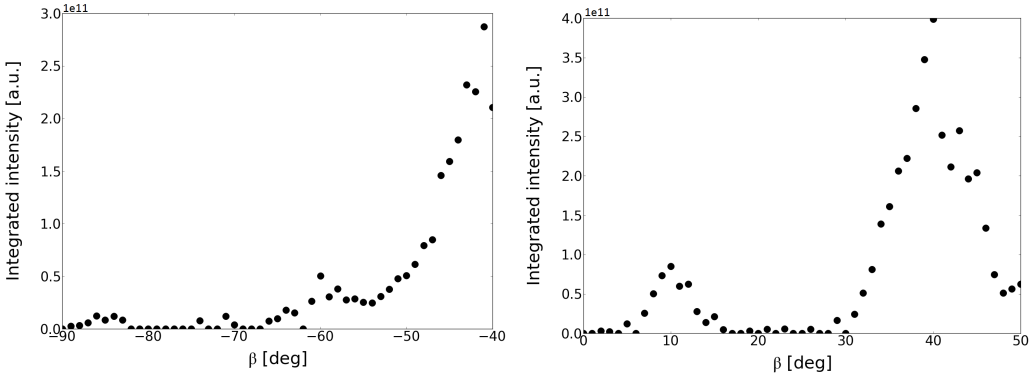

(a) 1.5 nm **(b)** 1 nm

Figure 5.10: $(001)_{STO} \,||\, (111)_{Au}$ nanoparticles Au{331} diffracted intensity for values of the initial Au layer thickness smaller than 2nm. The data points refer to the diffracted intensity integrated over a diffractometer rocking scan, analogously to those shown in Figure 5.8.

The above conclusion would immediately lead to interpret the double periodicity observed for the 1 nm sample as a direct result of the disappearance of one of the two different nanoparticles in-plane orientations. Looking at the peaks position in Figure 5.5, the family which seems to be absent in the sample with 1 nm of Au is the one characterized by $\beta_{111} = 0°$. The peaks sequence observed is indeed very close to $15°, 45°, 75°, \ldots$, produced by $\beta_{111} = 15°$. This seems to be elegantly predicted by the variation in the peaks intensity originating from the two families as the initial Au layer thickness is decreased. This is evident in the plot of Figure 5.8. As can be clearly seen, the intensity of the central peak drops as the Au thickness decreases: while it is the dominant peak for 5.3 nm of Au, in the 3 nm sample the intensity associated with the $\pm 15°$ peaks becomes much greater. This trend leads to infer that further lowering of the Au layer thickness would lead to the total suppression of the central peak in favor of the other two. Unfortunately the diffraction data collected with the diffractometer for the 1 nm sample (Figure 5.10b) could not provide a completely convincing confirmation of the conclusions mentioned above. If, in fact, the 30° periodicity seems to be confirmed, the absolute peaks positions are not the ones expected, here being equal to 10° and 40°. These values would arise from a value of β_{111} equal to 10° or 20°: however, if this was the case, a peak in correspondence of $\beta = 20°$ should be also present (this follows from equation (5.1)). Furthermore, the diffraction data of the 1.5 nm samples (Figure 5.10a) looks even less convincing, displaying only one clear peak at $-40°$. Nevertheless, great attention has to be payed in interpreting the diffractometer data for these two latter Au thicknesses. Owing to the low amount of Au present (and considering the problems in choosing the beam energy outlined in Section 3.3), the diffracted intensity coming from these samples was very low. As a consequence, the aspect of the plots of Figure 5.10 is strongly dependent on the parameters used to fit the rocking scans data: the final trend obtained is then much less reliable than for greater Au thicknesses. Another important aspect to stress the attention on is the lack of a strict $(001)_{STO} \,||\, (111)_{Au}$ crystallographic orientation for the 1 and 1.5 nm samples (as shown in Figure 4.11): therefore the observed trend in the in-plane investigation plots may somehow arise from the lobes of the cross-like feature measured. Given the previous

considerations, the presence of only the $\beta_{111} = 45°$ family for the 1 nm sample appears to be the most consistent scenario considering the whole set of data collected. The intermediate case of 1.5 nm needs further investigation since only the diffractometer data are available. It is also worth noticing that this latter sample belongs to a distinct set of samples, grown by a different operator after all the others: variations between one set of samples and another may also be taken into account.

The existence of two different in-plane orientations was quite unexpected at the time the measurements were performed. Since the cubic {110} and {100} reciprocal lattice directions are not equivalent, one would expect the two in-plane configurations, $\beta_{111} = 0°$ and $\beta_{111} = 45°$, to produce two different values for the Au/STO interface energy: the nanoparticles were then expected to choose the one corresponding to the minimum value. Apparently the energy difference between the two configurations is small enough for both of them to be present with an initial Au layer thickness greater than 2 nm. Anyway this result is consistent with the epitaxial orientations of Au islands on a $SrTiO_3(001)$ - (2 x 1) surface found by Silly and Castell [46]: in particular, the cases $\beta_{111} = 0°$ and $\beta_{111} = 45°$ corresponds to the second and the first of relations (2.17) respectively. As already noticed in reference to Figure 5.5, the fact that the peaks at 0° and ±15° arise from two distinct families, each one with its own crystallographic properties, is confirmed by their different appearance. With respect to Figure 5.8, as well as the peaks maximum value (already discussed), the shape looks clearly different, with the peak at 0° being generally sharper. The shape difference can be particularly well appreciated in the contour plot of Figure 5.9, relative to the 5.3 nm sample. The plot represents by means of a colormap, the diffracted intensity over rocking scans (that is to say scans of the ω angle, as defined in Figure 3.7b) performed for different values of the nanoparticle in-plane orientation. The peaks at ±15° are much broader along the β axis, while having a slightly smaller extension along the ω one. The 5.3 nm graph of Figure 5.8 is simply obtained through an integration along the ω direction.

Moreover, as mentioned before, Figure 5.8 seems to suggest that the energy associated with each one of the two in-plane configurations depends on the initial Au layer thickness. The $\beta_{111} = 0°$ family appears to be related to an energy term which increases as the thickness value decreases. At low thicknesses value this energy term is high enough to cause the disappearance of the corresponding in-plane orientation, as shown by the double periodicity of the red plot of Figure 5.5. This dependence of the Au nanoparticles crystalline preferred orientation on the initial Au layer thickness was even more unexpected than the presence of two different in-plane orientations itself. In literature several works can be found dealing with the crystalline properties thickness dependence of various thin film systems. However they mainly regards the investigation of the crystal defects (for instance [35] and [41]) or the disappearance of crystalline order above a certain thickness threshold value (for instance [14] and [15]). As far as the author knows, there are no documented cases of crystal orientations modifications depending on the thin film thickness, least of all for embedded nanoparticles as the ones considered in the present work.

A very interesting aspect is represented by the role of the STO thin film in the nanoparticles in-plane orientation. In this regard, the plot of Figure 5.11 shows how the same

15°-periodical in-plane orientation angles sequence is also present for the sample without the STO thin film and an initial Au layer thickness of 5 nm. Furthermore the peak shape in the contour plot of Figure 5.12 exhibit similar features to the 5.3 nm sample with STO top layer previously pointed out. As for the preferred nanoparticles vertical growth orientation (see Section 4.2), the nanoparticles in-plane orientation seems to directly derive (at least for a Au thickness about 5 nm) from that of the Au 3D islands. However, since only one sample without the STO top layer was available at the time the measurements were performed, a systematic study about its influence on the nanoparticles orientation was not possible. The

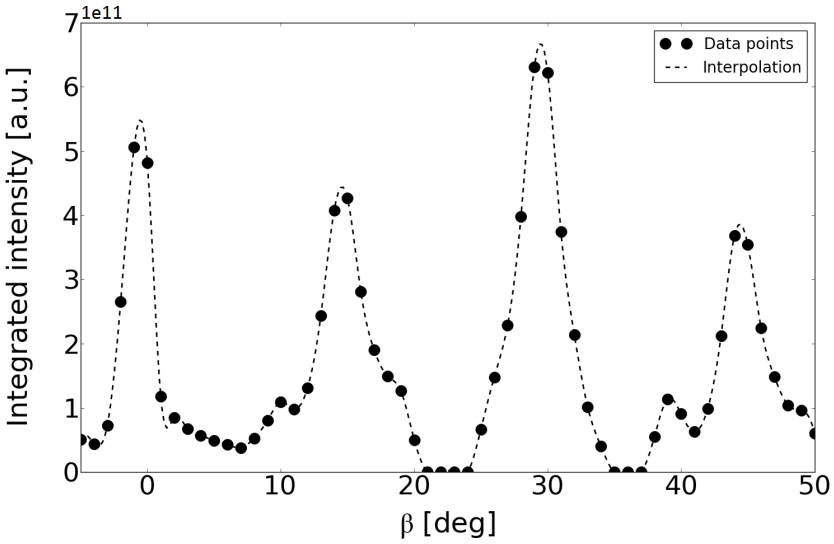

Figure 5.11: $(001)_{STO}$ || $(111)_{Au}$ 3D islands Au{331} diffracted intensity for the sample without STO thin film (5 nm of Au). The measured points refer to the diffracted intensity integrated over a diffractometer rocking scan, as for the previous plots. The dashed line is meant just to help displaying the trend.

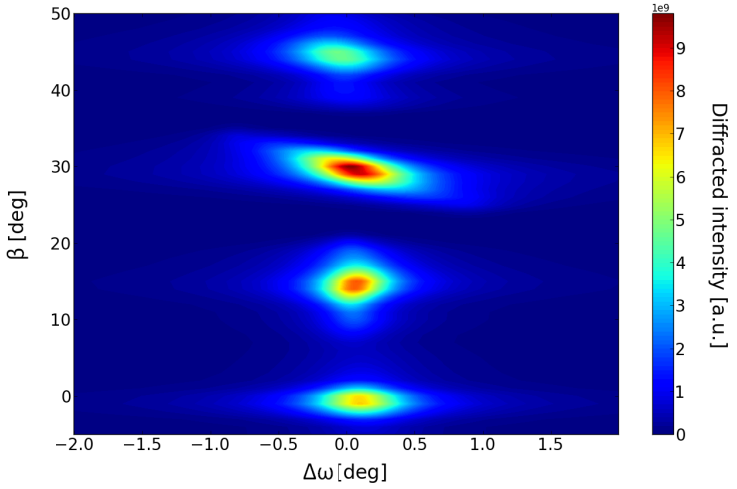

Figure 5.12: Au{331} diffractometer rocking scans for different $(001)_{STO}$ || $(111)_{Au}$ 3D islands in-plane orientations for the sample without STO top layer (5 nm of Au). The corresponding integrated intensity is shown in Figure 5.11

intensity drop of the $\beta_{111} = 0°$ peak in Figure 5.8 and the disappearance of the corresponding nanoparticles family (as displayed in Figure 5.5) pave the way to two different possibilities:

- The first one considers the presence of the same features observed in the Au nanoparticles diffraction pattern for the corresponding sample (same initial Au layer thickness) without STO top layer. In this case the nanoparticles in-plane orientation would be completely determined by the Au 3D islands / $SrTiO_3(001)$ interface: the STO thin film would thus have no influence on the Au preferred crystalline orientations.
- The second one considers the possibility to observe the same pattern of Figure 5.11 for the samples without STO top layer at any values of Au layer thickness. In this case the measured differences between one nanoparticle sample and another would be due to the peculiar Au/STO interactions induced by the presence of the thin film.

With the data available up to now it is impossible to definitely claim which one of the two is the correct one. However, considering the lack of documented crystallographic orientations thickness dependences in traditional layered samples, a role of the overgrown thin film is likely to be supposed. The presence of the STO secondary phases for the 5.3 and 8 nm samples (see Section 4.2) seems not to be related with the disapparance of one of the two in-plane orientations (which occur at lower Au thicknesses) and in general seems not to have a direct impact on the nanoparticles orientation.

As mentioned in Section 4.2, increasing the amount of Au deposited on the substrate seems to lead to an increased degree of disorder in the Au/STO crystallographic relations. This is quite evident for the 8 nm sample both in Figures 5.6a and 5.15a, where the diffraction peaks exhibit a more noisy trend or are almost invisible respectively. The previous consideration about the presence of an increased disordered can be somehow extended to all the Au layer thicknesses probed. Going from 1 to 8 nm indeed implies first the increase in the number of measured in-plane orientations from 1 to 2 (in between 1 and 2 nm of Au) and then the loosening of strictly defined Au/STO relative crystallographic relations (around 8 nm). The presence of a completely random (isotropic) in-plane nanoparticles orientation might be predicted for even greater Au thicknesses. It is finally worth noticing that the aforementioned increasing disorder is somehow consistent with the increasing amount of Au to be accommodated inside the STO matrix as the Au layer thickness is increased.

5.2.2 $(001)_{STO} \,||\, (002)_{Au}$ nanoparticles in-plane orientation

The ϕ scans performed for the in-plane investigation can be effectively displayed using pole figures. Starting from the intensity maps of Figure 5.4, the pole figures of Figure 5.14 were obtained. Their aspect can be easily interpreted by comparison with the corresponding simulated ones, shown in Figure 5.13c. The simulation was carried out considering the presence of the two $(001)_{STO} \,||\, (111)_{Au}$ families, namely the $\beta_{111} = 0°$ and $\beta_{111} = 45°$ one. In addition it takes into account the presence of the $(001)_{STO} \,||\, (002)_{Au}$ nanoparticles: for the latter family, β_{002} values equal to 0° and 45° were supposed, consistently with the epitaxial relations 2.16 already documented in literature. As clearly shown by the simulation, the series of peaks at $\chi = 35.26°$ (as defined in Figure 2.13b) arises from the $(001)_{STO} \,||\, (111)_{Au}$

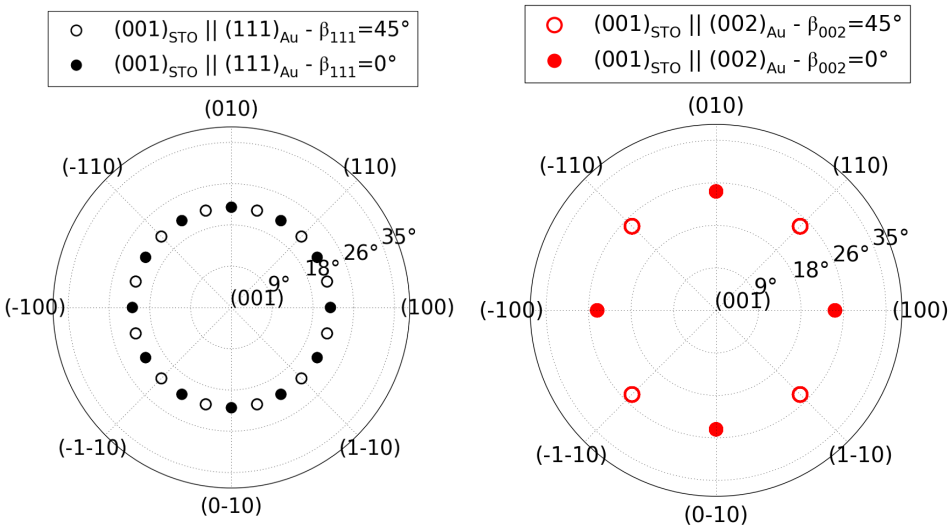

(a) Au{331} **(b)** Au{311}

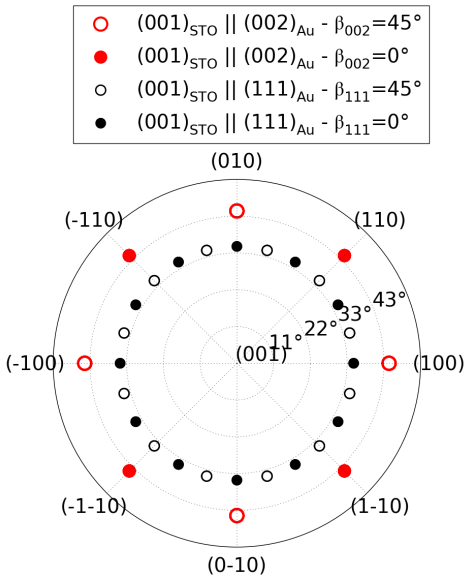

(c) Au{220}

Figure 5.13: Simulated pole figures for different Au reflections used for the in-plane investigation. For the Au{220} one, both the $(001)_{STO} \,||\, (002)_{Au}$ and the $(001)_{STO} \,||\, (111)_{Au}$ families of nanoparticles have been considered: for each one of them two different in-plane orientation values (0° and 45°) have been taken into account. For the Au{331} and Au{311} ones, only one of the two families is displayed (the one whose corresponding in-plane orientation whose probed using the considered reflection).

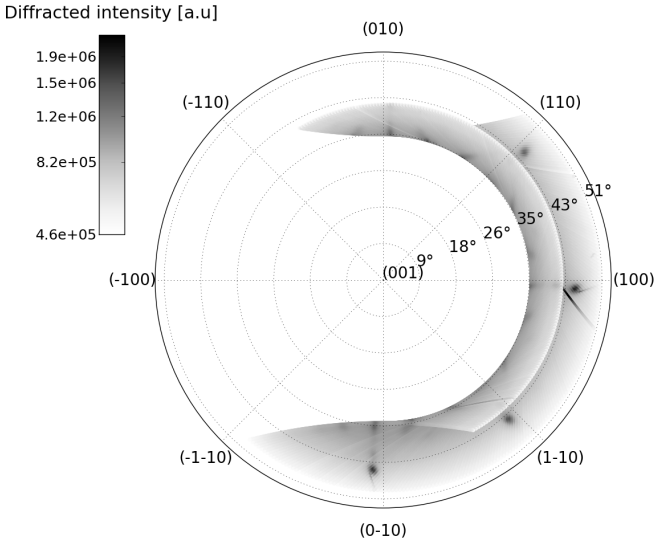

(a) 2 nm

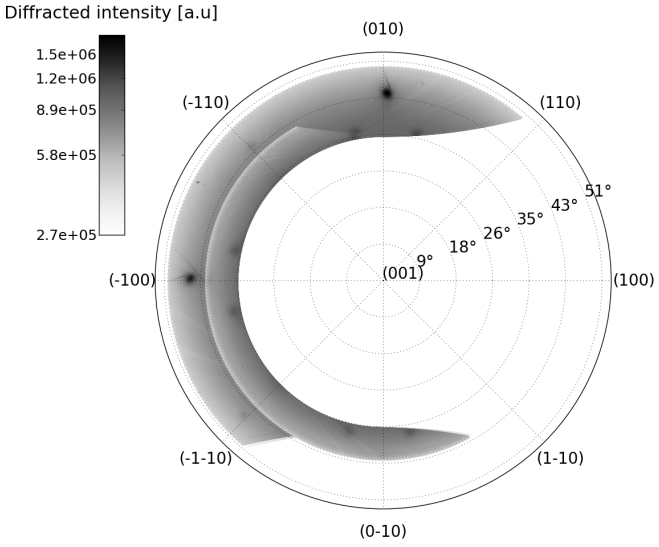

(b) 1 nm

Figure 5.14: Au{220} pole figures for the samples with the two lowest initial Au layer thickness values.

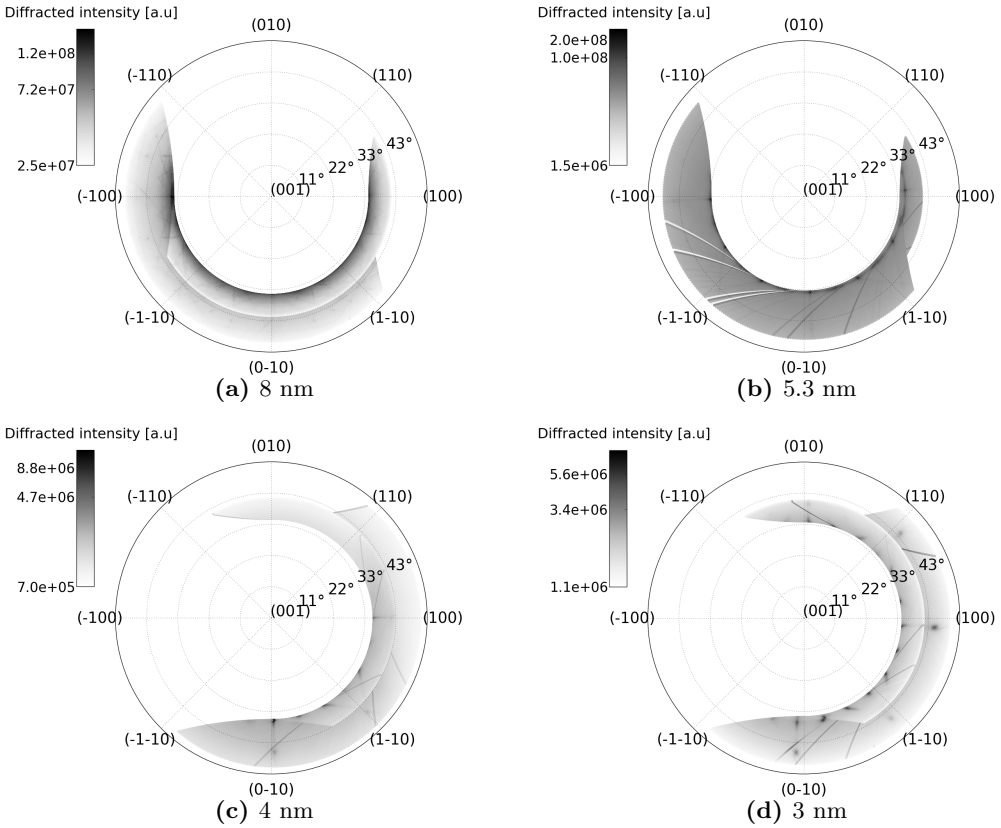

(a) 8 nm **(b)** 5.3 nm

(c) 4 nm **(d)** 3 nm

Figure 5.15: Au{220} pole figures for samples with different initial Au layer thickness values.

nanoparticles. From the pole figures of Figure 5.14 is evident the absence, for the 1 nm case, of the spots represented through black full circles in the simulation, as a direct consequence of the missing $\beta_{111} = 0°$ family. All the peaks are instead present for the sample with 2 nm of Au (and for greater thicknesses, as displayed in Figure 5.15). An inspection of the pole figures also reveals the existence of different $(001)_{STO} \,||\, (111)_{Au}$ nanoparticles spot shapes for a Au thickness greater than 2 nm: roughly round shaped spots are spaced out by couples of oppositely elongated ones. On the other hand, the same roughly round shape is exhibited by the spots of the 1 nm sample. Further work is needed to understand if this aspect is merely an artifact produced by the data analysis or otherwise it is related to a physically interesting aspect about the samples. Anyway, the most interesting features shown by the pole figures lies in the presence of additional peaks, located at $\chi \approx 45°$ along the {100} and {110} substrate directions. These peaks (which are the same that can be seen for $\gamma \approx 60°$ in Figure 5.4) derived from the $(001)_{STO} \,||\, (002)_{Au}$ nanoparticles, as shown by the simulation. They are not visible for the samples with 8, 5.3 and 4 nm of Au. However it is very likely that this is simply due to a small misalignment of the samples, which prevents the Bragg condition for these reflections to be fully satisfied. The ϕ scans which the pole figures derived from were indeed conceived to look only at the $(001)_{STO} \,||\, (111)_{Au}$ nanoparticles. The existence of the other family was not known and the measurements were not consequently optimized for the corresponding reflections. Although this problem makes a precise evaluation of the spots intensity actually impossible, preliminary indications can be extracted anyway.

From the inspection of the pole figures, a substantial difference between the 1 nm sample and the other ones with visible $(001)_{STO} \,||\, (002)_{Au}$ peaks emerges. In the samples with 2 and 3 nm of Au the intensity of such peaks seems roughly equally distributed between the two families ($\beta_{002} = 0°$ and $\beta_{002} = 45°$). On the contrary, in the 1 nm sample the peaks along the {100} directions ($\beta = 0°, 90°, \ldots$) displays a much greater intensity with respect to the others ($\beta = 45°, 135°, \ldots$). This in turn suggests that the $\beta_{002} = 45°$ occurs more frequently than the other one. As will be pointed out hereafter, this is confirmed by the diffraction data collected with the diffractometer and shown in the form of contour plots in Figure 5.16. These graphs are analogous to the ones already used with respect to the peaks originating from the $(001)_{STO} \,||\, (111)_{Au}$ nanoparticles. The only difference is that in this case (a part from the 5.3 nm sample), in the x axis is reported the reciprocal vector component along the (100) substrate direction rather than the rocking angle. The diffracted intensity displayed is in this case the one of the Au{311} diffration peaks coming from the $(001)_{STO} \,||\, (002)_{Au}$ nanoparticles. As before, the β angle identifies the in-plane orientation of such peaks. For each initial Au thickness the regions around $\beta = 0°$ and $\beta = 45°$ (or equivalently $\beta = -45°$) are shown. In comparing these contour plots with the Au{220} pole figures reported before, one has to bear in mind the observation already done in the previous section referring to Figure 5.2b: for a fixed value of β_{002}, the Au{220} equivalent diffraction peaks are shifted with respect to the Au{311} by an angle of 45°. This is clear comparing the simulated pole figures of Figures 5.13b and 5.13c.

Consistently to what previously observed, for the 1 nm sample the intensity associated to the $\beta_{002} = 45°$ family (which produces Au{311} diffraction peaks at $\beta = \pm 45°$) is much

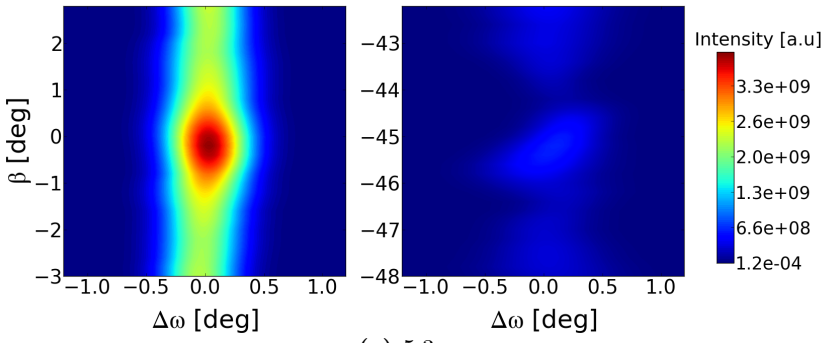

(a) 5.3 nm

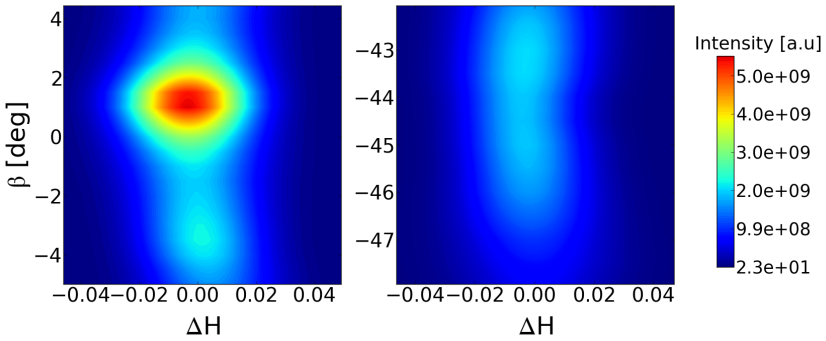

(b) 4 nm

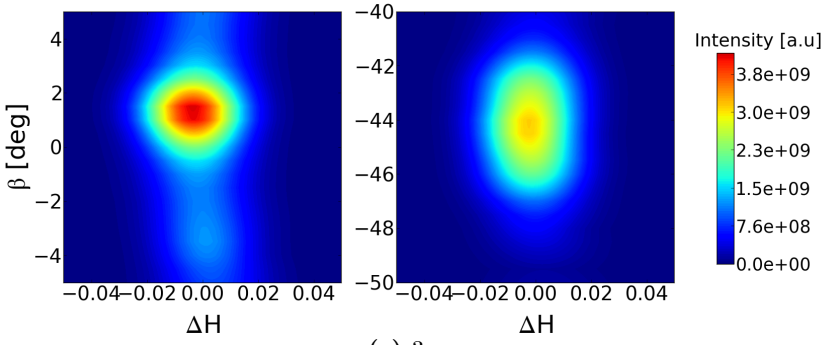

(c) 3 nm

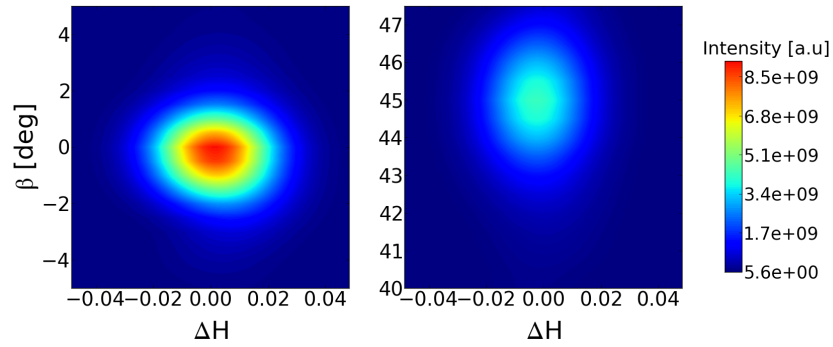

(d) 1.5 nm

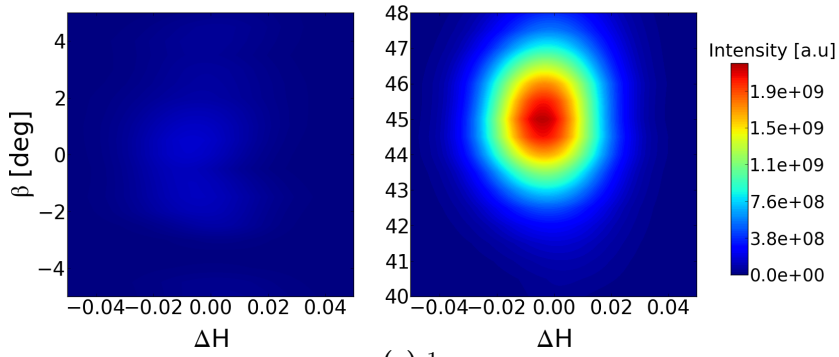

(e) 1 nm

Figure 5.16: Au{311} diffractometer rocking scans for different $(001)_{STO} \,||\, (002)_{Au}$ nanoparticles in-plane orientations (β values) around $\beta = 0°$ (left) and $\beta = 45°$ (right). The data refers to samples with different values of the initial Au layer thickness: the left and the right plot of each thickness share the same colorscale to allow a direct comparison.

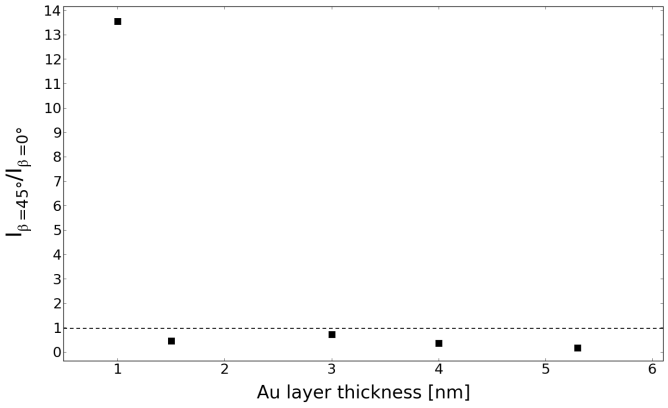

Figure 5.17: Diffracted intensity ratio between the Au{311} peaks at $\beta = 45°$ and the same peaks at $\beta = 0°$ for different initial Au layer thicknesses. The ratio provides an indication about the relative abundance of the $\beta_{002} = 45°$ family with respect to the $\beta_{002} = 0°$ one. The values used to calculate the ratio are the maximum intensity values obtained from the plots of Figure 5.16.

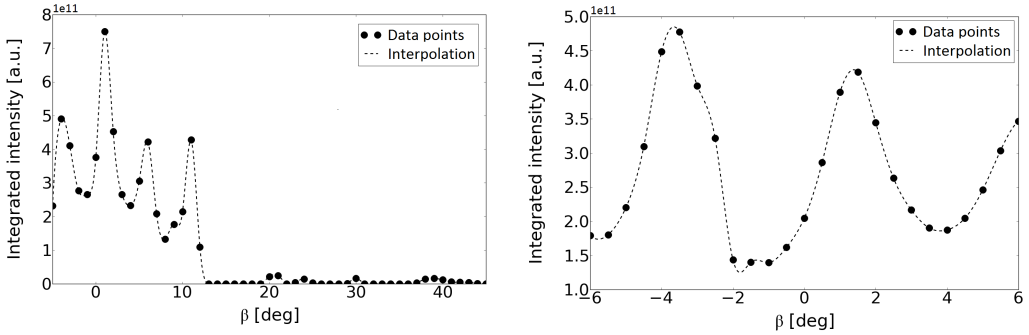

(a) Scan over a wide in-plane range

(b) Finer scan around $\beta = 0°$

Figure 5.18: $(001)_{STO}$ || $(002)_{Au}$ 3D islands Au{311} diffracted intensity for the sample without STO thin film (5 nm of Au). The measured points refer to the diffracted intensity integrated over a diffractometer rocking scan, as for the previous plots. The dashed line is meant just to help displaying the trend.

higher than the one associated to the $\beta_{002} = 0°$ one. The peak at $\beta = 0°$ is actually almost absent. On the other hand, thicker Au layers induce the opposite situation, the peak at 0° being more intense than the 45° one. The ratio between the maximum intensity values of the two peaks as a function of the Au layer thickness is systematically shown in Figure 5.17. For all but the 1 nm sample this ratio is smaller than one, indicating a more abundant presence of the $\beta_{002} = 0°$ family. The data points exhibit a monotonically decreasing trend from 3 nm onward. The value of about 0.7 calculated for the 3 nm sample (the closest to unity) is consistent with an almost equally distributed intensity observed in the corresponding pole figure spots. As for the $(001)_{STO}$ || $(111)_{Au}$ nanoparticles in-plane orientation, the 1 nm sample shows substantially different features from all the others. The ratio is in this case much bigger than 1 and the difference in the two families population is the greatest observed, the $\beta_{002} = 0°$ being practically absent. It is worthwile pointing out that, as previously observed for the $(001)_{STO}$ || $(111)_{Au}$ nanoparticles, small deviations from the exact $\beta = 0°$ and $\beta = \pm 45°$ positions seem to occur. Also in this case, further investigation is needed to rule out the possibility of an experimental error.

As already done for the $(001)_{STO}$ || $(111)_{Au}$ nanoparticles, it is interesting to compare the crystallographic features of the nanoparticles with those of the 3D islands in the sample without STO thin film. Only one sample was available in this case too, thus making once again a systematic comparison impossible. For this sample the preferred in-plane orientation of the Au islands seems to be located around $\beta = 0$. However, contrary to what observed for the Au nanoparticles, in the case of the 3D islands multiple peaks are present in the probed $(-6°, 10°)$ interval (Figures 5.18 and 5.19). The STO thin film thus seems somehow to force only one of the in-plane orientations present prior to its deposition to occur for the embedded nanoparticles. It is interesting how none of these peaks is exactly centered at $\beta = 0°$: the closest one occurs at a β value between 1° and 2° (Figure 5.18b). This evidence might be related to the deviations observed for the nanoparticles peaks mentioned above. Moreover, no peak seems to be present around $\beta = 45°$. This constitutes a difference with respect to the case of the nanoparticles, since a peak at the latter in-plane orientation is

always observed, even if with a lower intensity as compared to the 0° one. A more active role of the STO layer in the determination of the preferred $(001)_{STO}$ || $(002)_{Au}$ nanoparticles crystalline orientation might thus be promoted with respect to the other family. It is also true that the absence of the 45° peak in the sample without STO thin film (and with 5 nm of Au) may also be regarded to be consistent with the relative low intensity of the 45° peak for the 5.3 nm sample with STO layer as compared to the other Au thickness. The increased $I_{\beta=45^\circ}/I_{\beta=0^\circ}$ ratio measured lowering the Au thickness down to 3 nm (Figure 5.17) could be consequently attributed to a similar trend occurring for the corresponding samples (same Au thickness) without STO top layer. Once again, samples without STO layer and with different Au thicknesses would be necessary to disentangled the contribution of the STO thin film and the Au thickness in determining the nanoparticles preferred orientation.

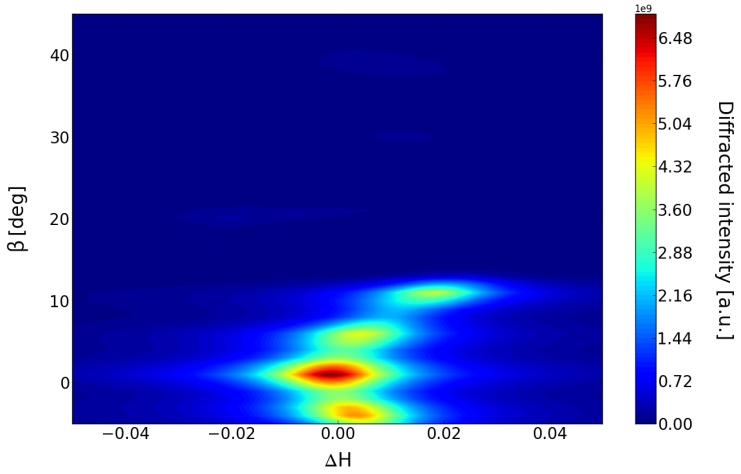

Figure 5.19: Au{311} rocking scans for different $(001)_{STO}$||$(002)_{Au}$ 3D islands in-plane orientations for the sample without STO top layer (5 nm of Au). The corresponding integrated intensity is shown in Figure 5.18a

Considering the body of the results obtained from the analysis of both the nanoparticles families, the most relevant aspect which stands out is the peculiarity of the 1 nm sample with respect to all the other. For both the $(001)_{STO}$ || $(111)_{Au}$ and the $(001)_{STO}$ || $(002)_{Au}$ nanoparticles in-plane orientation an abrupt change in the crystallographic properties is observed lowering the Au thickness to the value of 1 nm. On the other hand the samples with greater Au thickness values exhibit qualitatively equivalent crystallographic properties: quantitative differences in the diffracted intensity are nonetheless present. In this sense the measurements realized for both the families lead to the common conclusion that a transition in the samples texture properties occur between 1 and 2 nm of initial Au layer thickness. With respect to Figure 5.17 the sample with 1.5 nm of Au show properties which can be considered roughly equivalent to the one displayed by the sample with a greater Au thickness (a part from the deviation from the monotonically decreasing trend in the $I_{\beta=45^\circ}/I_{\beta=0^\circ}$ ratio observed for greater values as the thickness is increased). This would shift the transition position somewhere between 1 and 1.5 nm. The most important aspect to be clarified (which will require further investigation on additional samples) is represented by the factors involved

in the occurrence of such a transition. In particular the interplay in the roles of the STO thin film and the amount of deposited Au (that is to say the Au layer thickness) needs to be disentangled. An interesting aspect has been recently pointed out by the Scanning Electron Microscopy images of Figure 4.4. From these images a clear dependence of the Au 3D islands shape and distribution on the amount of deposited Au becomes visible. While between 3 and 5 nm of deposited Au the morphological properties of the islands resulting from the annealing process appear more or less equivalent, for the sample with 1 nm of Au an abrupt change occurs. It indeed exhibits a tendency to form a greater number of much smaller 3D islands with respect to the other thickness values. This abrupt change is consistent with the transition in the nanoparticles crystallographic orientation shown by the diffraction data of the corresponding STO-covered samples: a relation between structure and morphological properties thus seem to be present. A complete understanding of the nature of this relation will need further investigation.

Conclusions and future developments

Hard X-ray synchrotron diffraction was used to study the crystalline preferred orientation of gold nanoparticles embedded in a $SrTiO_3$ matrix. Metal nanoparticles systems are well suited to be used as plasmonic active materials, with proved potentialities as sensors in life sciences. The samples were kindly provided by the Institute of Solid State Physics of the Friedrich-Schiller-University in Jena, Germany. They were prepared by growing a $SrTiO_3$ thin film on a system composed by a Au dewetted layer deposited on a $SrTiO_3(001)$ single crystal substrate; magnetron sputtering and pulsed laser deposition were used for the Au and STO layer deposition respectively. This novel fabrication method presented allows the production of crystalline anisotropic nanoparticles with tunable size and shape without the necessity to recur to more complicated lithographic or chemical processes. Two separate X-ray experiments were performed on samples with different Au layer thickness values: the first one made use of a CCD area detector, while in the second a traditional point detector mounted on a single crystal diffractometer was exploited. Through these experiments, the following conclusions can be drawn:

- With respect to the vertical (normal to the substrate surface) nanoparticles growth orientations, two main families are present, one aligned along the (111) direction and the other along the (002). The (111) orientation appears to be not strictly present for the samples with 1 and 1.5 nm of Au layer thickness, for which additional orientations around the (111) were measured. For each vertical crystallographic direction, the orientation in the plane of the substrate surface was also investigated.

- For the (111)-oriented nanoparticles the two in-plane orientations $(001)_{SrTiO_3}||(111)_{Au}$, $[110]_{SrTiO_3}$ || $[110]_{Au}$ and $(001)_{SrTiO_3}$ || $(111)_{Au}$, $[100]_{SrTiO_3}$ || $[110]_{Au}$ were found for the samples with an initial Au layer thickness greater or qual to 2 nm, in accordance with what documented in literature for a similar system [46]. For the (002)-oriented nanoparticles the two in-plane orientations reported in literature for the (001) heteroepitaxy of FCC metals on $SrTiO_3(001)$ substrates were found for the same range of thicknesses: they are, namely, $(001)_{SrTiO_3}$ || $(002)_{Au}$, $[100]_{SrTiO_3}$ || $[100]_{Au}$ and $(001)_{SrTiO_3}$ || $(002)_{Au}$, $[100]_{SrTiO_3}$ || $[110]_{Au}$.

- The nanoparticles crystalline preferred orientations seem to be strongly influenced by

the one observed in the Au 3D islands present on the substrate surface prior to the STO thin film growth. Strong evidences of a transition in the nanoparticles crystalline preferred orientation occurring between 1 and 2 nm of Au layer thickness were found. For the 1 nm sample, it causes the $(001)_{SrTiO_3} \,||\, (111)_{Au}$, $[100]_{SrTiO_3} \,||\, [110]_{Au}$ to apparently disappear and the relative abundance of the $(001)_{SrTiO_3} \,||\, (001)_{Au}$, $[100]_{SrTiO_3} \,||\, [110]_{Au}$ orientation to abruptly decrease with respect to the $(001)_{SrTiO_3} \,||\, (001)_{Au}$, $[100]_{SrTiO_3} \,||\, [100]_{Au}$ one. An undocumented layer thickness dependance of the Au crystalline preferred orientations has been thus pointed out.

- Modifications of the STO thin film crystal structure were also observed for the samples with 5.3 and 8 nm of Au: an actually polycrystalline film was obtained for these thickness values, with grains oriented with the {110} and {111} direction normal to the substrate surface. Structural modifications induced by the nanoparticles or the preexisting 3D islands (which are larger for the greatest Au thickness values probed) may be considered as a possible explanation.

The nature of the Au nanoparticles orientation dependance on the amount of deposited Au and the consequent transition observed has still to be clarified. This will require a deeper investigation of the samples with a low Au layer thickness, particularly in the region between 1 and 2 nm, for which the low diffracted signal intensity constituted the main obstacle to a complete understanding of their properties. Furthermore, the role of the STO thin film in the nanoparticles crystallographic orientations will have to be elucidated. For this purpose the preparation of additional samples without the STO top layer, one for each value of the Au layer thickness probed, might be necessary. A characterization of the substrate surface could also lead to a deeper understanding of the interface phenomena involved in the sample growth process. In this regard, an investigation of the bulk terminations actually present and of possible reconstructions (and/or changes in the stoichiometry) occurring on the surface might be valuable.

Finally, as a future subject of study, an investigation of the possible presence of a macroscopic and/or microscopic strain for both the Au nanoparticles and the STO grains could provide further information on the growth process involved in the nanoparticles formation. Furthermore, since the plasmonic properties of metal nanoparticles are strongly influenced by their shape and size, a further size-broadening analysis of the XRD peaks for different crystallographic directions could be of great interest.

Appendix A

Overview of synchrotron radiation properties

The first observation of synchrotron radiation came on 24 April 1947, at the General Electric Research Laboratory in Schenectady, New York. Ironically, synchrotron radiation was intially considered as an unwanted loss of energy in accelerators designed to produce intense beams of X-rays by directing accelerated electrons onto a suitable target. The potentialities of synchrotron radiation were later understood by Tomboulian and Hartman [51]. Five years later, in 1961, the first synchrotron radiation facility, the Synchrotron Ultraviolet Radiation Facility (SURF I), became operative in the Washington, D.C. labs of the National Bureau of Standards. Nowadays, synchrotrons are well established X-ray (and UV) radiation sources and several synchrotron radiation facilities all over the world (e.g. ESRF, Figure A.1) are available for a large number of external users. The properties of synchrotron radiation make it a powerful tool of investigation in many different fields of science, ranging from biology to solid state physics.

Figure A.1: Aerial view of the European Synchrotron Radiation Facility (ESRF), Grenoble (FR) [22].

A synchrotron is a charged particles, usually electrons, accelerator consisting of arched

sections, containing bending magnets (BM), alternated to straight sections used for insertion devices (ID), which generate the most intense synchrotron radiation, as shown in Figure A.2. The deflection field provided by the bending magnets forces the charged particles to describe a closed trajectory at relativistic energies (6 GeV for the ESRF). Such relativistic accelerated particles emit electromagnetic radiation with features depending both on the angular frequency of rotation of the particles and their energy E; this is given by $E[GeV] = \gamma/1957$, where $\gamma = 1/\sqrt{1-(v/c)^2}$ is the so called Lorentz factor (being v the speed of the charged particles). The beamlines run off along the axes of the insertion devices or tangentially at bending magnets (also used to produce synchrotron radiation): they contain the experimental setup for the sample investigation as well as all the instrumentation needed for the beam conditioning. For further details about the components of synchrotron facilities and the radiation emission process the reader should refer to the dedicated literature (Willmott [57]).

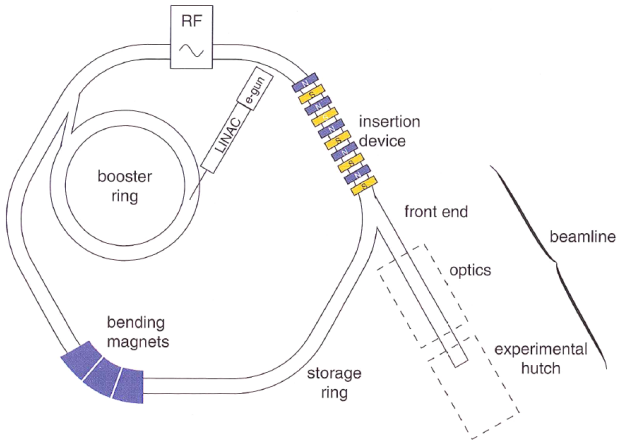

Figure A.2: Schematic of the main components of a modern synchrotron source [57].

The main reason why synchrotrons have become such important research tools is the extremely high brilliance as compared to traditional laboratory sources. Brilliance is a physical quantity which describes how the photon flux (number of photons per second per unit bandwidth, conventionally 0.1%) is distributed in space and angular range. It is defined as

$$\text{Brilliance} = \frac{\text{photons/second}}{(\text{mrad})^2(\text{mm}^2 \text{ source area})(0.1\% \text{ bandwidth})}$$

The brilliance of a third generation undulator is about 10^{20} photons/s/mrad^2/mm^2/0.1% bandwidth, some ten order of magnitude higher than that of a rotating anode Cu Kα line. The reason for such a high brilliance mainly lies on the enormous amount of light emitted by the accelerated charges, normally electrons. It is possible to demonstrate (see Willmott [57] for a more detailed discussion) that a flux emitted by an electron is proportional to γ^4, which increases as the speed of the electron increases. Since in a synchrotron the charges travel at a speed close to the speed of light, the flux of the emitted radiation is accordingly very high. Another reason for the high brilliance is the low emittance of the beam. The emittance is defined as the product of the linear source size and the beam divergence in the same

plane. The source size is primarily determined by the transverse size of the electron beam: generally it is of the order of microns. Furthermore the angular divergence is kept small by the relativistic speed of the electrons, which implies that the radiation is emitted in a narrow cone tangential to their curved trajectory. This results in an intrinsically collimated beam. The emittance has a lower fundamental limit deriving from the Heisenberg's uncertainty principle, namely $\epsilon_{min} = \lambda/(4\pi)$. In practice the emittance will always be higher than this value.

Another attractive properties of synchrotron radiation is the high degree of coherence, which cannot be achieved by traditional laboratory sources. Coherence can be phenomenologically defined as the property that enables a wave to produce visible diffraction and interference effects. It turns out to be important for imaging applications of synchrotron radiation. It is possible to distinguish between a longitudinal (or temporal) and a transverse (or spatial) coherence length. The former represents the length over which two harmonic components (with a wavelength difference $\Delta\lambda$) of an electromagnetic wave develop a phase difference of 2π radians and it is given by $l_c^{(l)} = \lambda^2/(\Delta\lambda)$. It mainly depends on the quality of the monochromator used, which defines the ratio $\lambda/\Delta\lambda$. The latter arises from the interference of waves with the same wavelength but different propagation direction: it is due to the finite divergence $\Delta\theta$ of the radiation source and it is given by $l_c^{(t)} = \lambda/(2\Delta\theta) = \lambda R/(2D)$, being R the distance from the source to the observation point and D the lateral source size.

Synchrotron radiation also presents a high degree of polarization, whose direction depends on the line of sight considered. Viewed in the electrons orbital plane, the polarization is linear and lies in the plane of the orbit described by the electrons. Finally, synchrotrons represent tunable radiation sources, since they can emit photons over a wide spectrum, ranging from UV to hard X-ray. This makes synchrotron radiation necessary for spectroscopy and generally in any cases where a precise absorption edge of the probed sample has to be selected (e.g. Resonant Elastic X-ray Scattering, REXS).

Appendix B

PyFAI, a fast azimuthal integration python tool

PyFAI is a versatile and open source Python library for azimuthal regrouping of 2D diffraction data internally developed by the scientific staff of the European Synchrotron Radiation Facility (Kieffer and Karkoulis [32], Kieffer and Wright [31]). It provides a collection of tools and also a few programs which can be used directly (outside of the Python language). Azimuthal regrouping (also called *caking*) is a transformation from the Cartesian coordinates of the 2D diffraction frames acquired by an area detector to a polar coordinates system made up by the so called azimuthal angle χ in the angular direction and either the scattering angle 2θ or the transferred momentum Q in the radial direction. In order to accomplish this task, each pixel of the detector has to be associated with the corresponding polar coordinates $(2\theta, \chi)$ (or (Q, χ)). The association is carried out by PyFAI using the geometry defined by Boesecke [6]. It defines the detector position with respect to the sample through a set of 6 parameters: 3 rotations around the 3 main detector axes and 3 additional parameters to fix the position of the so called Point Of Normal Incidence (PONI). The latter is defined by giving a pair of coordinates (x, y) identifying the position on the detector surface and the normal distance D to the sample. Since this geometry does not consider the incidence position of the direct beam as origin, PyFAI is compatible with any flat area detector at any orientation, even significantly tilted (as the one described in Section 3.2). The result of the azimuthal regrouping procedure is a 2D array of intensity values as a function of 2θ (or Q) and χ: an example is provided by Figure 4.5.

The definition of the experimental geometry (that is to say the relative sample-detector position) represents the first step of the data analysis. It can be carried out through the `pyFAI-calib.py` calibration program, which makes a constrained least squares optimization based on the known d-spacings of the Debye rings of an image collected from a reference sample, along with the wavelength of the incident radiation and the detector pixel dimensions. An example of usage of the calibration program is provided by the following prompt command:

```
pyFAI-calib.py -S d_spacings.txt -w 1.771 -p 64.5 reference_image.edf
```

where the flags `-S`, `-w` and `-p` are used to specify the text file containing the d-spacing values, the wavelength (in Å) and the detector pixel side (in μm) respectively, while `reference_image.edf` is the file containing the reference image used for the calibration. The output of the calibration program is a `.poni` file containing the geometrical parameters defining the experimental geometry. Refinement of a calibration with a good initial set of parameters can be done using the `pyFAI-recalib.py` script, starting from a previously calculated `.poni` file.

Once the `.poni` file is available, it can be imported in a Python interactive session or in a Python script through the command `pyFAI.load()`, receiving as input the path of the file. The azimuthal regrouping can then be performed, either interactively or via scripts, through the attribute `.integrate2d()`, as shown in the following example

```
ai=pyFAI.load("calibration.poni")
integration = ai.integrate2d("detector_acquisition.edf", nbPt_rad=1000, nbPt_azim
    ↪ =2000,radial_range=(27,92), unit="2th_deg")
```

Here `detector_acquisition.edf` is the name of the diffraction image given as input, `nbPt_rad` and `nbPt_azim` specify the number of radial and azimuth points respectively, `radial_range` is the tuple with the first and last value of the radial coordinate to consider and `unit` specifies the desired radial coordinate (in this example the angle 2θ). The output of the `.integrate2d()` command is a 2D array containing the azimuthal regrouped intensity values. While performing the regrouping, the same command can apply, through a set of optional arguments, some corrections to the image given as input: these are the dark current subtraction and the flat field, the solid angle and the polarization corrections. In the following appendix, the full Python script used to perform the azimuthal regrouping of the diffraction data discussed in Chapters 4 and 5 will be reported.

Appendix C

Python scripts code

Hereafter the most relevant Python scripts used for the data analysis presented in Chapters 4 and 5 are reported.

PyFAI azimuthal integration: intensity maps. The code used to calculate the intensity maps corresponding to the ω angle scans (see Figure 4.7) is here reported. The azimuthal integration of the diffraction images is performed through the PyFAI library (described in the previous appendix), while the detector images are imported using the PyMca module, developed by the Software Group of the European Synchrotron Radiation Facility.

```
from PyMca import EdfFile
import pyFAI
from pylab import*

###Dictionary with the scans###
scans={
#8nm
"Scan69": (arange(1526,1797),"STO"),
#5.3nm
"Scan114": (arange(560,831),"STO"),
#4nm
"Scan39": (arange(1070,1351),"Gold"),
#3nm
"Scan169": (arange(1053,1324),"Gold"),
#2nm
"Scan141": (arange(1290,1561),"Gold"),
#1nm
"Scan99": (arange(1114,1385),"Gold"),
}

###Dictionaries with the counting times###
countingTime={
"Scan69": 0.002,
"Scan114": 0.1,
"Scan39": 0.75,
"Scan169": 1,
"Scan141": 5,
```

```
"Scan99": 10,
}

###Dictionary with the folders names###
folders={
"Scan69": "HB19A/hb19a_",
"Scan114": "HB18A/hb18a_",
"Scan39": "HB17A/hb17a_",
"Scan169": "HB16A/hb16a_",
"Scan141": "HB15A/hb15a_",
"Scan99": "HB14A/hb14a_",
}

###Dictionary with the 2theta integration range (STO samples)###
intRangeSTO={
"STO(110)": (36.5,38.5),
"Au(111)": (43,45.3),
"STO(111)": (45.48,47.5),
"Au(200)": (50.04,52.55)
}

###Dictionary with the 2theta integration range (Gold samples)###
intRangeGold={
"Au(111)": (43,45.3),
"Au(200)": (50.04,52.55)
}

idx=0 #Index of intensityMap row: each row is the intensity plot of a different
    ↪ image
firstIntegration=True

###################################
#LOOP OF THE SCANS
###################################
for Scan_number in scans:

     Images_vector=scans[Scan_number][0] #Vector with the numbers of the images
     Images_dictionary=dict()
     intensityMap=zeros((len(Images_vector),2000)) #Intensity map

     ######################
     #PONI FILE
     ######################
     if (Scan_number=="Scan79"):
         ai=pyFAI.load("hb19a_3192_Fit2D.poni")
     if (Scan_number=="Scan122"):
         ai=pyFAI.load("AvgScan122_Fit2D.poni")
     if (Scan_number=="Scan182"):
         ai=pyFAI.load("AvgScan182_Fit2D_Scan76.poni")
     else:
         ai=pyFAI.load("hb19a_2891_Fit2D.poni")

     ##############################################
```

```
80      #LOOP TO LOAD THE IMAGES OF A SCAN
81      ################################################
82      for imageNumber in Images_vector:
83          dataRaw=EdfFile.EdfFile("%s%04d_NoDark.edf"%(folders[Scan_number],
                ↪ imageNumber),access="rb").GetData(0)/countingTime[Scan_number]
84          print "\n%s%04d_NoDark.edf read"%(folders[Scan_number],imageNumber)
85          Images_dictionary[imageNumber]=dataRaw
86
87      ########################
88      #INTEGRATION
89      ########################
90      ###2THETA RANGE###
91      if (scans[Scan_number][1]=="STO"):
92          intRange=intRangeSTO
93      if (scans[Scan_number][1]=="Gold"):
94          intRange=intRangeGold
95      for reflection in intRange:
96          intLimit=intRange[reflection]
97          for imageNumber in sorted(Images_dictionary.keys()):
98
99              ###INTEGRATION###
100             integration = ai.integrate2d(Images_dictionary[imageNumber], nbPt_rad
                    ↪ =1000, nbPt_azim=2000,radial_range=intLimit, unit="2th_deg")
101             print "\n%s%04d_NoDark.edf %s integrated"%(folders[Scan_number],
                    ↪ imageNumber,reflection)
102
103             ###CREATION OF THE AZIMUTHAL ANGLES VECTOR (ONLY FOR THE FIRST
                    ↪ INTEGRATION)###
104             if (firstIntegration==True):
105                 azimuth=zeros(2000)
106                 i=0     #Index of the azimuth vector
107                 for x in integration[2]:
108                     if (x<0):
109                         azimuth[i]=integration[2][i]+360
110                     else:
111                        azimuth[i]=integration[2][i]
112                     i=i+1
113                 firstIntegration=False
114
115             ###CREATION OF THE INTENSITY MAP###
116             intensity=zeros(2000)
117             l=0 #Index of the intensity vector
118             for i in argsort(azimuth):
119                 intensity[l]=integration[0].sum(axis=1)[i]
120                 l=l+1
121             intensityMap[idx]=intensity
122             idx=idx+1
123
124         ################################################################
125         #WRITING OF THE INTENSITY MAP IN A .EDF OUTPUT FILE
126         ################################################################
127         idx=0
128         save=EdfFile.EdfFile("Intensity_maps\map%s%s.edf"%(Scan_number,reflection)
```

```
            ↪ , access="a+")
        info={}
        info["Title"]=""
        save.WriteImage(info,intensityMap)
        print "\n\nIntensity map map%s%s.edf written\n\n"%(Scan_number,reflection)
```

Pole figures. Starting from the intensity maps calculated through the code of the previous paragraph, the following Python script was used to calculate the corresponding pole figures. The calculations are based on those presented in Section 2.3.2. It is worth noticing that the azimuthal angle χ used by PyFAI (called `azimuth` in the script) does not coincide with the γ angle of Section 2.3.2: they are instead related by the following

$$\gamma = 270^\circ - \chi$$

```
from __future__ import division
from pylab import*
from PyMca import EdfFile

###Dictionary with the scans###
scans={
"Scan69": (-14,13,45,-8.8,-8.8,0.2,0,"STO",8), #"Scan number" : (first omega value,
    ↪  last omega value, phi, psi, eta, x_off, y_off, sample type, Au thickness)
"Scan114": (-14,13,45,-10.2,-10.2,0.05,0.6,"STO",5.3),
"Scan39": (-14,14,45,-8.7,-8.7,0.4,0,"Gold",4),
"Scan169": (-14,13,45,-10,-10,0.4,0.3,"Gold",3),
"Scan141": (-14,13,225,9.4,9.4,-0.3,0.94,"Gold",2),
"Scan99": (-14,13,225,9.4,9.4,0.35,0,"Gold",1),
}


diffraction_rings_STO={
"STO(110)": (37.413,55,121.5), #"Reflection" :(2theta, first azimuth value, last
    ↪ azimuth value)
"Au(111)": (44.167,44.5,120),
"STO(111)": (46.258,45.5,119),
"Au(200)": (51.458,48,116.5),
}

diffraction_rings_Gold={
"Au(111)": (44.167,44.5,120), #"Reflection" :(2theta, first azimuth value, last
    ↪ azimuth value)
"Au(200)": (51.458,48,116.5),
}

###################################
#LOOP OF THE SCANS
###################################
for Scan_number in scans:
    if (scans[Scan_number][7]=="STO"):
        diffraction_ring=diffraction_rings_STO
    if (scans[Scan_number][7]=="Gold"):
```

```
35          diffraction_ring=diffraction_rings_Gold
36
37      ##########################################
38      #SAMPLE ROTATIONS
39      ##########################################
40      omega_range=(scans[Scan_number][0],scans[Scan_number][1]) # (initial value,
            ↪ final value) [deg]
41      if (omega_range[0]>omega_range[1]):
42          omega_vector=arange(omega_range[0],omega_range[1]-0.1,-0.1)
43      else:
44          omega_vector=arange(omega_range[0],omega_range[1]+0.1,+0.1)
45      scan_points=abs(omega_vector[0]-omega_vector[len(omega_vector)-1])/abs(abs(
            ↪ omega_vector[0])-abs(omega_vector[1]))+1
46      phi_deg=scans[Scan_number][2]
47      psi_deg=scans[Scan_number][3]
48      eta_deg=scans[Scan_number][4]
49      x_off_deg=scans[Scan_number][5]
50      y_off_deg=scans[Scan_number][6]
51
52      for reflection in diffraction_ring:
53
54          ##########################################
55          #INTENSITY MAP AND DIFFRACTION SPACE
56          ##########################################
57          intensity_map=EdfFile.EdfFile("Intensity_mapS\map%s%s.edf"%(Scan_number,
                ↪ reflection),access="rb").GetData(0)
58          print "map%s%s.edf read\n"%(Scan_number,reflection)
59          pyfai_azimuth_vector=arange
                ↪ (-179.90997769,179.90999135+0.17999998,0.17999998)
60          azimuth=zeros(2000)
61          j=0 #Index of the azimuth vector
62          for x in pyfai_azimuth_vector:
63              if (x<0):
64                  azimuth[j]=pyfai_azimuth_vector[j]+360
65              else:
66                 azimuth[j]=pyfai_azimuth_vector[j]
67              j=j+1
68          azimuth=sort(azimuth)
69          first_azimuth=[i for i,j in enumerate(azimuth) if j>270-diffraction_ring[
                ↪ reflection][2] and j<270-diffraction_ring[reflection][1]][0]
70          last_azimuth=[i for i,j in enumerate(azimuth) if j>270-diffraction_ring[
                ↪ reflection][2] and j<270-diffraction_ring[reflection][1]][-1]
71          azimuth_range=(first_azimuth,last_azimuth)
72          two_theta=diffraction_ring[reflection][0] #[deg]
73
74          ##########################################
75          #POLE FIGURE VECTORS
76          ##########################################
77          beta=zeros(scan_points*(azimuth_range[1]-azimuth_range[0]))
78          r=zeros(scan_points*(azimuth_range[1]-azimuth_range[0]))
79          intensity=zeros(scan_points*(azimuth_range[1]-azimuth_range[0]))
80          i=0#Index of the pole figures vectors
81
```

```
82          ##########################################
83          #POLE FIGURE CALCULATION
84          ##########################################
85          for col in arange(scan_points):
86              omega_deg=omega_vector[col]
87              for row in arange(azimuth_range[0],azimuth_range[1]):
88                  gamma=-azimuth[row]+270 #[deg]
89
90                      ##########################################
91                      #Diffraction space (2theta,gamma) [deg] --> Reciprocal lattice
                            ↪ unit vector (Laboratory coordinate system)
92                      ##########################################
93                      hlab=array([[-sin(two_theta/2/180*pi)],[-cos(two_theta/2/180*pi
                            ↪ )*sin(gamma/180*pi)],[-cos(two_theta/2/180*pi)*cos(gamma
                            ↪ /180*pi)]])
94
95                      ##############################
96                      #(xlab,ylab,zlab)-->(x,y,z) with all sample rotations and
                            ↪ offset = 0
97                      ##############################
98                      zlab_rot=array([[-1,0,0],[0,-1,0],[0,0,1]]) #180 degrees
                            ↪ rotation about zlab
99                      xlab_rot=array([[1,0,0],[0,0,1],[0,-1,0]]) #-90 degrees
                            ↪ rotation  about xlab
100                     LAB=dot(xlab_rot,zlab_rot)
101                     hsample_zero=dot(LAB,hlab)
102
103                     ##############################
104                     #Motor values in degrees --> (omega,psi,phi) in radians
105                     ##############################
106                     omega=omega_deg/180*pi
107                     phi=phi_deg/180*pi
108                     psi=psi_deg/180*pi
109                     eta=eta_deg/180*pi
110
111                     ##############################
112                     #SAMPLE ROTATIONS: R MATRIX
113                     ##############################
114                     ###y axis: omega###
115                     omega_rot=array([[cos(omega),0,-sin(omega)],[0,1,0],[sin(omega)
                            ↪ ,0,cos(omega)]])
116                     ###z axis: phi - left handed###
117                     phi_rot=array([[cos(-phi),sin(-phi),0],[-sin(-phi),cos(-phi)
                            ↪ ,0],[0,0,1]])
118                     ###x axis: psi(lt) - left handed###
119                     psi_rot=array([[1,0,0],[0,cos(-psi),sin(-psi)],[0,-sin(-psi),
                            ↪ cos(-psi)]])
120                     ###y axis: eta(ut) ###
121                     eta_rot=array([[cos(eta),0,-sin(eta)],[0,1,0],[sin(eta),0,cos(
                            ↪ eta)]])
122                     R=dot(eta_rot,dot(psi_rot,dot(phi_rot,omega_rot)))
123                     hsample_noOff=dot(R,hsample_zero)
124
```

```
                    ##############################
                    #SAMPLE OFFSET: U MATRIX
                    ##############################
                    x_off=x_off_deg/180*pi
                    y_off=y_off_deg/180*pi
                    off_x_rot=array([[1,0,0],[0,cos(x_off),sin(x_off)],[0,-sin(
                        ↪ x_off),cos(x_off)]])
                    off_y_rot=array([[cos(y_off),0,-sin(y_off)],[0,1,0],[sin(y_off)
                        ↪ ,0,cos(y_off)]])
                    U=dot(off_x_rot,off_y_rot)
                    hsample=dot(U,hsample_noOff)

                    ########################################
                    #POLE FIGURE (pole mapping equations)
                    ########################################
                    alpha_pfigure=arcsin(abs(hsample[2]))/pi*180
                    if(hsample[1]>0 or hsample[1]==0):
                        beta[i]=arccos(hsample[0]/sqrt(pow(hsample[0],2)+pow(
                            ↪ hsample[1],2)))/pi*180
                    else:
                        beta[i]=-arccos(hsample[0]/sqrt(pow(hsample[0],2)+pow(
                            ↪ hsample[1],2)))/pi*180
                    r[i]=tan((45-alpha_pfigure/2)/180*pi)
                    intensity[i]=intensity_map[col,row]
                    i=i+1

        ##################################
        #OUTPUT .DAT FILES
        ##################################
        file=open("PoleFigure%s%s.dat"%(Scan_number,reflection),mode="w")
        for i in arange(len(intensity)):
          file.writelines(["%f"%beta[i],"       ","%f"%r[i],"       ","%f"%
              ↪ intensity[i],"\n"])
```

Simulated pole figures. The following script was used to calculate the Au{220} simulated pole figure of Figure 5.13c. For the other Au reflections the simulations were obtained in an analogous way.

```
from __future__ import division
from pylab import *
mpl.rcParams["mathtext.default"] = "regular"

#####################################
#(111)-ORIENTED NANOPARTICLE
#####################################

hgold111_reflections=[
array([[2],[2],[0]]),array([[2],[0],[2]]),array([[0],[2],[2]]),
array([[-2],[2],[0]]),array([[-2],[0],[2]]),array([[0],[-2],[2]]),
array([[2],[-2],[0]]),array([[2],[0],[-2]]),array([[0],[2],[-2]]),
array([[-2],[-2],[0]]),array([[-2],[0],[-2]]),array([[0],[-2],[-2]])
]
```

```
beta_values111=[ #deg
0,
45,
]

###################################
#POLE FIGURE VECTORS
###################################
alpha_pfigure111=list()
beta111=list()
r111=list()
alpha_pfigure111_45=list()
beta111_45=list()
r111_45=list()

for hgold in hgold111_reflections:
    hgold=hgold/sqrt(hgold[0]**2+hgold[1]**2+hgold[2]**2)
    ###################################################
    #SYMMETRY EQUIVALENT BETA ROTATIONS
    ###################################################
    for beta_deg in beta_values111:
        if (beta_deg==0):
            alpha=beta_deg/180*pi
            beta_equivalent=[beta,beta+pi/2,beta+pi,beta+3*pi/2,-beta,-beta+pi/2,-
                ↪ beta+pi,-beta+3*pi/2]
            for rotation in beta_equivalent:
                ###########################################################
                #GOLD REFERENCE SYSTEM --> SAMPLE REFERENCE SYSTEM
                ###########################################################
                phi=pi/4 #radians
                eta=arccos(1/sqrt(3))
                rot_z=array([[cos(phi),sin(phi),0],[-sin(phi),cos(phi),0],[0,0,1]])
                    ↪  #45deg around Au(001)
                rot_y=array([[cos(eta),0,-sin(eta)],[0,1,0],[sin(eta),0,cos(eta)]])
                    ↪  #arccos(1/sqrt(3))=0.9553deg around Au(-1,1,0)
                rot_beta=array([[cos(-rotation),sin(-rotation),0],[-sin(-rotation),
                    ↪ cos(-rotation),0],[0,0,1]]) #beta rotation
                V=dot(rot_beta,dot(rot_y,rot_z))
                hsample=dot(V,hgold)
                ############################
                #POLE FIGURE
                ############################
                if (hsample[2] > -5.55111512e-16): #Condition for reflection
                    ↪ geometry
                    if (hsample[2]<1):
                        alpha_pfigure111.append(arcsin(abs(float(hsample[2])))/pi
                            ↪ *180)
                        if(hsample[1]>0 or hsample[1]==0):
                            beta111.append(arccos(float(hsample[0])/sqrt(pow(float(
                                ↪ hsample[0]),2)+pow(float(hsample[1]),2)))/pi
                                ↪ *180)
                        else:
                            beta111.append(-arccos(float(hsample[0])/sqrt(pow(float
```

```
                                ↪ (hsample[0]),2)+pow(float(hsample[1]),2)))/pi
                                ↪ *180)
60                          r111.append(tan((45-alpha_pfigure111[-1]/2)/180*pi))
61                      else:
62                          alpha_pfigure111.append(90)
63                          r111.append(0)
64                          beta111.append(0)
65          else:
66              beta=beta_deg/180*pi
67              beta_equivalent=[beta,beta+pi/2,beta+pi,beta+3*pi/2,-beta,-beta+pi/2,-
                    ↪ beta+pi,-beta+3*pi/2]
68              for rotation in beta_equivalent:
69                  ##########################################################
70                  #GOLD REFERENCE SYSTEM --> SAMPLE REFERENCE SYSTEM
71                  ##########################################################
72                  phi=pi/4 #radians
73                  eta=arccos(1/sqrt(3))
74                  rot_z=array([[cos(phi),sin(phi),0],[-sin(phi),cos(phi),0],[0,0,1]])
                        ↪  #45deg around Au(001)
75                  rot_y=array([[cos(eta),0,-sin(eta)],[0,1,0],[sin(eta),0,cos(eta)]])
                        ↪  #arccos(1/sqrt(3))=0.9553deg around Au(-1,1,0)
76                  rot_beta=array([[cos(-rotation),sin(-rotation),0],[-sin(-rotation),
                        ↪ cos(-rotation),0],[0,0,1]]) #beta rotation
77                  V=dot(rot_beta,dot(rot_y,rot_z))
78                  hsample=dot(V,hgold)
79                  ############################
80                  #POLE FIGURE
81                  ############################
82                  if (hsample[2] > -5.55111512e-16): #Condition for reflection
                        ↪ geometry
83                      if (hsample[2]<1):
84                          alpha_pfigure111_45.append(arcsin(abs(float(hsample[2])))/
                                ↪ pi*180)
85                          if(hsample[1]>0 or hsample[1]==0):
86                              beta111_45.append(arccos(float(hsample[0])/sqrt(pow(
                                    ↪ float(hsample[0]),2)+pow(float(hsample[1]),2)))/
                                    ↪ pi*180)
87                          else:
88                              beta111_45.append(-arccos(float(hsample[0])/sqrt(pow(
                                    ↪ float(hsample[0]),2)+pow(float(hsample[1]),2)))/
                                    ↪ pi*180)
89                          r111_45.append(tan((45-alpha_pfigure111_45[-1]/2)/180*pi))
90                      else:
91                          alpha_pfigure111_45.append(90)
92                          r111_45.append(0)
93                          beta111_45.append(0)
94
95  ######################################
96  #(002)-ORIENTED NANOPARTICLE
97  ######################################
98
99  hgold200_reflections=[
100 array([[2],[2],[0]]),array([[2],[0],[2]]),array([[0],[2],[2]]),
```

```
array([[-2],[2],[0]]),array([[-2],[0],[2]]),array([[0],[-2],[2]]),
array([[2],[-2],[0]]),array([[2],[0],[-2]]),array([[0],[2],[-2]]),
array([[-2],[-2],[0]]),array([[-2],[0],[-2]]),array([[0],[-2],[-2]])
]
beta_values200=[ #deg
0,
45
]

##########################################
#POLE FIGURE VECTORS
##########################################

alpha_pfigure200=list()
beta200=list()
r200=list()
alpha_pfigure200_45=list()
beta200_45=list()
r200_45=list()

for hgold in hgold200_reflections:
    hgold=hgold/sqrt(hgold[0]**2+hgold[1]**2+hgold[2]**2)
    ##########################
    #SYMMETRY EQUIVALENT BETA ROTATIONS
    ##########################
    for beta_deg in beta_values200:
        if (beta_deg==0):
            beta=beta_deg/180*pi
            beta_equivalent=[beta,beta+pi/2,beta+pi,beta+3*pi/2,-beta,-beta+pi/2,-
                ↪ beta+pi,-beta+3*pi/2]
            for rotation in beta_equivalent:
                ##########################################################
                #GOLD REFERENCE SYSTEM --> SAMPLE REFERENCE SYSTEM
                ##########################################################
                phi=pi/4
                rot_z=array([[cos(phi),sin(phi),0],[-sin(phi),cos(phi),0],[0,0,1]])
                    ↪  #45deg around Au(001)
                rot_beta=array([[cos(-rotation),sin(-rotation),0],[-sin(-rotation),
                    ↪ cos(-rotation),0],[0,0,1]]) #beta rotation
                V=dot(rot_beta,rot_z)
                hsample=dot(V,hgold)
                ############################
                #POLE FIGURE
                ############################
                if (hsample[2] > -5.55111512e-16): #Condition for reflection
                    ↪ geometry
                    if (hsample[2]<1):
                        alpha_pfigure200.append(arcsin(abs(float(hsample[2])))/pi
                            ↪ *180)
                        if(hsample[1]>0 or hsample[1]==0):
                            beta200.append(arccos(float(hsample[0])/sqrt(pow(float(
                                ↪ hsample[0]),2)+pow(float(hsample[1]),2)))/pi
                                ↪ *180)
```

```
                        else:
                            beta200.append(-arccos(float(hsample[0])/sqrt(pow(float
                                ↪ (hsample[0]),2)+pow(float(hsample[1]),2)))/pi
                                ↪ *180)
                        r200.append(tan((45-alpha_pfigure200[-1]/2)/180*pi))
                    else:
                        alpha_pfigure200.append(90)
                        r200.append(0)
                        beta200.append(0)
        else:
            beta=beta_deg/180*pi
            beta_equivalent=[beta,beta+pi/2,beta+pi,beta+3*pi/2,-beta,-beta+pi/2,-
                ↪ beta+pi,-beta+3*pi/2]
            for rotation in beta_equivalent:
                ############################################################
                #GOLD REFERENCE SYSTEM --> SAMPLE REFERENCE SYSTEM
                ############################################################
                rot_z=array([[cos(phi),sin(phi),0],[-sin(phi),cos(phi),0],[0,0,1]])
                    ↪  #45deg around Au(001)
                rot_beta=array([[cos(-rotation),sin(-rotation),0],[-sin(-rotation),
                    ↪ cos(-rotation),0],[0,0,1]]) #beta rotation
                V=dot(rot_beta,rot_z)
                hsample=dot(V,hgold)
                ############################
                #POLE FIGURE
                ############################
                if (hsample[2] > -5.55111512e-16): #Condition for reflection
                    ↪ geometry
                    if (hsample[2]<1):
                        alpha_pfigure200_45.append(arcsin(abs(float(hsample[2])))/
                            ↪ pi*180)
                        if(hsample[1]>0 or hsample[1]==0):
                            beta200_45.append(arccos(float(hsample[0])/sqrt(pow(
                                ↪ float(hsample[0]),2)+pow(float(hsample[1]),2)))/
                                ↪ pi*180)
                        else:
                            beta200_45.append(-arccos(float(hsample[0])/sqrt(pow(
                                ↪ float(hsample[0]),2)+pow(float(hsample[1]),2)))/
                                ↪ pi*180)
                        r200_45.append(tan((45-alpha_pfigure200_45[-1]/2)/180*pi))
                    else:
                        alpha_pfigure200_45.append(90)
                        r200_45.append(0)
                        beta200_45.append(0)

##############################
#POLAR PLOT
##############################
beta200=array(beta200)
r200=array(r200)
beta200_45=array(beta200_45)
r200_45=array(r200_45)
beta111=array(beta111)
```

```
r111=array(r111)
beta111_45=array(beta111_45)
r111_45=array(r111_45)
yticks=list()
ylabel=list()
degree_symbol="\u00b0"
degree_symbol=degree_symbol.decode("unicode-escape")
for i in arange(0,0.5,0.1):
    yticks.append(i)
    if (i==0):
        ylabel.append("(001)")
    else:
        ylabel.append("%d%s"%(int(90-(45-arctan(i)/pi*180)*2),degree_symbol))
fig=figure(1,figsize=(17,12))
ax = subplot(111, polar=True)
scatter(beta200_45/180*pi,r200_45,c="none",edgecolor="red",s=350, label=r"(001)$_{
    ↪ STO}$ || (002)$_{Au}$ - $\beta_{002}$=45%s"%degree_symbol,linewidth=3)
scatter(beta200/180*pi,r200,c="red",s=350, label=r"(001)$_{STO}$ || (002)$_{Au}$ -
    ↪ $\beta_{002}$=0%s"%degree_symbol,linewidth=0 )
scatter(beta111_45/180*pi,r111_45,c="none",edgecolor="black",s=200, label=r"(001)$_
    ↪ {STO}$ || (111)$_{Au}$ - $\beta_{111}$=45%s"%degree_symbol,linewidth=2)
scatter(beta111/180*pi,r111,c="black",s=200, label=r"(001)$_{STO}$ || (111)$_{Au}$
    ↪ - $\beta_{111}$=0%s"%degree_symbol)
legend(scatterpoints=1, bbox_to_anchor=[1.05, 1.5],fontsize=28)
ax.set_rmax(0.5)
ax.set_yticks(yticks)
ax.set_yticklabels(ylabel)
ax.set_xticklabels(["(100)","(110)","(010)","(-110)","(-100)","(-1-10)","(0-10)","
    ↪ (1-10)"])
ax.xaxis.label.set_fontsize(28)
ax.yaxis.label.set_fontsize(28)
for xticks in ax.get_xticklabels():
    xticks.set_fontsize(28)
for yticks in ax.get_yticklabels():
    yticks.set_fontsize(28)
savefig("SimulationPoleFigureAu{220}.png")
show()
```

Acknowledgments

The time has come to thank many people who, each one in his own way, have contributed to this work. First of all I would like to thank Dr. Carsten Detlefs, my supervisor at ID06, and all the beamline staff for having given me the incredible opportunity to work for almost 10 months in a prestigious research facility as is the ESRF and for having made me taste what doing research really means. Secondly, thanks to my professor Giacomo Ghiringhelli, who first offered me the chance to conclude my studies at the ESRF, and to Dr. Claudio Mazzoli for the support provided during all the duration of the internship. Thanks to all the group of the Jena university which provided the samples and always trusted my work; a special thank you to Christian and Hendrik for the great time spent together on the beamline for my first experiment and for the continuous and accurate updates from Germany during all the time. Thanks also to Jonathan Wright and Claudio Ferrero for the valuable support in the PyFAI software usage and for his advice in the early stages of the data analysis respectively.

Thanks to my friend and beamline colleague Hugh Simons for his precious language support during the draft of the present thesis (he surely knows better than anyone how it was needed!) and, above all, for our deep conversations about Italian style between one data analysis and the other; in addition he showed me that also collecting quite mysterious diffraction images nightlong can be a funny pastime. Of course a big thank you goes to all the people from all over Europe (and not only) I met in Grenoble during my 10 months stay and to my friends from Italy (Mauro, Silvia, Matteo and Andrea) with whom I shared this beautiful experience: I will never forget our sunny week-end excursions to La Bastille and our winter ski sessions in all the nearby available resorts, even with more than uncertain weather conditions.

Looking back at the past five years of university in Milano, I cannot do without thanking all my classmates with whom I shared joys and sorrows of the life as an out of town student. They have been five years packed with events, full of pleasant and funny moments, as the beers (or the unlikely "potions" of the *Saloon* bar) drunk in company during the Milano nightlife or the endless return at home late in the night, when you realize it would have been better avoiding to miss the last tram; surely less pleasant but equally memorable the study sessions of titanic proportions past the exams in the Architecture or Maths library, spent trying to get a glimmer of meaning in absolutely meaningless notes (of as much meaningless lectures). Very special thanks go also to my little hometown friends for the unforgettable leisure time we spent together in the rare (and unfortunately always short) periods I managed to stay home during my five years absence (for which I guess I should beg their pardon...).

Last but not least, I would like to thank my family (this time more than any other) for having always unconditionally encouraged me to take my own path, no matter how long it would have implied staying away from them. All I have done in the past five years would have been impossible without them, and I will always be grateful for that.

List of Figures

Bibliography

[1] Neil W Ashcroft and N David Mermin. Solid state phys. *Saunders, Philadelphia*, 1976.

[2] LV Azaroff. Elements of X-ray Crvstallographv, 1968.

[3] Alexis T Bell. The impact of nanoscience on heterogeneous catalysis. *Science*, 299(5613): 1688–1691, 2003.

[4] Hendrik Bernhardt. Untersuchungen an epitaktischen Schichten mit selbstorganisiert wachsenden Gold-Nanopartikeln. Master degree thesis, Friedrich-Schiller-Universität Jena, 2013.

[5] Hendrik Bernhardt, Christian Katzer, Frank Schimdl, and Ingo Uschmann. X-ray diffraction and TEM measurements, Friedrich-Schiller-Universität Jena. Unpublished raw data, 2013.

[6] Peter Boesecke. Reduction of two-dimensional small-and wide-angle x-ray scattering data. *Applied Crystallography*, 2007.

[7] CF Bohren and DR Huffman. Absorbing and scattering of light by small particles. *Wiley Interscience*, 13(2):123–127, 1983.

[8] William R Busing and Henri A Levy. Angle calculations for 3-and 4-circle x-ray and neutron diffractometers. *Acta Crystallographica*, 22(4):457–464, 1967.

[9] Charles T Campbell. Ultrathin metal films and particles on oxide surfaces: structural, electronic and chemisorptive properties. *Surface Science Reports*, 27(1):1–111, 1997.

[10] Richard Kounai Chang and Thomas Elton Furtak. *Surface enhanced Raman scattering*, volume 233. Plenum Press New York, 1982.

[11] Dominique Chatain, Veronique Ghetta, and Paul Wynblatt. Equilibrium shape of copper crystals grown on sapphire. *Interface Science*, 12(1):7–18, 2004.

[12] MS Chen and DW Goodman. The structure of catalytically active gold on titania. *Science*, 306(5694):252–255, 2004.

[13] S Christke, C Katzer, V Grosse, F Schmidl, G Schmidl, W Fritzsche, J Petschulat, T Pertsch, and M Rettenmayr. Optical resonances of self-organized monocrystalline Au nanoparticles embedded in $SrTiO_3$ matrix. *Optical Materials Express*, 1(5):890–897, 2011.

[14] DJ Eaglesham, H-J Gossmann, and M Cerullo. Limiting thickness h_ {epi} for epitaxial growth and room-temperature Si growth on Si (100). *Physical Review Letters*, 65(10): 1227, 1990.

[15] DJ Eaglesham, LN Pfeiffer, KW West, and DR Dykaar. Limited thickness epitaxy in GaAs molecular beam epitaxy near 200° C. *Applied Physics Letters*, 58(1):65–67, 1991.

[16] Andrew J Francis and Paul A Salvador. Crystal orientation and surface morphology of face-centered-cubic metal thin films deposited upon single-crystal ceramic substrates using pulsed laser deposition. *Journal of Materials Research*, 22(01):89–102, 2007.

[17] Walter Friedrich, Paul Knipping, and Max Laue. Interferenzerscheinungen bei röntgenstrahlen. *Annalen der Physik*, 346(10):971–988, 1913.

[18] Herbert Fröhlich. *Theory of dielectrics*, volume 18. Clarendon Press Oxford, 1949.

[19] Qiang Fu and Thomas Wagner. Interaction of nanostructured metal overlayers with oxide surfaces. *Surface Science Reports*, 62(11):431–498, 2007.

[20] Sergey V Gaponenko. *Introduction to nanophotonics*. Cambridge University Press, 2010.

[21] NA Gjostein. Surface self-diffusion in fcc and bcc metals: A comparison of theory and experiment. Technical report, Ford Motor Co., Dearborn, Mich., 1968.

[22] Andy Gotz, Petri Makijarvi, Bernard Regad, Manuel Perez, and Paolo Mangiagalli. Esrf aerial view. http://www.linuxjournal.com/article/3612, 1999.

[23] Veit Grosse, Sebastian Engmann, Frank Schmidl, Andreas Undisz, Markus Rettenmayr, and Paul Seidel. Formation of gold nano-particles during pulsed laser deposition of $YBa_2Cu_3O_7$–δ thin films. *Physica status solidi (RRL) - Rapid Research Letters*, 4(5-6): 97–99, 2010.

[24] Encai Hao and George C Schatz. Electromagnetic fields around silver nanoparticles and dimers. *The Journal of Chemical Physics*, 120(1):357–366, 2003.

[25] Bob B He. *Two-dimensional X-ray Diffraction*. Wiley. com, 2011.

[26] JC Heyraud and JJ Metois. Equilibrium shape and temperature; lead on graphite. *Surface Science*, 128(2):334–342, 1983.

[27] JB Jackson and NJ Halas. Silver nanoshells: variations in morphologies and optical properties. *The Journal of Physical Chemistry B*, 105(14):2743–2746, 2001.

[28] C Katzer, M Schmidt, P Michalowski, D Kuhwald, F Schmidl, V Grosse, S Treiber, C Stahl, J Albrecht, U Hübner, et al. Increased flux pinning in $YBa_2Cu_3O_7$- δ thin-film devices through embedding of Au nano crystals. *EPL (Europhysics Letters)*, 95(6): 68005, 2011.

[29] C Katzer, M Westerhausen, P Naujok, H Bernhardt, G Schmidl, W Fritzsche, A Undisz, M Drüe, M Rettenmayr, and F Schmidl. Matrix induced in-situ growth of crystalline Au nanoparticles for photonic applications. In *SPIE NanoScience+ Engineering*, pages 88070K–88070K. International Society for Optics and Photonics, 2013.

[30] K Lance Kelly, Eduardo Coronado, Lin Lin Zhao, and George C Schatz. The optical properties of metal nanoparticles: the influence of size, shape, and dielectric environment. *The Journal of Physical Chemistry B*, 107(3):668–677, 2003.

[31] J Kieffer and JP Wright. PyFAI: a python library for high performance azimuthal integration on GPU. *Powder Diffraction*, 28(S2):S339–S350, 2013.

[32] Jérôme Kieffer and Dimitrios Karkoulis. PyFAI, a versatile library for azimuthal regrouping. In *Journal of Physics: Conference Series*, volume 425, page 202012. IOP Publishing, 2013.

[33] Uwe Kreibig and Peter Zacharias. Surface plasma resonances in small spherical silver and gold particles. *Zeitschrift für Physik*, 231(2):128–143, 1970.

[34] Joseph R Lakowicz. Radiative decay engineering: biophysical and biomedical applications. *Analytical biochemistry*, 298(1):1–24, 2001.

[35] S Lalitha, R Sathyamoorthy, S Senthilarasu, A Subbarayan, and K Natarajan. Characterization of CdTe thin filmdependence of structural and optical properties on temperature and thickness. *Solar Energy Materials and Solar Cells*, 82(1):187–199, 2004.

[36] Stephan Link and Mostafa A El-Sayed. Spectral properties and relaxation dynamics of surface plasmon electronic oscillations in gold and silver nanodots and nanorods. *The Journal of Physical Chemistry B*, 103(40):8410–8426, 1999.

[37] Stephan Link and Mostafa A El-Sayed. Optical properties and ultrafast dynamics of metallic nanocrystals. *Annual Review of Physical Chemistry*, 54(1):331–366, 2003.

[38] Nuria Lopez, TVW Janssens, BS Clausen, Y Xu, Manos Mavrikakis, T Bligaard, and Jens Kehlet Nørskov. On the origin of the catalytic activity of gold nanoparticles for low-temperature CO oxidation. *Journal of Catalysis*, 223(1):232–235, 2004.

[39] Stefan A Maier, Pieter G Kik, Harry A Atwater, Sheffer Meltzer, Elad Harel, Bruce E Koel, and Ari AG Requicha. Local detection of electromagnetic energy transport below the diffraction limit in metal nanoparticle plasmon waveguides. *Nature Materials*, 2(4): 229–232, 2003.

[40] P Michalowski, M Schmidt, F Schmidl, V Grosse, D Kuhwald, C Katzer, U Hübner, and P Seidel. Engineering of $YBa_2Cu_3O_7$-δ grain boundary josephson junctions by Au nanocrystals. *Physica status solidi (RRL) - Rapid Research Letters*, 5(8):268–270, 2011.

[41] V Nagarajan, IG Jenkins, SP Alpay, H Li, S Aggarwal, L Salamanca-Riba, AL Roytburd, and R Ramesh. Thickness dependence of structural and electrical properties in epitaxial lead zirconate titanate films. *Journal of Applied Physics*, 86(1):595–602, 1999.

[42] Lukas Novotny and Bert Hecht. *Principles of nano-optics*. Cambridge university press, 2012.

[43] Graz University of Technology. Atomic form factors. http://lamp.tu-graz.ac.at/~hadley/ss1/crystaldiffraction/atomicformfactors/formfactors.php.

[44] Matthew Pelton, Javier Aizpurua, and Garnett Bryant. Metal-nanoparticle plasmonics. *Laser & Photonics Reviews*, 2(3):136–159, 2008.

[45] Paras N Prasad. *Nanophotonics*. John Wiley & Sons, 2004.

[46] Fabien Silly and Martin R Castell. Bimodal growth of Au on $SrTiO_3(001)$. *Physical Review Letters*, 96(8):086104, 2006.

[47] Beamline staff. ID06 wiki page. http://wikiserv.esrf.fr/id06/index.php/Main_Page, 2013.

[48] CXRO: the center for x-ray optics. Atomic X-ray scattering factors. http://henke.lbl.gov/optical_constants/.

[49] Wikipedia the free encyclopedia. X-ray. http://en.wikipedia.org/wiki/X-ray, 2014.

[50] Wikipedia the free encyclopedia. Plasmon. http://en.wikipedia.org/wiki/Plasmon, 2014.

[51] DH Tomboulian and PL Hartman. Spectral and angular distribution of ultraviolet radiation from the 300-MeV Cornell synchrotron. *Physical Review*, 102(6):1423, 1956.

[52] M Valden, X Lai, and Dz W Goodman. Onset of catalytic activity of gold clusters on titania with the appearance of nonmetallic properties. *Science*, 281(5383):1647–1650, 1998.

[53] M Vollmer and U Kreibig. Optical properties of metal clusters. *Springer Ser. Mat. Sci*, 25, 1995.

[54] T Wagner, AD Polli, G Richter, and H Stanzick. Epitaxial growth of metals on (100) $SrTiO_3$: The influence of lattice mismatch and reactivity. *Zeitschrift für Metallkunde*, 92(7):701–706, 2001.

[55] Zhangmin Wang and Paul Wynblatt. The equilibrium form of pure gold crystals. *Surface Science*, 398(1):259–266, 1998.

[56] Bertram Eugene Warren. *X-ray Diffraction*. Courier Dover Publications, 1969.

[57] Philip Willmott. *An introduction to synchrotron radiation: Techniques and applications*. John Wiley & Sons, 2011.

[58] E Wolf. Electromagnetic diffraction in optical systems. i. an integral representation of the image field. *Proceedings of the Royal Society of London. Series A. Mathematical and Physical Sciences*, 253(1274):349–357, 1959.

[59] H You. Angle calculations for a '4s+ 2d' six-circle diffractometer. *Journal of Applied Crystallography*, 32(4):614–623, 1999.